

UNCLASSIFIED

AD 426787

DEFENSE DOCUMENTATION CENTER

FOR

SCIENTIFIC AND TECHNICAL INFORMATION

CAMERON STATION, ALEXANDRIA, VIRGINIA



UNCLASSIFIED

NOTICE: When government or other drawings, specifications or other data are used for any purpose other than in connection with a definitely related government procurement operation, the U. S. Government thereby incurs no responsibility, nor any obligation whatsoever; and the fact that the Government may have formulated, furnished, or in any way supplied the said drawings, specifications, or other data is not to be regarded by implication or otherwise as in any manner licensing the holder or any other person or corporation, or conveying any rights or permission to manufacture, use or sell any patented invention that may in any way be related thereto.

626787

64-6

U. S. A R M Y

TRANSPORTATION RESEARCH COMMAND
FORT EUSTIS, VIRGINIA

TRECOM TECHNICAL REPORT 63-45

A STUDY OF THE RADIATIVE CHARACTERISTICS
OF SHIELDED INFRARED SOURCES

Task 1D121401A14802
(Formerly Task 9R38-01-022-02)
Contract DA 44-177-TC-805

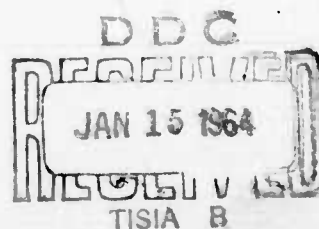
October 1963

CATALOGED BY DDC

AS AD No.

prepared by:

HAYES INTERNATIONAL CORPORATION
Birmingham, Alabama



DISCLAIMER NOTICE

When Government drawings, specifications, or other data are used for any purpose other than in connection with a definitely related Government procurement operation, the United States Government thereby incurs no responsibility nor any obligation whatsoever; and the fact that the Government may have formulated, furnished, or in any way supplied the said drawings, specifications, or other data is not to be regarded by implication or otherwise as in any manner licensing the holder or any other person or corporation, or conveying any rights or permission, to manufacture, use, or sell any patented invention that may in any way be related thereto.

* * *

DDC AVAILABILITY NOTICE

Qualified requesters may obtain copies of this report from

Defense Documentation Center
Cameron Station
Alexandria, Virginia 22314

* * *

This report has been released to the Office of Technical Services, U. S. Department of Commerce, Washington 25, D. C., for sale to the general public.

* * *

The findings and recommendations contained in this report are those of the contractor and do not necessarily reflect the views of the U. S. Army Mobility Command, the U. S. Army Materiel Command, or the Department of the Army.

HEADQUARTERS
U S ARMY TRANSPORTATION RESEARCH COMMAND
FORT EUSTIS, VIRGINIA


This report has been prepared by the Hayes International Corporation under the terms of Contract DA 44-177-TC-805. Views expressed in this report have not been reviewed or approved by the Department of the Army.

The technical objectives of this contract called for derivation of a theoretical or an empirical analysis which may be used to predict the infrared radiant intensity as a function of azimuthal angle for representative complex radiation sources.

The results of the investigation clearly indicate the feasibility of predicting the radiative characteristics of shielded infrared sources whose geometries can be described by analytical equations; the conclusions resulting from this feasibility study are concurred in by this command.

The information in this report will be utilized in future aircraft design to reduce radiation and thus to improve the passive defense characteristics of aircraft.


E. V. MERRITT
Project Engineer


WOODBURY JOHNSON, Lt Col, TC
Group Leader
Human Factors & Survivability Group

APPROVED.

FOR THE COMMANDER:


LARRY M. HEWIN
Technical Director

Task 1D121401 A14802
(Formerly Task 9R38-01-022-02)
Contract DA 44-177-TC-805
TRECOM Technical Report 63-45
October 1963

A STUDY OF THE RADIATIVE
CHARACTERISTICS OF SHIELDED
INFRARED SOURCES

Interim Report

Engineering Report Number 649

Prepared by
Hayes International Corporation
Birmingham, Alabama

for
U. S. ARMY TRANSPORTATION RESEARCH COMMAND
FORT EUSTIS, VIRGINIA

FOREWORD

This investigation was made under Army Contract Number DA 44-177-TC-805 by Hayes International Corporation, Birmingham, Alabama, during 1962 and 1963. This paper effectively extends the investigations made by the Johns Hopkins Radiation Laboratory on cylindrical radiation shields to conical and cylindrical shields with and without spherical innerbodies.

The infrared research staff of Hayes International Corporation wishes to express appreciation to Mr. B. F. Hochheimer of Johns Hopkins for helpful suggestions in regard to instrumentation.

CONTENTS

	Page
FOREWORD	ii
ILLUSTRATIONS	v
SYMBOLS	viii
SUMMARY	1
CONCLUSIONS.	2
INTRODUCTION.	3
HISTORY OF EXPERIMENTAL PROGRAM	4
EXPERIMENTAL APPARATUS.	4
Design Criteria	4
Basic Model Configurations	5
Constant-Temperature Bath Complex	9
EXPERIMENTAL INSTRUMENTATION AND MEASUREMENTS	14
Original Experimental Equipment Arrangement	14
Final Experimental Equipment Arrangement	15
METHODS OF EXPERIMENTAL PROGRAM	20
EXPERIMENTAL MEASUREMENTS	20
CONFIGURATION MODELS STUDIED	27

CONTENTS (CONT'D.)

	Page
DATA REDUCTION	27
Theory of Filter Radiometer	32
Radiometer Field of View	39
Computer Program for Data Reduction	42
PRESENTATION OF RESULTS	46
ANALYSIS OF EXPERIMENTAL ERROR.	76
ANALYSIS OF COMPUTER PROGRAMS	83
INTRODUCTION	83
MONTE CARLO TECHNIQUES	84
RAY-TRACING TECHNIQUES	86
RESULTS	93
COMPARISON OF EXPERIMENTAL MEASUREMENTS AND EMPIRICAL PREDICTIONS.	98
DISTRIBUTION	100

ILLUSTRATIONS

Figure		Page
1	Cylinder	6
2	Reversible Frustum of a Cone	7
3	Two Opposed Truncated Cones Having a Common Diameter	8
4	Experimental Apparatus Assembly as Originally Fabricated	10
5	Eroded Inconel Plate	12
6	Temperature Distribution Over Source Plate	13
7	Block Diagram of Original Experimental Arrangement	16
8	Block Diagram of Final Experimental Arrangement	19
9	Temperature-Compensated Contact Thermocouple	20
10	Field of View for Barnes R4F-1 Radiometer	23
11	Normalized Comparison Between Lambert Cosine Curve and Observed Radiation from Unshielded Source Plate	26
12	Cylinder	28
13	Reversible Frustum of a Cone	29

ILLUSTRATIONS (CONT'D.)

Figure		Page
14	Two Opposed, Truncated Cones Having a Common Diameter	30
15	Solid Angle Ω in Direction θ from Normal	36
16	Spectral Transmission Curve for the First ($n = 1$) Band-Pass Filter	44
17	Unsmoothed Spectral Radiant Intensity for Two Shield Configurations	47
18	Normal Radiation from Gold Cones	49
19	Gold Cylinder, No Innerbody.	55
20	Black Cylinder, No Innerbody	56
21	Gold Cylinder and Gold Innerbody, Front Position	57
22	Gold Cylinder and Gold Innerbody, Back Position	58
23	Gold Cylinder and Black Innerbody, Front Position	59
24	Gold Cylinder and Black Innerbody, Back Position	60
25	Black Cylinder and Gold Innerbody, Front Position	61
26	Black Cylinder and Black Innerbody, Front Position	62

ILLUSTRATIONS (CONT'D.)

Figure		Page
27	Gold Large Cone, No Innerbody	63
28	Gold Large Cone, Gold Innerbody	64
29	Gold Large Cone, Black Innerbody	65
30	Black Large Cone, No Innerbody	66
31	Gold Small Cone, No Innerbody	67
32	Gold Small Cone, Gold Innerbody	68
33	Gold Small Cone, Black Innerbody	69
34	Black Small Cone, No Innerbody.	70
35	Gold Double Cone, No Innerbody	71
36	Sum of Large Plus Small Gold Cones	72
37	Gold Double Cone, Gold Innerbody.	73
38	Gold Double Cone, Black Innerbody	74
39	Black Double Cone, No Innerbody	75
40	Cylinder with Emergent Ray L_1 and Reflected Ray L_2	87
41	Geometry for Determining Reflected Ray	89

SYMBOLS

λ	wavelength
$\Delta\lambda$	wavelength interval
J	radiant intensity
$J(\lambda)$	spectral radiant intensity
N	radiance
$N(\lambda)$	spectral radiance
$W(\lambda)$	spectral emittance
A_B	area of black body aperture
A_T	area of target source
$\tau_a(\lambda)$	water vapor spectral transmittance
$\tau_f(\lambda)$	spectral transmittance of band pass filter
$\Delta\lambda^*$	filter band width
V_B	radiometer voltage caused by black body
V_T	radiometer voltage caused by target source
f_J	filter factor
F	field-of-view correction factor
θ	aspect angle
$\beta(\lambda)$	generalized absorption coefficient
T	temperature

SYMBOLS (CONT'D.)

L denotes a ray
k, l, m direction cosines
R reflectivity
 Ω solid angle

SUBSCRIPTS

n denotes integral values
T denotes quantities pertaining to target radiation source
B denotes quantities pertaining to black body source
m denotes a maximum value

SUMMARY

This project has been conceived as having a dual purpose: (1) the laboratory measurement of certain model configurations having simple, carefully maintained boundary conditions, with the aim of determining the radiant intensity distribution as a function of the azimuthal angle and expressing the radiant intensity in a suitable system of units, as opposed to normalized curves; and (2) the derivation of a theoretical or empirical formulation for the prediction of the radiant intensity as a function of the azimuthal angle for complex, shielded, radiating sources.

The first part of the program was carried out by the manufacturing of three basic configuration shields or models and the necessary associated apparatus to provide a uniformly heated source plate, and by the measuring of the radiant intensity as a function of the azimuthal angle by means of a total radiometer modified for spectral measurements and referenced to a black body.

The second portion of the project focused on the writing of eight computer programs aimed at predicting the radiant intensity patterns. The results of this effort were encouraging, with predictions for some configurations yielding excellent agreement with laboratory measurements. Other predictions indicated that certain modifications to the computer programs, in the form of supplementary programs, might produce a closer agreement. Time did not permit an extensive investigation of this hypothesis. However, the results obtained from the present formulation clearly indicate the feasibility of the accurate prediction of the radiative characteristics of shielded infrared sources by electronic computers.

CONCLUSIONS

The results obtained from the computer programs clearly indicate the feasibility of the accurate prediction of the radiative characteristics of shielded infrared sources whose geometries can be described by analytical equations. This technique, it is felt, can even be applied to complicated shield configurations and to hot reflecting surfaces, although verification of the latter application may require laboratory substantiation. The degree of accuracy is limited primarily by the degree of approximation used in the mathematical representations of the geometries. Although specular reflection was assumed in the programs of this project, this is not a prerequisite; hence, diffuse surfaces may also be considered. The programs originally written for this project, however, need certain modifications in the form of supplementary programs, described in the section Comparison of Experimental Measurements and Empirical Predictions.

Investigations into theories of atmospheric absorption made in connection with the data reduction program pointed out the need for more comprehensive data over short path lengths (tens of meters) and on a finer wavelength scale (hundredths of a micron).

INTRODUCTION

During the past several years, Hayes International Corporation has conducted research and development programs which consisted of studies leading to prediction of infrared radiation from aircraft and other vehicles. The experimental measurements led to results which differed from the theoretical predictions to the extent that an alternate method of prediction was sought. The methods by which predictions were made when this project was initiated were based on projected areas, the temperatures of these areas, and the physical constants of the materials to arrive at a radiant energy distribution calculation. There was an approximate method* by which multiple reflections from the interior of radiant sources could be taken into account; but the applicable geometries were limited, and the radiant intensities calculated were for the total radiation emitted into a hemisphere rather than for an angular distribution. Snider, Sobel, and Anselone** investigated the radiation pattern of a heated flat plate and an attached, cooled, cylindrical shield; but their analysis was limited to the case of the cylinder, and all results were normalized. The over-all problem of getting comparable results for prediction and measurement of a variety of complex configurations led to the present program upon which this report is based.

* Hayes Aircraft Corp. Eng. Report No. 475, "Project Red Skin - Final Report", Contract AF 33(616)-6566, Nov. 1, 1959.

** A. E. Snider, F. Sobel, and P. Anselone, "Some Effects of Cylindrical Radiation Shields-Part One-Experimental", and "Part Two-Mathematical Treatment", Johns Hopkins Radiation Lab Reports AF-29, March 1956.

HISTORY OF EXPERIMENTAL PROGRAM

EXPERIMENTAL APPARATUS

Design Criteria

In the initial planning of the project, it was obvious that the calculations to be made in arriving at the final radiant intensity patterns for the various cavities would depend heavily upon the boundary conditions imposed. Although the theoretical analysis was written in such a manner as to be applicable to most general cases, it was desirable to make the boundary conditions as simple as possible, initially.

In accomplishing this, the models were designed so that they would consist, basically, of a cavity consisting of a flat, circular metal plate as the base and interchangeable walls of various shapes which would act as shields for the base. The following general boundary conditions were followed as closely as possible in the designing of the models:

- (1) The base plate was blackened and assumed to be a black body emitter. It was heated in such a way as to minimize thermal gradients across the surface and time variations of the temperature about the control point.
- (2) Cylindrical symmetry about an axis perpendicular to the center of the base plate was preserved in all models, including those having innerbodies within the cavity.
- (3) The shields and innerbodies were water-cooled so that their contribution to the total radiant intensity was negligible compared with that of the base plate.
- (4) The reflection coefficients of the inner walls of the shields, as well as the outer surfaces of the innerbodies, were made constant and were not considered as a function of the angle of incidence.

(5) Specular reflection from all surfaces was assumed.

Basic Model Configurations

The design of the experimental apparatus consistent with the above assumptions began as scheduled, followed by fabrication in the shops. The first model to be completed was the water-cooled cylinder. The inner surface of the model was a 4-inch-diameter copper tube, 8 inches long. It was designed to accept two hollow, spherical innerbodies made from stainless steel and having diameters of $2\frac{1}{2}$ and 3 inches. Like the model, the innerbodies were water-cooled. (See Figure 1.)

The second model to be completed was a reversible frustum of a cone having provisions for removable, water-cooled spherical innerbodies of 2- and $3\frac{1}{2}$ -inch diameters in the small and large ends, respectively. The design of the cone provided for apertures of $2\frac{3}{4}$ inches and 5 inches in diameter and a length of 8 inches. The water-cooled model was designed to be reversible so that either end could be placed adjacent to the plate source. The model was made from rolled, $\frac{1}{8}$ -inch brass sheets and was polished to a mirror finish. (See Figure 2.)

The third, and last, model consisted of two opposed truncated cones having a common diameter of $4\frac{1}{8}$ inches and end diameters of $3\frac{1}{8}$ and $3\frac{5}{8}$ inches, with a total length of $5\frac{1}{2}$ inches. This water-cooled model provided for the insertion of a $3\frac{1}{2}$ -inch water-cooled innerbody at the apex of the model. Like the conical model, it was made from $\frac{1}{8}$ -inch rolled brass sheets and was polished to a mirror finish. (See Figure 3.)

The assumption of specular reflection that was made in the theoretical analysis required that all inner cavity surfaces (and innerbody surfaces) have a mirror finish. This was achieved by polishing the surfaces with successively finer grades of emory paper and finally with jeweler's rouge.

For the first phase of the project, all model and innerbody surfaces were gold plated. The gold plating was done by Precision Plating and Metal Finishing Company of St. Petersburg, Florida.

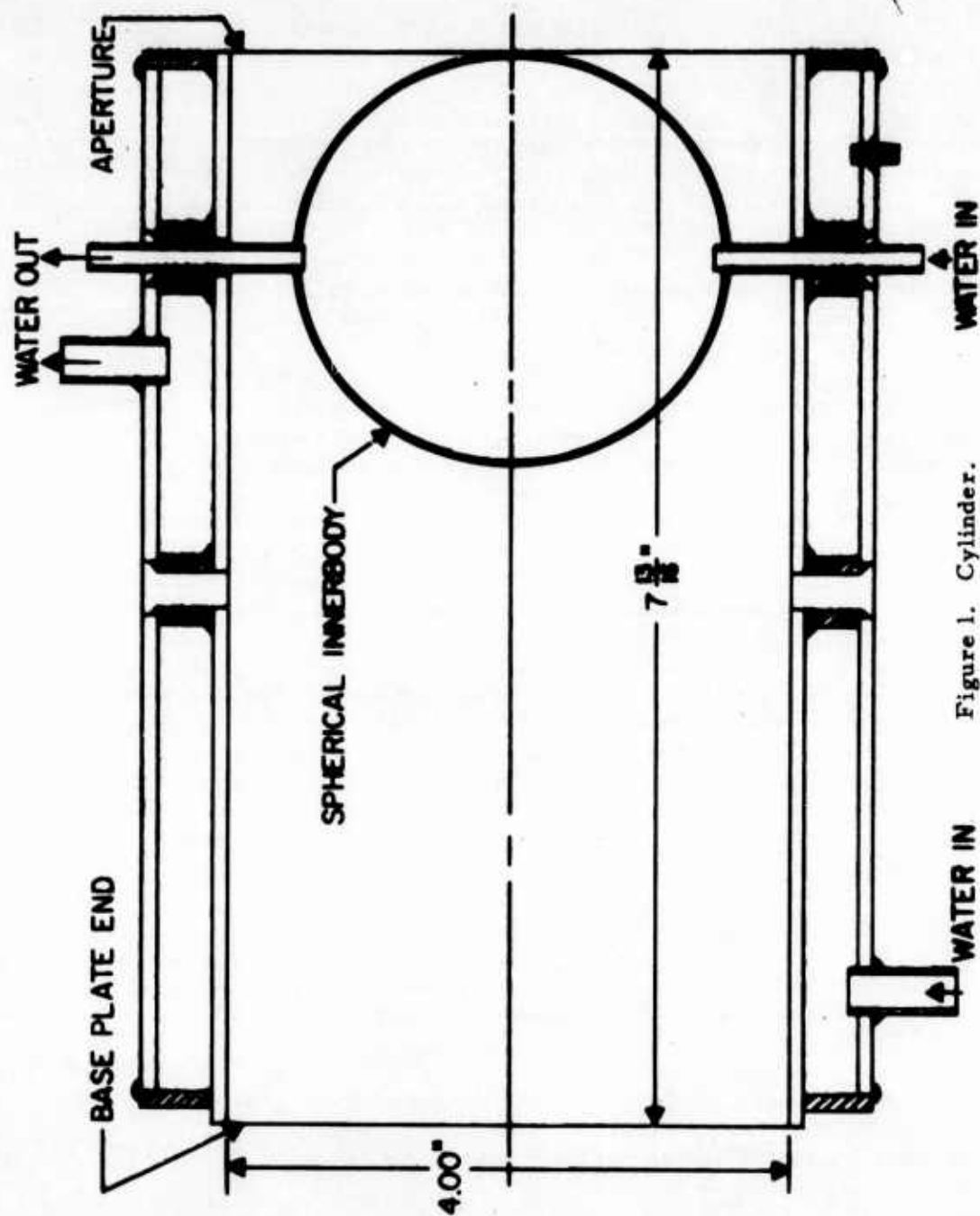


Figure 1. Cylinder.

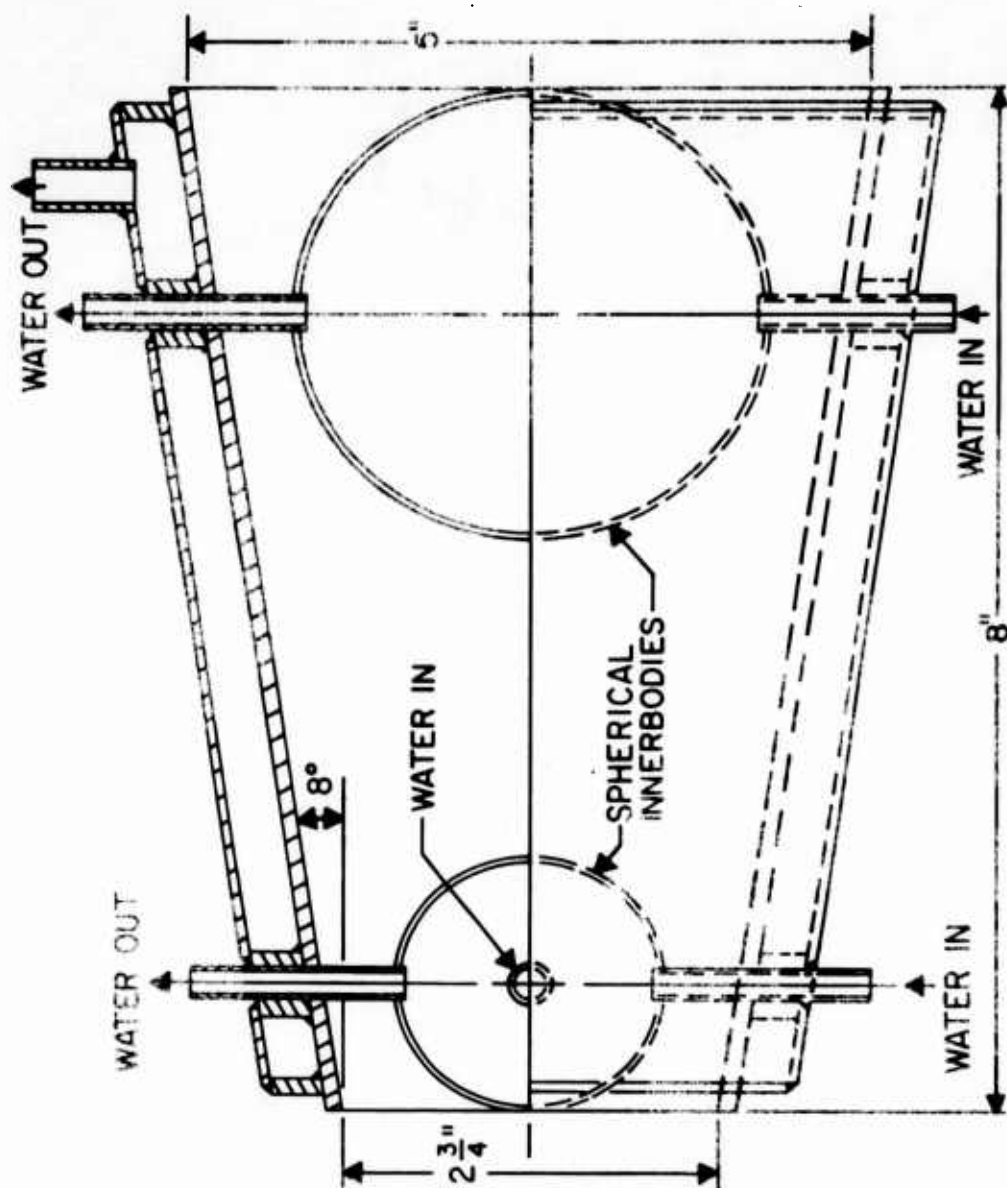


Figure 2. Reversible Frustum of a Cone.

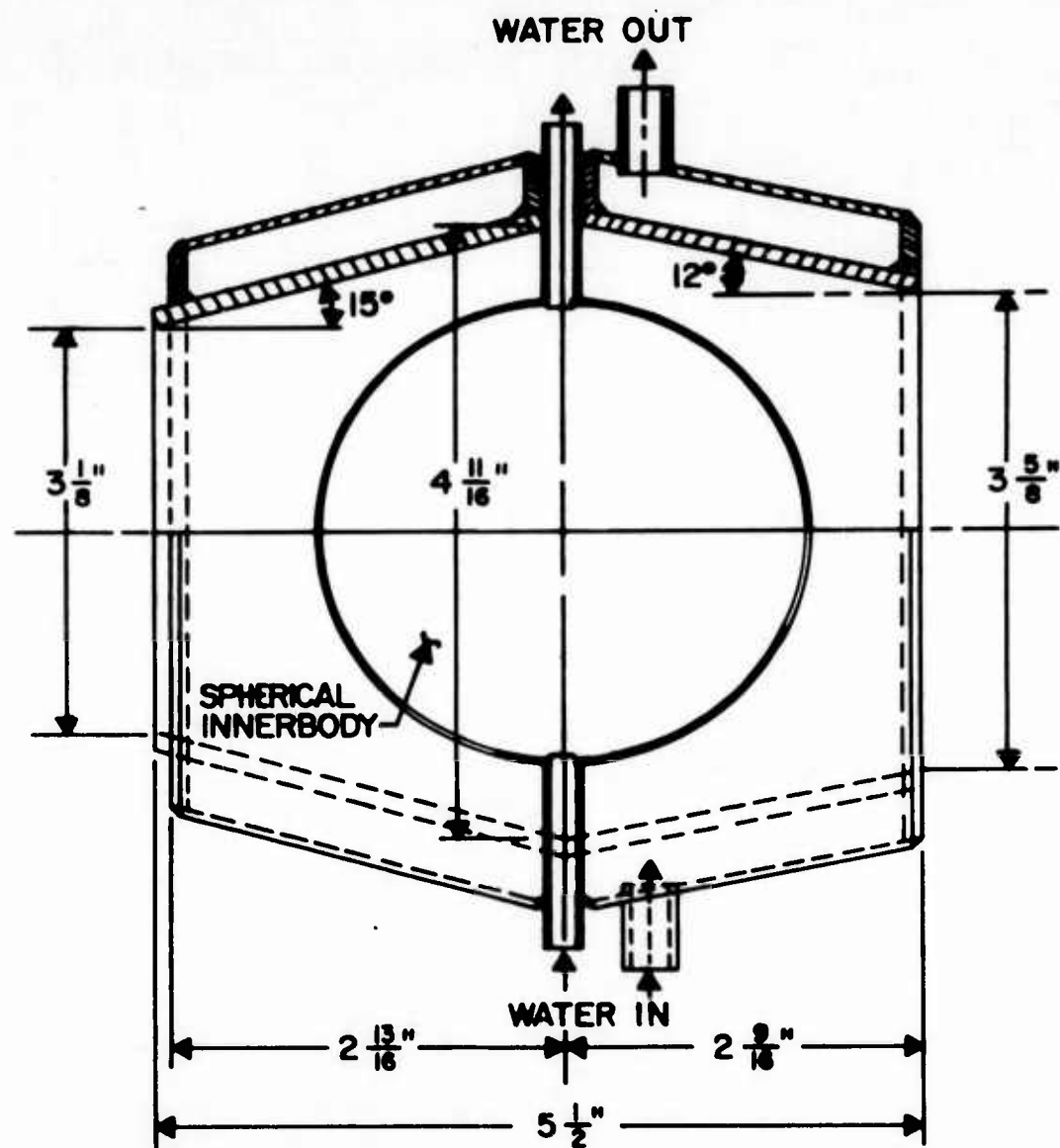


Figure 3. Two Opposed, Truncated Cones Having a Common Diameter.

The second phase of the project required the surfaces to be coated with a material of low reflectivity. The material finally chosen was "3M" #9564 Black Velvet Coating, a durable, low-reflectance substitute for lampblack, originally planned. Minnesota Mining and Manufacturing Company states that the reflectivity of this coating material is less than 0.01 from 0.2 to 20 microns.

Constant-Temperature Bath Complex

Several methods of heating a flat, vertically mounted plate in order to achieve isothermal characteristics were considered for this program. Of those considered, two had been previously used by this laboratory. They are as follows:

- (1) A thin cover plate, mounted on a ceramic form containing closely spaced nichrome wire resistance heating elements. The cover plate showed temperature variations as much as 10° to 15°C over a 1-inch-diameter circle in its center.
- (2) A thin cover plate mounted in the opening of a small, electrical furnace with an additional nichrome wire heating element positioned at the base of the plate. Surface temperatures varied up to 5°C over a 1-inch-diameter circle in the center of the plate.

Since it was desirable to have as little temperature variation as possible, and since both methods were difficult to adjust, they were ruled out as possible methods for this program. Other methods considered were similarly ruled out, and attention was given to an altogether new method.

This method exhibited smaller thermal gradients than the above systems, and had a much greater temperature stability as well as a less critical adjustment. Hence, the boundary conditions considered in the theoretical analysis were closely approached in the experimental apparatus.

Figure 4 shows the assembly of the apparatus as it was originally fabricated. A section was cut from the wall of a stainless steel pipe (304ELC, 8.303 inches I.D., .322 inch wall) and replaced by

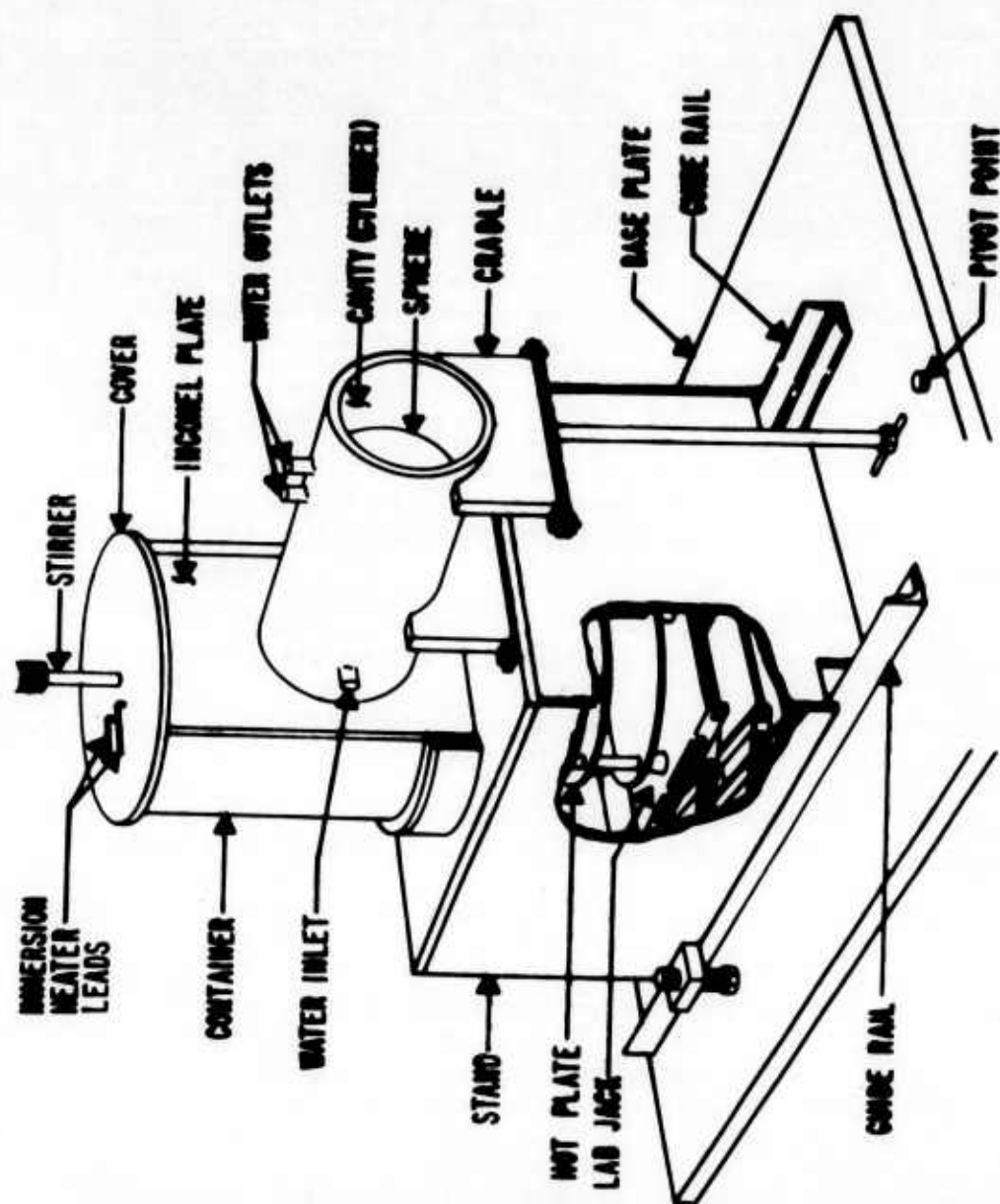


Figure 4. Experimental Apparatus Assembly as Originally Fabricated.

a flat Inconel plate ($9\frac{1}{2}$ inches x 6 inches x $\frac{1}{8}$ inch) and welded in place. Then, a 304ELC stainless steel plate was welded to one end of the pipe, completing the formation of a container $9\frac{1}{2}$ inches tall and open at the top. The container was to be filled with an alloy such as 50% tin - 50% zinc (weight per cent). The exact alloy was to be adjusted in order to obtain the desired temperatures. The container was placed on a steel stand 10 inches tall, and the alloy was melted by a 1200-watt, 7-inch-diameter hot plate raised into position under the container through a circular opening in the stand. After melting, the hot plate was to be removed and the temperature of the liquid alloy raised to the control point by two 1000-watt Calrod immersion heating elements. A homogeneous bath temperature was insured by stirring the hot liquid with a propeller attached by a stainless steel shaft through the open top to a stirring motor. An immersion heater was used to minimize temperature gradients across the container walls (and the Inconel plate) which, it was believed, would occur if an external heater, such as the hot plate, were used. Fairly thick material was used in construction of the container to give it high heat capacity, thereby greatly reducing time varying fluctuations of the plate temperature.

The container was insulated on the circular portion of the wall with asbestos cloth, and an insulating sheet of Johns-Manville Superex was to be positioned under the bottom upon removal of the hot plate. This was to reduce heat losses from all parts of the container except the exposed Inconel plate and would, therefore, require less power for the immersion heaters to maintain the bath temperature at the control point.

An Inconel plate was used because of its resistance to scaling at high temperatures as opposed to metals such as copper, which rapidly build up a layer of surface scale at high temperatures.

The inside diameter of all cavities at the base was originally expected to be a maximum of 4 inches. The rectangular Inconel plate was made wider so that the large temperature gradients at the plate edges would not be present in the area forming the cavity base. Also, the entire area of the Inconel plate was flame-coated with chromium oxide and exposed to the ambient atmosphere so that radiation losses would tend to be equalized over the whole plate surface. If only the area forming the cavity base were oxidized,

and the remaining plate surface not made to radiate energy at the same rate, temperature gradients would be present at the edges of the cavity base despite all other precautions.

For the same reasons, the back edges of the water-cooled models were not brought into contact with the plate, but were separated by a small air gap. Even so, the presence of the models was probably the greatest contributing factor to any existing thermal gradients in the cavity base.

Pure zinc, which has a melting point of 419.5°C , was chosen as the liquid metal to be used in the container. Zinc's thermal properties (heat of fusion and specific heat) are such that the time required to raise its temperature to the anticipated operating point was considered to be relatively short. Other reasons for the choice of zinc were: (1) vapor from liquid zinc is only slightly toxic, (2) pure zinc is very inexpensive, and (3) it is readily available.

When the fabrication of the experimental apparatus was completed and the apparatus was assembled, the zinc metal was placed in the container and melted. After a short period of time, it was observed that the liquid zinc was becoming contaminated. An investigation led to the realization that the Inconel plate forming the front of the container was being dissolved by the liquid zinc. The plate was cut out and it was discovered that, after exposure to the liquid zinc for about 44 hours at a temperature of 450°C , the remaining portion of the plate was no more than $\frac{1}{32}$ inch thick in some places. A typical cross section of the Inconel plate is shown in Figure 5.

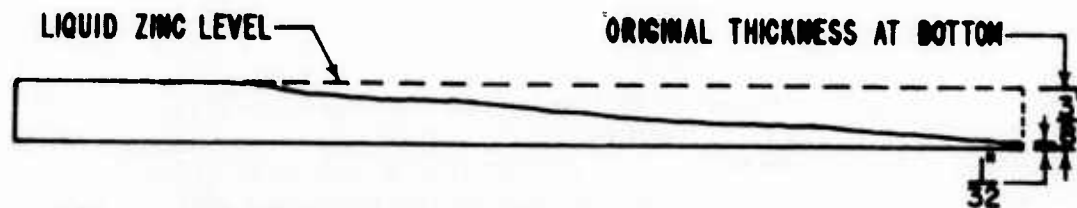


Figure 5. Eroded Inconel Plate.

This situation was corrected by replacing the Inconel plate with a $\frac{1}{4}$ -inch plate of 304ELC stainless steel. The zinc metal was replaced by a Class II heat treatment salt which has a melting point of 220°C. The bath was operated in the vicinity of 470°C for the remainder of the program with no indication of adverse effects.

Measurements of the temperature distribution over the source plate of the constant-temperature bath were made with the bath operating at about 433°C. The temperature distribution was later checked at higher temperatures and found to be essentially the same. A compensated contact thermocouple was used to make the measurements. A sample distribution is shown in Figure 6, where the rectangular outline represents the source plate. The dashed circle shows the

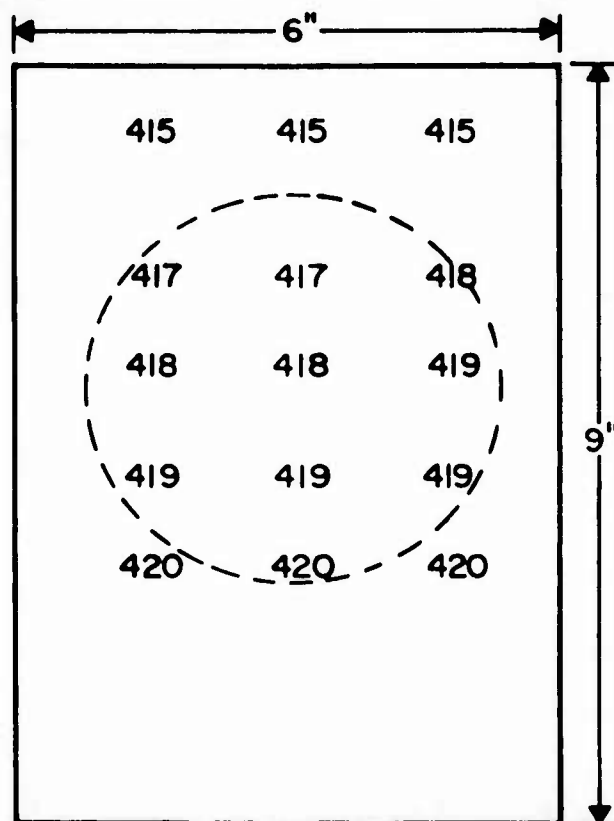


Figure 6. Temperature Distribution Over Source Plate

relative location of the area which served as the base plate of the various model configurations.

A need for certain improvements in the apparatus became evident as preliminary measurements were nearing completion. It was felt that these improvements would result in increased accuracy and reliability in subsequent measurements. So, advantage was taken of the delay caused by the radiometer modification (to be discussed in the next section) to execute these changes.

The biggest change was the design and fabrication of a new apparatus shield. The new shield provided a more uniform radiation background and a more positive means for positioning and supporting the models. Smaller changes included: (1) a more substantial mounting for the temperature control thermocouple, (2) more accurate alignment of the radiating surface plate with the optical axis of the radiometer, (3) substitution of an optical black paint ("3M" #9564) for lampblack on spheres and cavities to facilitate handling, (4) modifying the liquid salt container by welding a flange around the top to prevent the salt's sloshing over the rim, and (5) recoating the flat emitting surface with a fresh layer of chromium oxide after it had been cleaned with a wire brush and emory paper and then sandblasted with aluminum oxide grit.

A third 1000-watt Calrod immersion heater had to be added to the original two heaters, and the 1200-watt hot plate had to be used to maintain an operating bath temperature of 470°C (450°C surface temperature for the emitting plate). The effect of thermal gradients arising from the use of the hot plate was negligible, and the relative temperature distribution remained essentially the same.

EXPERIMENTAL INSTRUMENTATION AND MEASUREMENTS

Original Experimental Equipment Arrangement

The arrangement of the laboratory equipment was originally designed so that a Barnes Model R4F1 Radiometer could alternately view the aperture of the cavity (model configuration) and the "point-source" aperture of a Barnes Model 8B Reference Black Body at the same distance. The radiometer output was amplified by a Barnes synchronous rectifier amplifier (a part of the Model R4F1 radiometer system) and recorded by a Varian Model G11-A Recorder.

The Barnes radiometer has a field of view between half-power points covering a plane angle of $\frac{1}{4}^\circ$ (1.0×10^{-6} steradian). A contour plot of relative radiometer sensitivity versus linear deviation from the radiometer optical axis for a point-source black body was used to determine the optimum distance between the collection optics of the radiometer and a 4-inch cavity aperture. It was originally desired to keep the cavity aperture within the 0.95 contour of the contour plot. Requiring a 4-inch aperture to lie within the 0.95 contour permitted the omission of correction factors normally used to compensate for the varying response over the field of view with negligible loss of accuracy. The minimum distance necessary to insure this condition was 187 feet. Since the laboratory used for the measurements was only 90 feet in length, it was necessary to reflect the radiation twice between the cavity and the radiometer. To make possible the inclusion of a 5-inch aperture, the beam path selected was 250 feet in length. The reflection was effected by two 8-inch x 10-inch, front-surfaced, aluminized mirrors. In the spectral band considered, the reflectivity of aluminum is essentially constant; consequently, the reflections did not affect the spectral distribution of the radiant intensity from the cavity.

A Perkin-Elmer Model 13 Spectrophotometer was located close to the cavity aperture to collect the emitted radiation and to plot a continuous relative spectral distribution curve.

During normal operation, the constant-temperature bath was heated by immersion heating elements and a 1200-watt, 7-inch-diameter hot plate, as previously described. The heating elements were powered by a Lindberg reactor and controlled through a Barber-Colman Model 610A pilot amplifier by a Wheelco Model 407 temperature control unit. The Wheelco unit, in turn, employed a chromel-alumel thermocouple as a temperature sensing element. The thermocouple was located in the bath liquid for a more reliable output.

A block diagram of the original laboratory arrangement is shown in Figure 7.

Final Experimental Equipment Arrangement

During the equipment calibration period of the program, a field-of-view calibration was performed for the Model 13 Spectrophotometer.

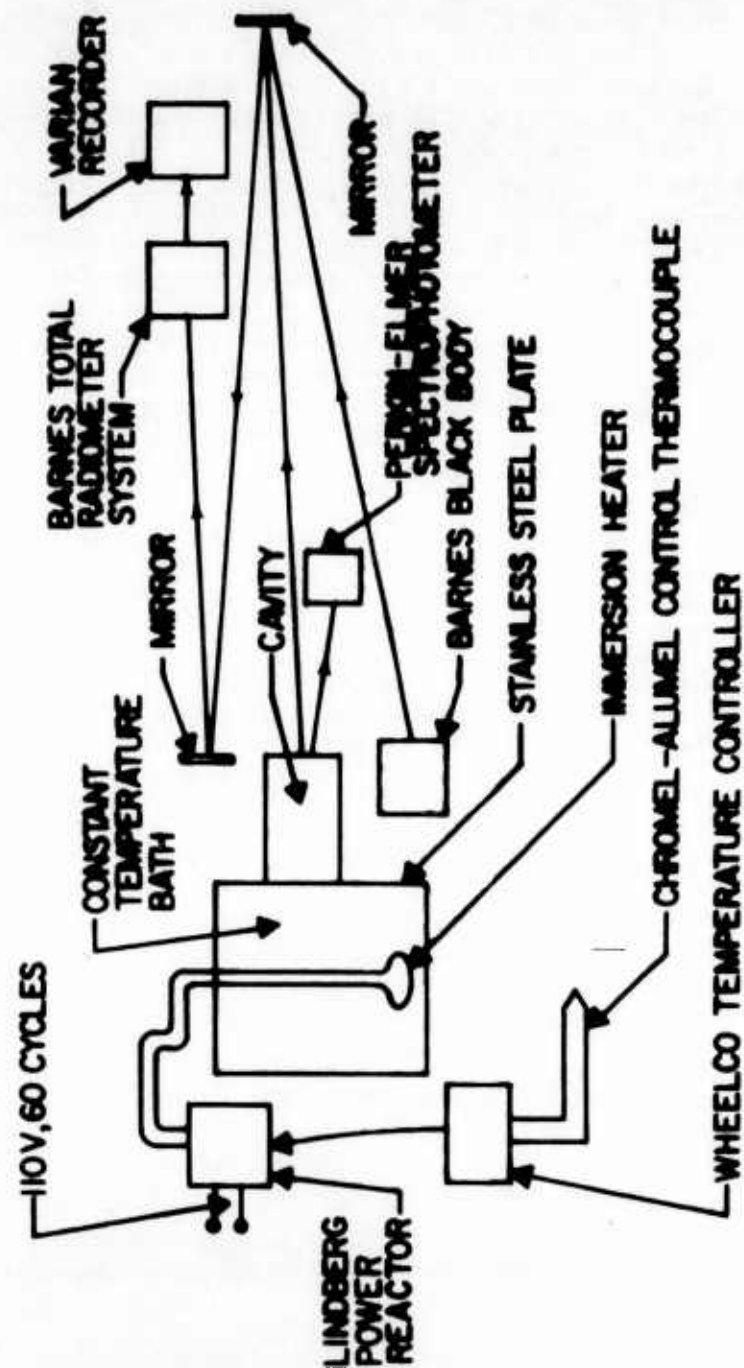


Figure 7. Block Diagram of Original Experimental Arrangement.

The results were somewhat disquieting, in that the field was considerably smaller than had been assumed. With the spectrophotometer located about 8 feet from the infrared source, the rectangular field of view measured about $\frac{1}{2}$ inch wide and about 3 inches high. At a distance of about 50 feet, the field had changed very little, measuring approximately $\frac{3}{4}$ inch by $3\frac{1}{2}$ inches. More precise dimensions of the field could not be obtained because the response does not drop to zero in a step; instead, it falls off quite rapidly over an interval of an inch or so on each side of the fairly flat, $\frac{1}{2}$ -inch band.

This narrow field of view of the spectrophotometer was undesirable because the spectrophotometer and the radiometer did not necessarily see the same area of the source. When the source is inhomogeneous in composition and temperature, it becomes difficult, if not impossible, to correlate data from the two instruments.

Studies were made to determine some way of correcting this situation. Possible solutions included (1) modification of the spectrophotometer collection optics and (2) modification of the radiometer.

Modification of the collection optics of the spectrophotometer would solve the problem of the limited field of view for the present program, but would present the same problem anew, if it were necessary for the spectrophotometer to view larger sources at some later time. The lengthy methods of data reduction would remain essentially unchanged. Modification of the radiometer, converting it to a semi-spectral radiometer, would eliminate the spectrophotometer from the measurements program. The resulting simplification would reduce considerably the process of data reduction. These two approaches were carefully evaluated, and a decision in favor of modifying the radiometer clearly became the only reasonable solution to the whole problem.

The heart of the modification is a set of eighteen optical interference filters. Each filter is a spike-type filter which passes radiation only over a narrow band of about 0.1 micron. The filters span the region from 1.68 to 5.16 microns at intervals of about 0.2 micron. A spectral distribution curve is drawn by viewing the source with successive filters and making a reference to a black body. Integrating under the spectral curve yields the radiant intensity.

The eighteen interference filters were mounted in two, parallel, closely spaced discs, each disc containing nine filters and one open hole. Rotation of the discs was accomplished by a pair of knobs mounted on the side of the radiometer. The internal mounting hardware was sprayed with "M" Black Velvet Coating to reduce extraneous reflections.

Because of the narrow band pass of the individual filters and the subsequent decrease in energy impinging on the detector, it was necessary to decrease the distance from the cavities to the radiometer. This distance, formerly 250 feet, was reduced to 147 feet. This was the maximum distance at which the calibrating reference black body could be seen. A new field-of-view contour plot of relative radiometer sensitivity versus linear deviation from the radiometer optical axis was made at 147 feet (see Figure 10). Superimposed on the field-of-view plot is a 5-inch circle, corresponding to the aperture of the largest model. As can be seen, most of the circle lies within the 80% response contour. Corrections were made to compensate for the decrease in detector response.

It will be recalled that two front-surfaced aluminized mirrors were used to increase the optical path length from the model configurations to the radiometer. With the reduced path length, it was possible to reduce, by one, the number of mirrors necessary to obtain the maximum distance of 147 feet.

In order to minimize the effects of atmospheric attenuation, the reference black body was placed at the same distance (147 feet) and had, essentially, the identical optical path as the models. The justification for this procedure will be discussed at length in the section on data reduction. To accomplish this without having to rotate the mirror, a separate mirror (identical to the first) was placed close by, and the black body was placed near the models. The radiometer was easily rotated from one position to the other.

A block diagram of the final laboratory arrangement is shown in Figure 8.

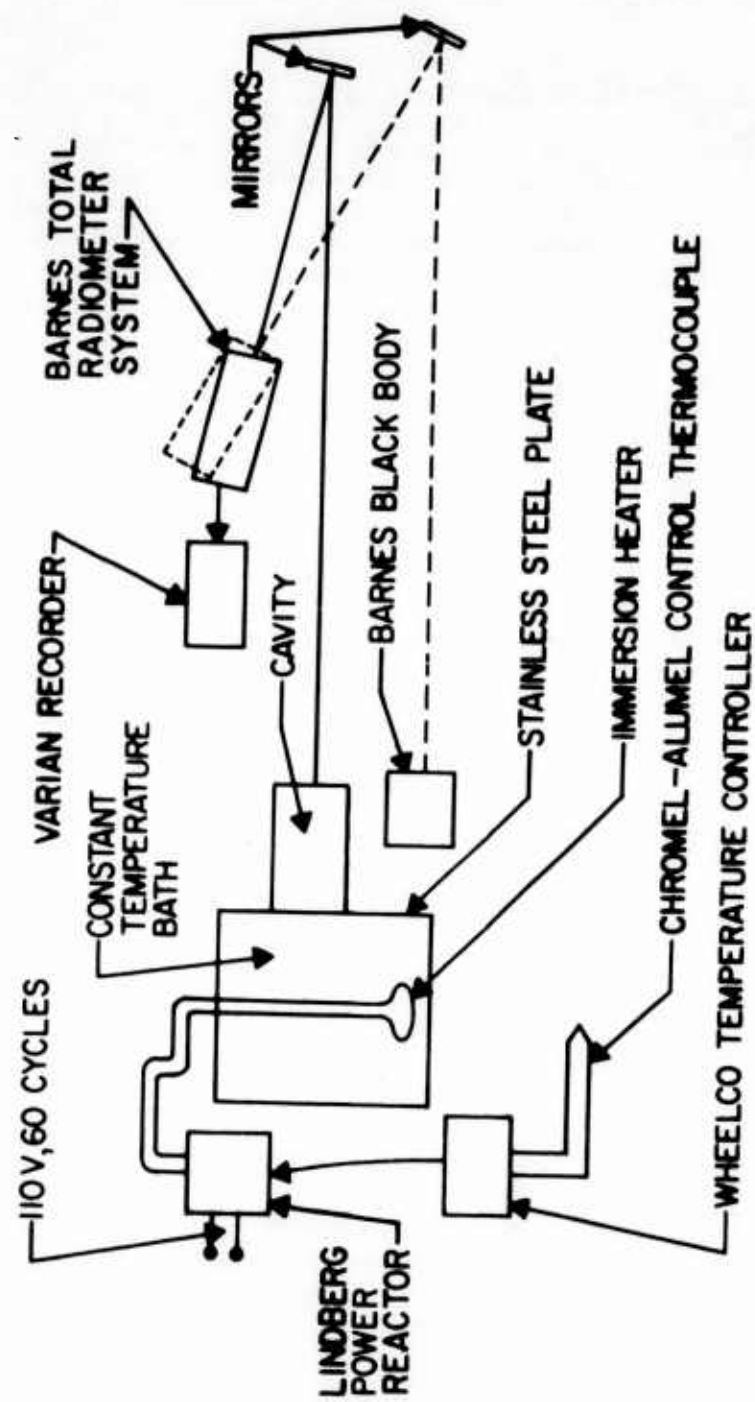


Figure 8. Block Diagram of Final Experimental Arrangement.

METHODS OF EXPERIMENTAL PROGRAM

EXPERIMENTAL MEASUREMENTS

A constant-temperature bath was used in the experimental portion of this program to provide a uniformly heated source plate at the base of the various model configurations. The temperature of the liquid salt bath was continuously monitored with a chromel-alumel thermocouple and displayed on the scale of the Wheelco Model 407 Indicating Controller. The controller was operated in association with a Barber-Colman Magnetic Plot Amplifier, Model 610A, which in turn drove a Lindberg Saturable Reactor. The controller complex maintained the bath at a constant, predetermined temperature - - in this case, 470°C. A 1200-watt, 3-speed hot plate was used to supplement the three 1000-watt Calrod immersion heaters.

The surface temperature of the source plate was measured with a modified temperature-compensated, contact-type, chromel-alumel thermocouple*. Figure 9 shows in schematic form how the thermocouple was constructed. The windings, electrically insulated from the thermocouple, served to heat the thermocouple junction to the

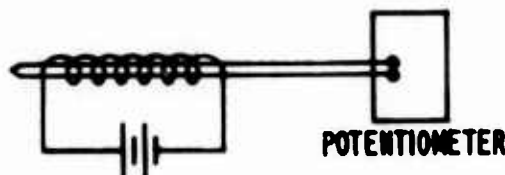


Figure 9. Temperature-Compensated,
Contact Thermocouple.

same temperature as the surface to be measured. When contact was established and no change in junction temperature was indicated, the

*Nobuji Sasaki and Akira Kamade, "A Recording Device for Surface Temperature Measurements", The Review of Scientific Instruments, Vol. 23, No. 6, June 1952, p. 261.

potentiometer (Leeds & Northrup Model K-3) reading was converted from millivolts to degrees Celsius to give the surface temperature. This device was used to determine the temperature distribution over the source plate, referred to in the preceding section.

As stated in a preceding section, the original program called for the radiometric measurements to be made with a Barnes Radiometer, Model R4F1 used in conjunction with a Perkin-Elmer Infrared Spectrophotometer, Model 13. The band pass of the radiometer was limited by filters to a region from 1.75 microns to 2.95 microns. Briefly, the radiometer voltage derived from the radiation output within this region was used to calibrate the response of the radiometer detector. The resulting power calibration was used to calibrate the ordinate axis of the relative spectral plot of the spectrophotometer over the region of 1.75 to 5.15 microns. Integration under the calibrated spectral curve yielded the radiant intensity of the source at a given aspect angle.

After the modification of the radiometer, the spectrophotometer was eliminated from the measurements program. The band pass of the radiometer was divided into eighteen narrow bands of 0.1 micron widths by means of interference filters. Viewing a source through the succession of filters was equivalent to using the spectrophotometer, but with the advantage of having the radiometer's field of view and detection system.

The initial step in making radiant intensity measurements was to view a reference black body at a known temperature through the succession of filters. The detector output voltages were amplified and recorded on a calibrated strip chart. After each filter reading, a background reading was taken by placing a black shield over the aperture. The source to be measured was then viewed by the radiometer at a given aspect angle in a manner identical to the viewing of the reference black body, including the background reading. The recorded net deflections for the source were then ratioed to the corresponding black body net deflections made in the same narrow filter band pass. This ratio of deflections, V_S/V_B , was multiplied by a factor f_J , which converted the voltage from the response to the source radiation to units of spectral radiant intensity, watts per micron per steradian. Plotting these spectral radiant intensity points yielded a curve of spectral

radiant intensity against wavelength. Integration under the curve from 1.68 to 5.16 microns yielded the total radiant intensity in this band for the particular model configuration when viewed at that aspect angle. The theory behind the derivation of the multiplicative factor f_j will be given in some detail in the section on data reduction.

Three sets of measurements made prior to the measurement of the model configurations deserve some comment. These are the field-of-view curves for the radiometer, the comparison of the source plate with a Lambert radiator, and the determination of the reflectivities of the surface finishes: gold plate on polished metal, and "3M" Black Velvet Coating on polished metal.

It was necessary to determine the extent to which the response of the detector was uniform across its face, since any extended source would be imaged on it by the optics in something more than a point. Because of attenuation by the radiometer filters, the optical path length had to be decreased from the original 250 feet to 147 feet. This was the maximum distance at which the reference black body could be seen by the radiometer. To determine the field of view, a "point source" black body was moved from point to point on an imaginary vertical grid having separations of one centimeter. At each point the recorder deflection was noted. The deflections were normalized to the maximum value and plotted on a sheet of square-grid graph paper. Points of equal response were connected to form contours of equal response. The resulting mapping of the field of view is shown in Figure 10. The heavy circle represents the largest of the model apertures. As can be seen, most of its area lies within the 80% contour. Details will be given in the section on data reduction about the correction factors applied to the data to compensate for the variations in detector sensitivity.

The computer programs which sought to simulate the laboratory measurements were written with the assumption that the source plate behaved like a Lambert radiator, i.e., the intensity of its radiation fell off according to the cosine of the angle of emission. Measurements were made to determine to what extent this assumption was valid. The source plate was rotated behind a fixed shield having a circular hole. As the source plate was rotated, the projection on the source plate of A_n , the area of the circular hole, increased inversely as the cosine of the angle of rotation, θ . If

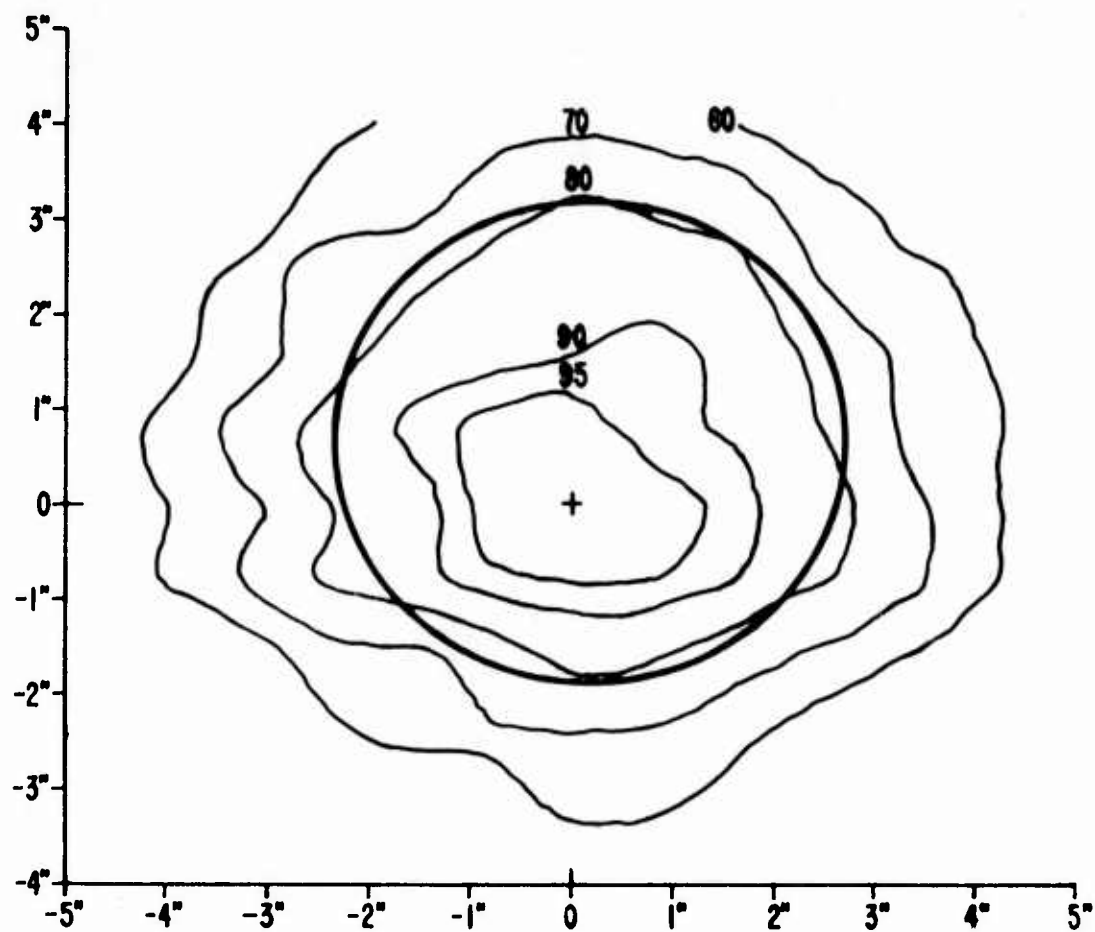


Figure 10. Field of View for Barnes R4F-1 Radiometer.

the source plate behaved like a perfect Lambert radiator, its radiance would decrease from its normal value, N_n , according to the cosine of the angle of rotation. The resulting signal should remain constant, independent of angle:

$$\frac{A_n}{\cos \theta} \cdot N_n \cos \theta = A_n N_n$$

The results are tabulated in Table 1 and are shown graphically in Figure 11, where the observed radiation from the source plate has been multiplied by $\cos \theta$ for comparison with the Lambert cosine curve. The deviation at 60° was less than 5%.

The computer programs were written to accept any value for the reflectivities of the surfaces of the models or their innerbodies. Measurements had to be made to determine as closely as possible the proper values of the reflectivities. Since special instrumentation for measuring reflectivities was not available, the initial examination was made on a Gardner glossmeter. Two small plates ($2\frac{1}{2}$ " x $4\frac{3}{4}$ "), one of copper and one of brass, were polished and sprayed with "3M" Black Velvet Coating. When the plates were subjected to glossmeter examination, no gloss was detectable. It was evident that a more refined technique would be required to determine the reflectivities. Since the sum of the emissivity and reflectivity of a given material is unity, the reflectivity may be determined by measuring the emissivity and subtracting it from unity. A 2-inch square was cut from the black-coated brass plate and a similar plate was gold plated in the same manner as the models. These plates were heated by a small radiation furnace. Surface temperatures were measured by a temperature compensated contact thermocouple, and black body temperatures were measured by inserting into the black body cavity the same thermocouple (without contact compensation). Although reflectivities at room temperature were desired, the techniques employed required the samples to be heated above the ambient temperature. Sample temperatures ranged from 125°C to 175°C for the black plate and from 150°C to 200°C for the gold plate. The radiometer was placed 4 to 8 feet from the samples and the black body. Observations were made of the black body and the samples over the full range of the spectral

TABLE 1
NORMALIZED COMPARISON BETWEEN LAMBERT COSINE
CURVE AND OBSERVED RADIATION FROM UNSHIELDED
SOURCE PLATE

Angle θ	Cos θ	Radiation Intensity x Cos θ Normalized to 10°	Deviation %
0	1.000	1.026	2.6
10	0.985	1.000	1.5
20	0.940	0.952	1.2
30	0.866	0.873	0.8
40	0.766	0.762	0.5
50	0.643	0.638	0.7
60	0.500	0.477	4.6

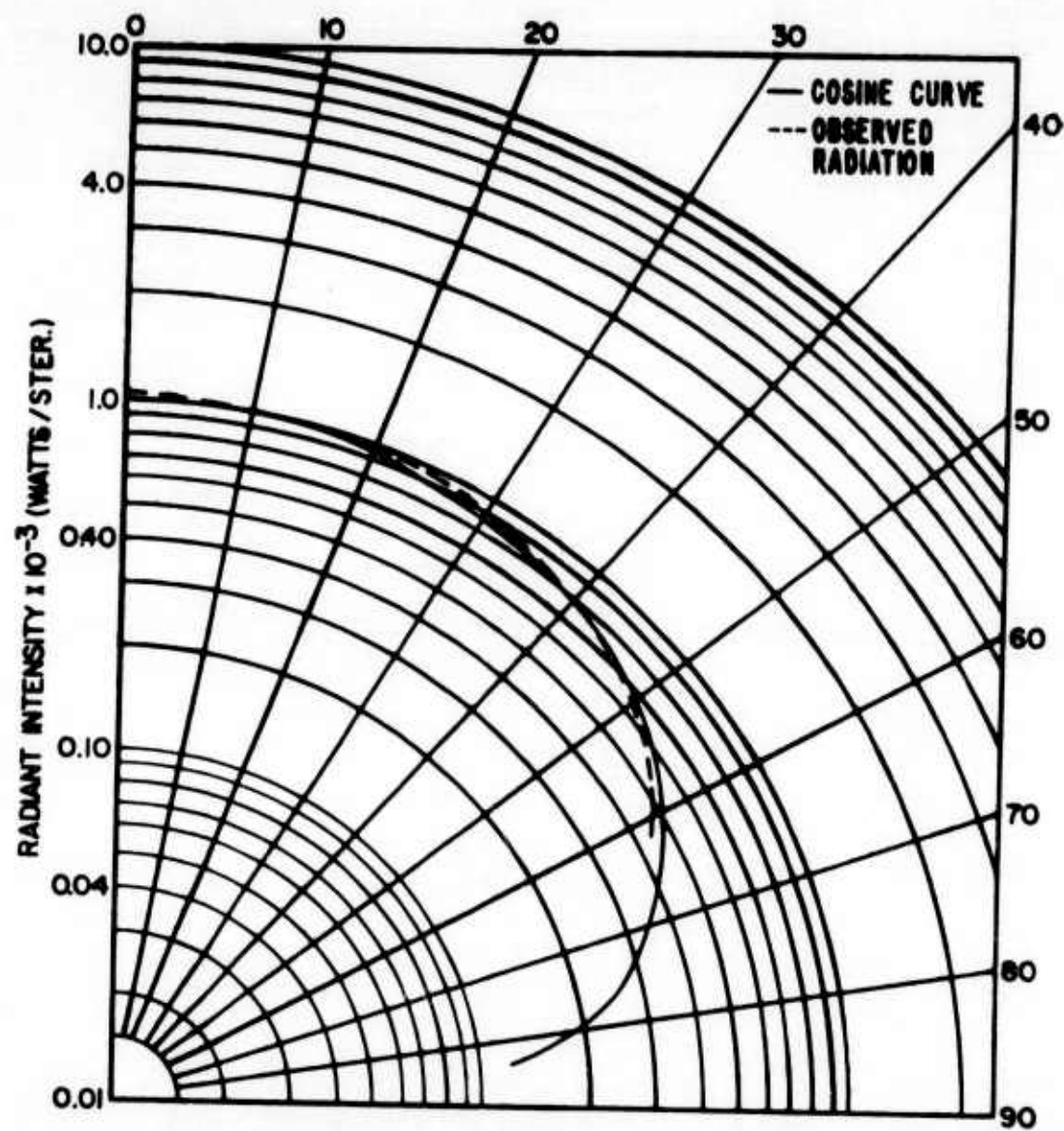


Figure 11. Normalized Comparison Between Lambert Cosine Curve and Observed Radiation from Unshielded Source Plate.

radiometer. The quotients of the net voltages from the samples and the corresponding net voltages from the black body were corrected for any difference between active sample and the black body areas. The results were the spectral emissivities of the samples. From the spectral emissivities, the total emissivities were calculated and plotted against temperature. The extrapolations to room temperature yielded an emissivity for the gold plate of 0.031 and an emissivity for the black plate of 0.995. The corresponding reflectivities were 0.969 (gold) and 0.005 (black).

CONFIGURATION MODELS STUDIED

A major part of the program was the laboratory measurements on various model configurations. A total of 20 different model configurations were measured. Photographs of the three basic models (the cylinder; the reversible frustum of a cone; and the two opposed, truncated cones or double cone) are shown in Figures 12, 13, and 14, respectively. Table 2 lists the different configurations studied. The cylinder, having the simplest geometry, was studied most fully. Certain configurations are conspicuous for their absence; e.g., the black double cone with either gold or black innerbody. The innerbody used with the double cone had a diameter greater than the source diameter, while the exit aperture diameter was only slightly larger than that of the innerbody. The result was that no ray could pass through the aperture without first suffering at least one reflection, and most rays would encounter several surfaces before escaping. With the double cone blackened, more than 99% of the energy was absorbed and conducted away by the coolant. So effective was the shielding that no heat could be felt with the hand at the aperture, whereas the same configurations when gilded produced intense heating.

DATA REDUCTION

The instrumentation at the beginning of this program was centered around a spectrophotometer-radiometer combination. Though the spectrophotometer produced a relative spectral curve of the radiation source, it was limited by a very narrow field of view. The radiometer, on the other hand, provided wide field of view but was incapable of producing a spectral curve, being a total radiometer. It was possible, however, to limit the response of the total

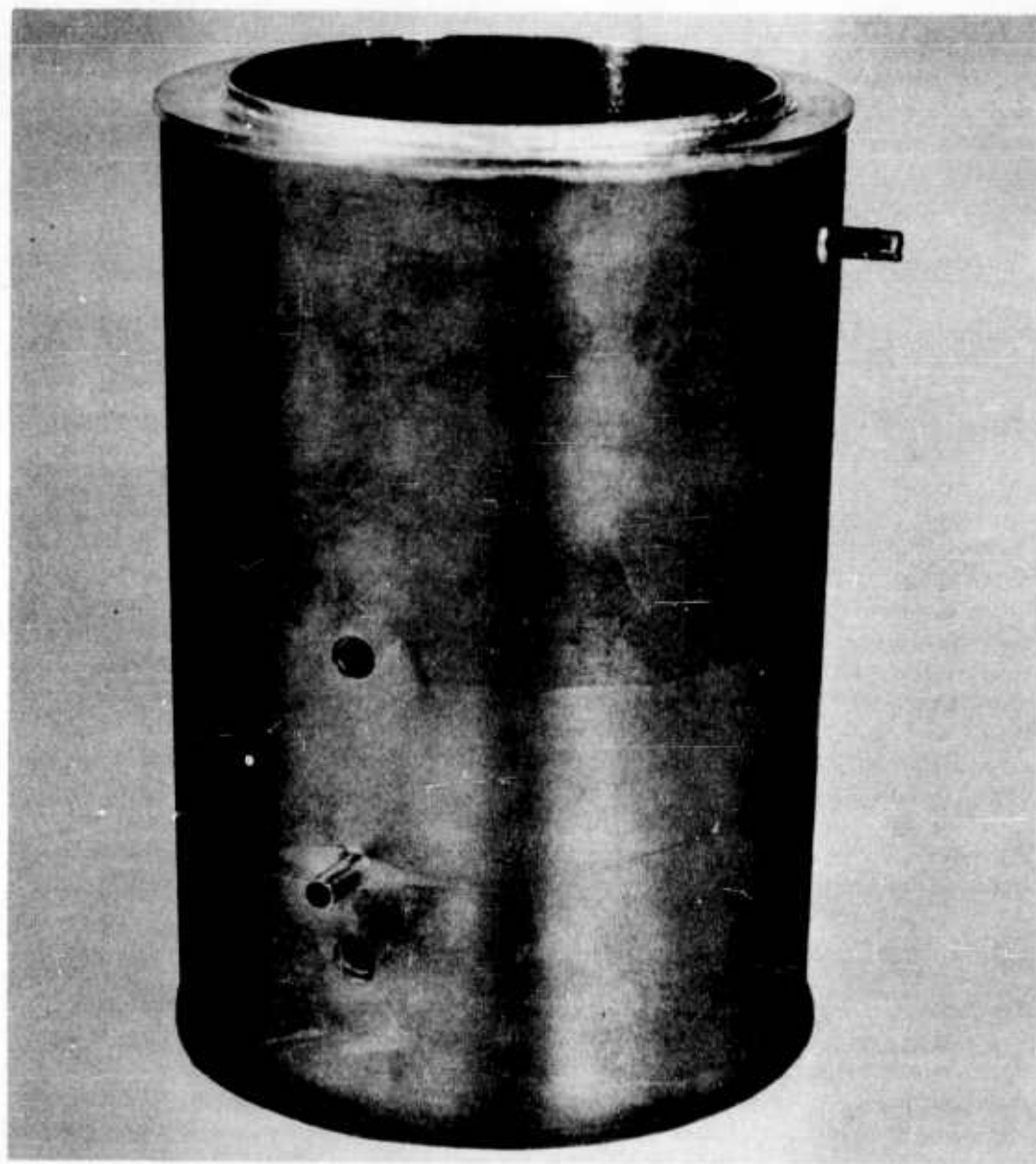


Figure 12. Cylinder.

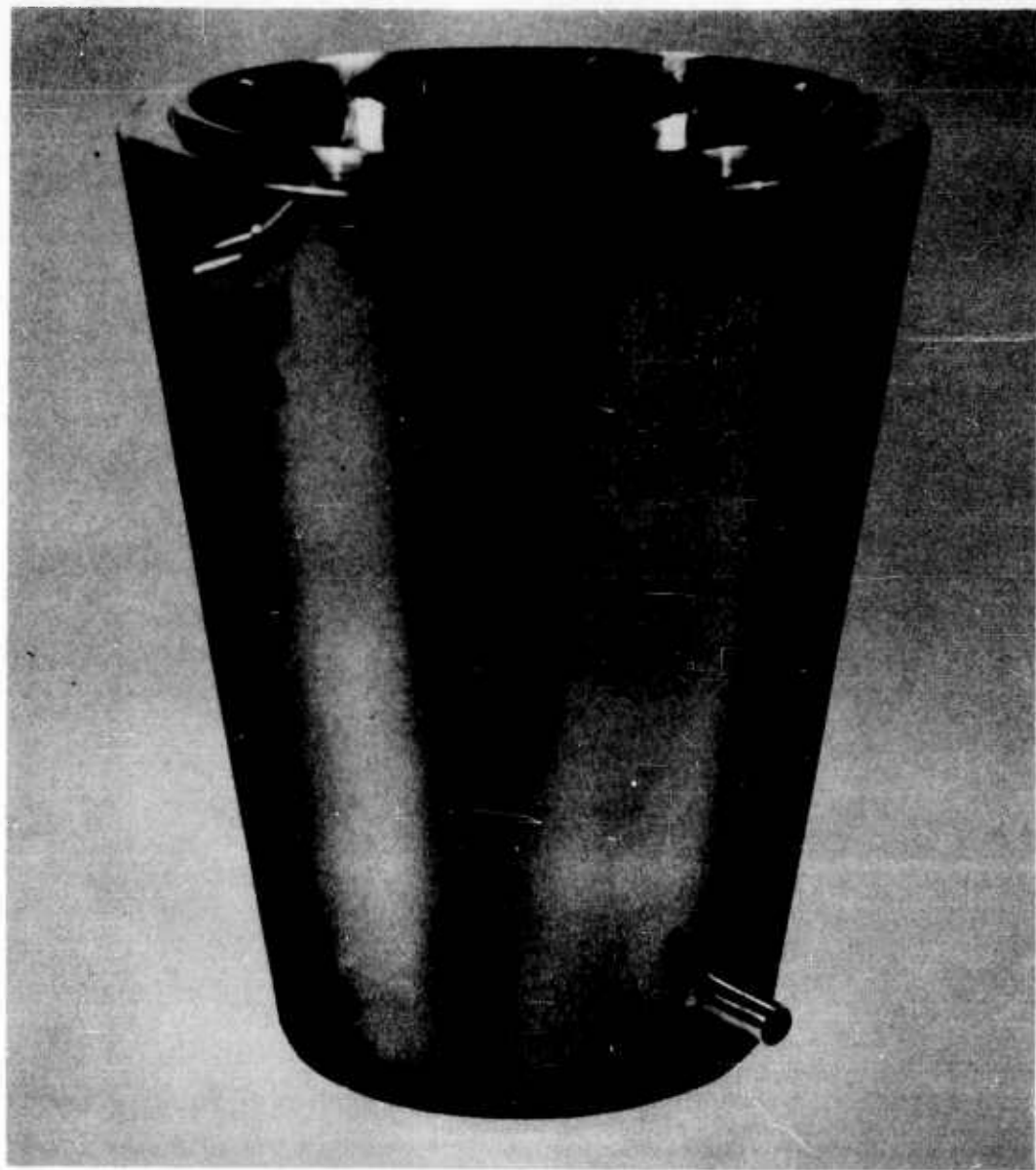


Figure 13. Reversible Frustum of a Cone.

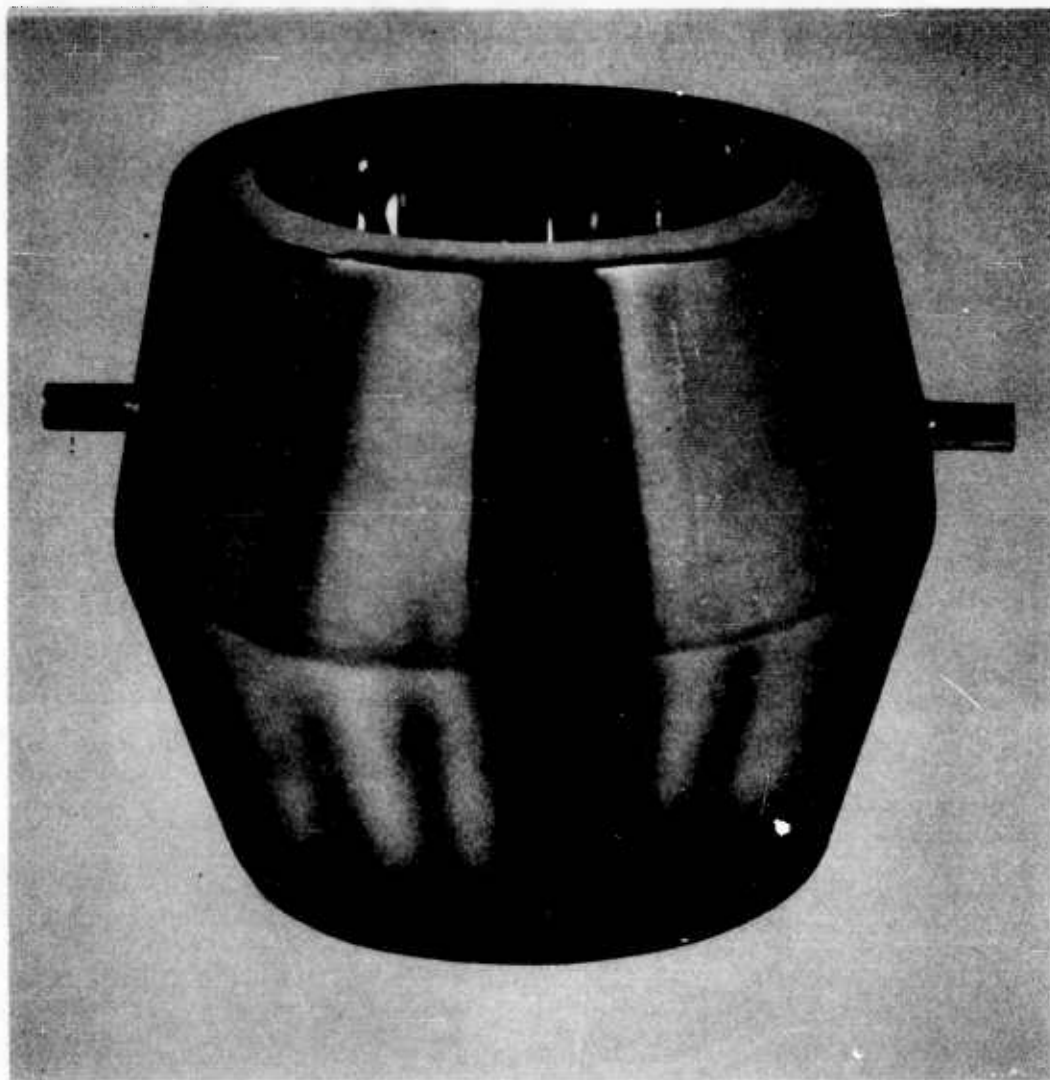


Figure 14. Two Opposed, Truncated Cones Having
a Common Diameter.

TABLE 2
MODEL CONFIGURATIONS STUDIED

Basic Configuration	Surface Finish	
	Basic Configuration	Spherical Innerbody
Cylinder	Gold	-
	Black	-
	Gold	Gold, Front
	Gold	Gold, Back
	Gold	Black, Front
	Gold	Black, Back
	Black	Gold, Front
	Black	Black, Front
Large Cone	Gold	-
	Black	-
	Gold	Gold
	Gold	Black
Small Cone	Gold	-
	Black	-
	Gold	Gold
	Gold	Black
Double Cone	Gold	-
	Black	-
	Gold	Gold
	Gold	Black

radiometer to narrow spectral bands through the use of band-pass interference filters. By selecting a set of filters whose peak wavelengths are closely spaced, it was possible to convert the total radiometer effectively into a spectral radiometer. The theory of this filter radiometer was derived for ideal field-of-view conditions. A set of field-of-view correction factors was determined for the actual radiometer. The theory of the filter radiometer, corrected for field of view, was incorporated into a computer program for reducing the experimental data.

Theory of Filter Radiometer

In view of the narrow spectral range of the band-pass filters and the concomitant reduced radiant energy reaching the detector, it was deemed desirable to investigate closely the operating principles of the filter radiometer and to account fully for the energy losses over the path from radiating source to the detector.

A total radiometer responds with a voltage output to radiation reaching the detector located in the focal plane of the collection optics. Thus, strictly speaking, the output voltage is a measure of the irradiation of the detector. The problem becomes that of relating the detector irradiation to some radiative property of the source, e. g., to the radiant intensity (watts/ster.) or the radiant emittance (watts/cm²).

The usual method employed in operating a total radiometer is to compare the voltage signal V_T produced by irradiation H_T from the target to the voltage signal V_B produced by irradiation H_B from a standard source whose spectral emittance is known. (The standard source is generally a black body source of specified temperature T .) The basic radiometer equation may be expressed as

$$\frac{H_T (\Delta \lambda, T')}{H_B (\Delta \lambda, T)} = \frac{V_T}{V_B} , \quad (1)$$

where $\Delta \lambda = \lambda_2 - \lambda_1$ indicates the wavelength interval to which the irradiation is limited and T' is the effective temperature of the target source. The accuracy to which the irradiation from the target source can be measured depends on the accuracy to which the irradiation from the black body can be determined, and, of course, on the accuracy to which V_T and V_B can be measured. The calculation of $H_B (\Delta \lambda, T)$ involves taking into account all factors which affect the radiation in the path between the black body source and the detector.

The major factors to be accounted for are the following:

- (1) Diminution of intensity by the inverse square effect.
- (2) Attenuation due to atmospheric scattering.
- (3) Attenuation due to atmospheric molecular absorption in certain wavelength bands.
- (4) Attenuation by losses on reflection at mirror surfaces.
- (5) Attenuation through band-pass filters.
- (6) Apparent diminution of intensity by non-uniform spectral response of the detector.

Except for the first factor, all the above are generally wavelength dependent. Thus, the problem reduces first to accounting for the spectral distribution of the irradiation on the detector and then to integrating over the appropriate band $\Delta \lambda$. Accordingly, the irradiation from the black body at temperature T is given by

$$H_B (\Delta \lambda, T) = \frac{\Omega}{\pi} \frac{A}{r^2} \int_{\Delta \lambda} \tau_s (\lambda) \tau_a (\lambda) \tau_f (\lambda) K (\lambda) S (\lambda) W_B (\lambda, T) d\lambda, \quad (2)$$

where

- | | |
|----------|---|
| Ω | is the solid angle subtended by the radiometer collecting mirror at the black body. |
| r | is the distance between black body and detector. |
| A | is the area of black body aperture. |
| τ_s | is the spectral transmittance of the atmosphere with regard to scattering. |

τ_a	is the spectral transmittance of the atmosphere with regard to molecular absorption.
τ_f	is the spectral transmittance of the band-pass filter, which defines $\Delta \lambda$.
$K(\lambda)$	is a reflection factor which accounts for combined losses at mirror surfaces in the radiometer collection optics.
$S(\lambda)$	is the normalized (at peak) spectral response of the detector over the range $\Delta \lambda$.
$W_B(\lambda, T)$	is the spectral emittance (Planck's equation) of the black body at wavelength λ .

By combining Eqs. (1) and (2), the irradiation of the detector by the target source is given by

$$H_T(\Delta \lambda, T', \theta) = \frac{V_T(\Delta \lambda, \theta)}{V_B(\Delta \lambda)} \frac{\Omega A}{\pi r^2} \int_{\Delta \lambda} \tau_s \tau_a \tau_f K(\lambda) S(\lambda) W_B(\lambda, T) d\lambda, (3)$$

where θ indicates the angle from the normal at which the target is viewed by the radiometer. * If no assumptions are allowed, Eq. (3) must be used as it stands to measure $H_T(\Delta \lambda, T', \theta)$, necessitating knowledge of all the parameters on the right-hand side. Since such knowledge is not often available or accurate, one is forced to make simplifying assumptions and compromises. Moreover, one is usually more interested in some radiation quantity at the radiating source; it thus remains to be found how closely Eq. (3) can be made to give a measure of a radiative property of the source.

Since no a priori assumptions are to be allowed concerning the spatial distribution of the radiance from the target, i.e., the radiance as a function of angle, one can write only the following

* It should be pointed out that Eq. (3), as it stands, gives no explicit information about the radiation at the target source, but that $V_T(\Delta \lambda, \theta)$ reflects variations in the spectral and spatial distributions of the target radiations over the range $\Delta \lambda$.

equation for the angular distribution of the spectral radiance of the target:*

$$N_{T\Omega}(\lambda, T', \theta) = N_{Tn\Omega}(\lambda, T) f(\theta), \quad (4)$$

where

$N_{Tn\Omega}(\lambda, T)$ is the normal spectral radiance at the target into the solid angle Ω centered about the normal n to the target, and

θ is the angle from the normal.

Thus, when Eq. (4) is integrated over the entire hemisphere (see Figure 15), one finds that the normal spectral radiance is related to the spectral emittance by

$$W_T(\lambda, T') = 2\pi N_{Tn\Omega}(\lambda, T') \int_0^{\pi/2} f(\theta) \sin \theta d\theta, \quad (5)$$

where the integration over ϕ has been performed. (Implicit assumption: the radiance does not depend on the azimuth angle ϕ) From Eq. (5) it follows that

$$N_{Tn\Omega}(\lambda, T') = \frac{1}{\pi} \frac{W_T(\lambda, T')}{2 \int_0^{\pi/2} f(\theta) \sin \theta d\theta} = \frac{1}{\pi} \frac{W_T(\lambda, T')}{k}, \quad (6)$$

where the constant $k = 2 \int_0^{\pi/2} f(\theta) \sin \theta d\theta$ will depend on the particular nature of the surface under observation. Thus, substituting Eq. (6) into Eq. (4) gives, for the angular dependence of the radiance

* The corresponding equation for a black body surface is Lambert's Law,

$$N_{B\Omega}(\lambda, T, \theta) = N_{Bn\Omega}(\lambda, T) \cos \theta$$

which, integrated over the hemisphere (2π solid angle), gives the well-known result

$$N_{Bn\Omega}(\lambda, T) = \frac{1}{\pi} W_B(\lambda, T)$$

relating the normal spectral radiance to the spectral emittance into the entire hemisphere.

at the target source, the equation

$$N_{T\Omega}(\lambda, T', \theta) = \frac{W_T(\lambda, T')}{\pi k} f(\theta), \quad (7)$$

the units of either side being watts/cm² - microns - steradian.

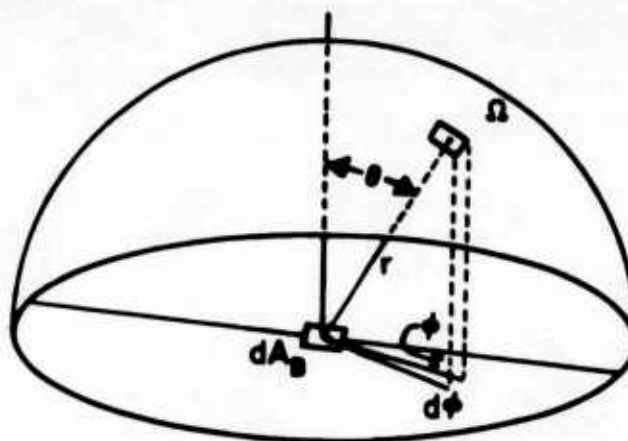


Figure 15. Solid Angle Ω in Direction θ from Normal.

It should be pointed out that, though the spectral quantities involved in Eqs. (4) through (7) exist for the target, they cannot be known beforehand and, indeed, cannot be inferred from a radiometer measurement over the single wavelength interval $\Delta\lambda$. However, knowing that the radiance function of the target exists at least in principle allows one to write for the target source an irradiation equation similar to Eq. (2) for the black body; i.e.,

$$H_T(\Delta\lambda, T'; \theta) = \frac{\Omega_T}{\pi} \frac{f(\theta)}{k} \frac{A_T}{r^2} \int_{\Delta\lambda} \tau_s \tau_a \tau_f K(\lambda) S(\lambda) W_T(\lambda, T') d\lambda, \quad (8)$$

where

A_T is the area of target,

Ω_T is the solid angle subtended by the radiometer collection optics at the target,

r_T is the distance between target and detector.

As the spatial distribution of the target source radiance approaches Lambert's Law, the factor $f(\theta)/k$ approaches $\cos \theta$; at any rate, the factor is absorbed by and taken into account by the radiometer voltage $V_T(\Delta \lambda, \theta)$ when the target is viewed at angle θ . Therefore, substituting Eq. (8) for $H_T(\Delta \lambda, T', \theta)$ in Eq. (3) produces the following result:

$$\frac{\Omega_T}{\pi} \frac{A_T}{r_T^2} \int_{\Delta \lambda} \tau_s \tau_a \tau_f K(\lambda) S(\lambda) W_T(\lambda, T') d\lambda =$$

$$\frac{V_T(\Delta \lambda, \theta)}{V_B(\Delta \lambda)} \frac{\Omega}{\pi} \frac{A}{r^2} \int_{\Delta \lambda} \tau_s \tau_a \tau_f K(\lambda) S(\lambda) W_B(\lambda, T) d\lambda. \quad (9)$$

From Eq. (9) it is immediately apparent that equal target-to-detector and black body-to-detector distances present an advantage, for the ratio Ω/r^2 , along with the factor $1/\pi$, cancels from both sides.

Equal target and black body distances have important implications with regard to quantities in the integrand, but caution must be observed before one may cancel any of them. It is convenient to consider each of the generally wavelength-dependent parameters individually.

- (1) First, consider the normalized spectral response of the detector. Obviously, the optimum spectral response curve is a step-function; i. e., the response of the detector is immediately full-valued at cut-on wavelength λ_1 , is constant (flat) over the interval $\Delta \lambda = \lambda_2 - \lambda_1$, and is immediately zero at cut-off wavelength λ_2 . The next best, and more physically realizable, response is that which varies only slowly with wavelength. Such is the case with thermistor bolometers; otherwise, one must determine experimentally the relative spectral response of the detector being used. Hence, if $S(\lambda)$ is

wavelength independent or only a slowly varying function of λ , over $\Delta\lambda$, it may be brought outside the integral and divided out of the equation.*

- (2) The factor $K(\lambda)$ depends on the spectral reflectivities of the various mirrors of the optical system involved in the experimental arrangement. If one uses front-surfaced mirrors with fresh coatings, a constant value of $K(\lambda)$ can be safely assumed. This assumption on $K(\lambda)$ is more plausible the narrower the wavelength interval $\Delta\lambda$. However, narrow $\Delta\lambda$ does not always insure a small change in the function over the band, as in the case of atmospheric transmission.
- (3) The attenuation due to the atmospheric medium is thought of as factorable into two parts: that caused by scattering and that caused by molecular absorption. For the latter, the transmission $\tau_a(\lambda)$ varies sharply with wavelength over well-known bands, even for small values of $\Delta\lambda$. One must exercise caution in treating $\tau_a(\lambda)$ as a slowly varying function except over the so-called atmospheric windows, where $\tau_a(\lambda)$ can be considered fairly constant.
- (4) The attenuation due to atmospheric scattering over short path lengths can be considered negligible. Moreover, the function $\tau_s(\lambda)$ exhibits no sharp changes in slope and, hence, over a narrow $\Delta\lambda$ may be considered constant.
- (5) Finally, consider the transmission of the limiting band-pass filter. Ideally, such a filter has a step-function transmission curve over $\Delta\lambda = \lambda_2 - \lambda_1$, but in practice the transmission curve has strong wavelength dependence. One usually has a recorder trace of $\tau_f(\lambda)$ to infer the wavelength dependence.

* Obviously, if applicable, this treatment applies for the other quantities within the integrand.

With these considerations, assuming a thermistor bolometer detector and freshly coated mirrors, Eq. (9) reduces to

$$\int_{\Delta\lambda} \tau_a(\lambda) \tau_f(\lambda) W_T(\lambda, T') d\lambda = \frac{V_T(\Delta\lambda, \theta)}{V_B(\Delta\lambda)} \frac{A}{A_T} \int_{\Delta\lambda} \tau_a(\lambda) \tau_f(\lambda) W_B(\lambda, T) d\lambda \quad (10)$$

from which $\tau_a(\lambda)$ may be factored when λ varies over an atmospheric window. Thus, one cannot hope to measure explicitly any radiative quantity at the target source, for Eq. (10) does not give the emittance (watts/cm²) of the target over the interval $\Delta\lambda$, giving instead an apparent emittance.

A value for the spectral emittance may, however, be deduced at the wavelength λ_m for which the product $\tau(\lambda) = \tau_a(\lambda) \tau_f(\lambda)$ is a maximum. In terms of the filter bandwidth $\Delta\lambda^*$, which is defined by

$$\Delta\lambda^* = \frac{\int_{\Delta\lambda} \tau(\lambda) d\lambda}{\tau(\lambda_m)}, \quad (11)$$

the spectral emittance (watts/cm² - micron) is given by

$$W_T(\lambda_m, T') = \frac{V_T(\Delta\lambda, \theta)}{V_B(\Delta\lambda)} \cdot \frac{A}{A_T} \cdot \frac{\int_{\Delta\lambda} \tau(\lambda) W_B(\lambda, T) d\lambda}{\tau(\lambda_m) \Delta\lambda^*}. \quad (12)$$

Equation (12) permits the plotting of the spectral emittance function of the target source if a series of closely spaced band-pass filters of narrow $\Delta\lambda$ is used with the radiometer. It should be mentioned that Eqs. (10) and (12) may be derived in terms of other radiation quantities, e.g., the radiance or radiant intensity, depending on target area A_T relative to the radiometer field of view. Equation (12) assumes ideal field-of-view conditions.

Radiometer Field of View

The area of a target source denoted by A_T includes the combined areas of all constituent surfaces projected perpendicular to the line of observation, i.e., as "seen" by the radiometer. Sources of radiant energy are classified under three types depending on size relative to the radiometer field of view. The classifications are the following:

- (1) The point source.
- (2) The extended source smaller than the field of view.
- (3) The extended source greater than the field of view.

All model shield configurations of this study presented target areas which fall under the second classification. The specification of radiant energy from such targets is appropriately made in terms of radiant intensity $J_T \Omega$, which is the radiant flux from the target area A_T into a unit solid angle.

Since the response of the radiometer is not uniform to all points within the field of view, a set of correction factors was determined for each different model aperture size. A map of the radiometer's field-of-view sensitivity contours is shown in Figure 10. These contours indicate that the response decreases as a point source moves off the central line of sight. This condition implies that the radiometer signal voltage is less than it should be otherwise for an extended uniform source which completely fills the field of view.

A correction factor can be derived from the sensitivity map and used to compensate partly the curtailment in response. The correction is derived by the following method: The outline of the target is superimposed upon the map of sensitivity contours, and the area elements A_i between adjacent contours (and between adjacent contours and the perimeter of the superimposed target outline, when the latter forms part of the desired boundary) were measured by means of a planimeter. Then, each A_i is divided by the total area A_s of the superimposed target outline to obtain the fraction value $w_i = A_i/A_s$. Each w_i is multiplied by the average sensitivity s_i between the two corresponding contours to produce the weighted sensitivity, $w_i s_i$. The reciprocal of the sum of all such weighted values is the desired correction factor, i.e.,

$$F = 1 / \sum_i w_i s_i . \quad (13)$$

The magnitude of F depends on the size and shape of the target source perimeter relative to the sensitivity map. The radiometer voltage signal V_T is increased by the factor F to compensate for the loss in response, i.e.,

$$V_T (\text{corrected}) = V_T (\text{measured}) \times F. \quad (14)$$

The variation of F with aspect angle θ is shown in Table 3 for each of the four model diameters. The correction factors $F(\theta)$ apply rigorously to a plane source whose emittance is uniform over the entire surface. For a target source area defined in the sense of A_T , i.e., two or more surfaces of different radiative characteristics, the $F(\theta)$ factors only approximately correct the radiometer voltage.

TABLE 3
FIELD-OF-VIEW CORRECTION FACTORS

Aspect Angle θ (degrees)	$F(\theta)$			
	Model Dia. 2.75 inches	Model Dia. 3.63 inches	Model Dia. 4.00 inches	Model Dia. 5.00 inches
0	1.06	1.10	1.11	1.18
10	1.06	1.08	1.10	1.28
20	1.06	1.09	1.14	1.25
30	1.05	1.08	1.09	1.25
40	1.05	1.07	1.09	1.23
50	1.04	1.07	1.08	1.23
60	1.04	1.06	1.07	-
70	1.04	1.06	1.03	-
80	1.04	-	-	-

Introducing the appropriate $F(\theta)$ factor as a multiplicative constant in Eq. (12) and using Eq. (11) for $\Delta\lambda^*$ yields for the spectral emittance at λ_m the following equation:

$$W_T(\lambda_m, \theta) = \frac{V_T(\Delta\lambda, \theta)}{V_B(\Delta\lambda)} \cdot F \cdot \frac{A}{A_T(\theta)} \cdot \frac{\int_{\Delta\lambda} \tau(\lambda) W_B(\lambda, T) d\lambda}{\tau(\lambda_m) \int_{\Delta\lambda} \tau(\lambda) d\lambda} \quad (15)$$

An expression for the spectral radiant intensity follows from Eq. (15) by dividing the product $AW_B(\lambda, T)$ by π , i.e.,

$$J_T(\lambda_m, \theta) = \frac{V_T(\Delta\lambda, \theta)}{V_B(\Delta\lambda)} \cdot F \cdot \frac{\int_{\Delta\lambda} \tau(\lambda) J_B(\lambda, T) d\lambda}{\tau(\lambda_m) \int_{\Delta\lambda} \tau(\lambda) d\lambda}, \quad (16)$$

denoting $A_T W(\lambda_m, \theta)$ by $J_T(\lambda_m, \theta)$. A filter factor was defined for each filter from Eq. (16) by the expression

$$f_J = \frac{\int_{\Delta\lambda} \tau(\lambda) J_B(\lambda, T) d\lambda}{\tau(\lambda_m) \int_{\Delta\lambda} \tau(\lambda) d\lambda} = \frac{A}{\pi} \cdot \frac{\int_{\Delta\lambda} \tau(\lambda) W_B(\lambda, T) d\lambda}{\tau(\lambda_m) \int_{\Delta\lambda} \tau(\lambda) d\lambda} \quad (17)$$

Computer Program for Data Reduction

Equation (16) was programed for the IBM 1620 computer to facilitate numerical calculation. The data reduction program was divided into the following three subroutines:

- (1) Calculation of spectral transmission of atmospheric water vapor.
- (2) Calculation of filter factors.
- (3) Calculation of spectral radiant intensity and of the total radiant intensity in a spectral band.

The spectral transmission of atmospheric water vapor was calculated, for the path length of 147 feet, from the Elsasser model for an H_2O absorption band. The Elsasser model is an approximate model in that the absorption band is assumed to consist of equally spaced absorption lines of equal intensity, each having the same Lorentz shape. On the basis of this model, the spectral absorption $\nu_a(\lambda)$ is given by the error function

$$\nu_a(\lambda) = \text{erf} [X(\lambda)], \quad (18)$$

where the argument $X(\lambda)$ is given by

$$X(\lambda) = \frac{1}{2} \beta(\lambda) \sqrt{\pi H} . \quad (19)$$

The wavelength dependent parameter $\beta(\lambda)$ is called the generalized absorption coefficient. Tables or curves of $\beta(\lambda)$ are available,* though they may be approximate for a particular application. Representing the precipitable centimeters of H_2O contained in the volume defined by the path length and unit cross section, the parameter H depends on the temperature, pressure, and relative humidity of the local atmosphere. Nomograms of these interrelated physical parameters are available for obtaining H .** The inputs $\beta(\lambda)$ and H permit determination of the spectral absorption over the desired wavelength intervals, which in the present case are defined by the spectral width $(\Delta\lambda)_n$ for each of the filters ($n = 1, 2, \dots, 18$). (See Figure 16.) The spectral absorption over each wavelength interval $\Delta\lambda$ is made more amenable to computation by the series form

$$\text{erf} [X(\lambda)] = \frac{2}{\pi} X(\lambda) \sum_{\kappa=0}^{\infty} \frac{(-1)^{\kappa+2} X(\lambda)^{2\kappa}}{\kappa! (2\kappa+1)} . \quad (20)$$

The spectral transmission $\tau_a(\lambda)$ follows from the relation

$$\tau_a(\lambda) = 1 - \nu_a(\lambda) = 1 - \text{erf} [X(\lambda)] . \quad (21)$$

It must be pointed out that Eq. (21) accounts only for H_2O absorption in the atmosphere. However, where the inputs corresponding to $\beta(\lambda)$ are available for the spectral bands of interest, a similar equation can be applied for CO_2 absorption. The spectral transmission $\tau_f(\lambda)$ for each filter was read directly from curves furnished by the manufacturer. Table 4 presents the wavelength interval $\Delta\lambda$ and the bandwidth $\Delta\lambda^*$ for each of the 18 filters.

The point-by-point product of $\tau_a(\lambda)$ and $\tau_f(\lambda)$ was obtained at .05 micron for each filter, and the resulting peak transmittance $\tau(\lambda)$ was noted. The integrations indicated in Eq. (17) for the

* Rand Confidential Report RM-784.

** J. N. Howard, D. L. Burch, D. Williams, "Near-Infrared Transmission Through Synthetic Atmospheres", Geophysical Research Papers No. 40, AFCRC-TR-55-213, p. 89.

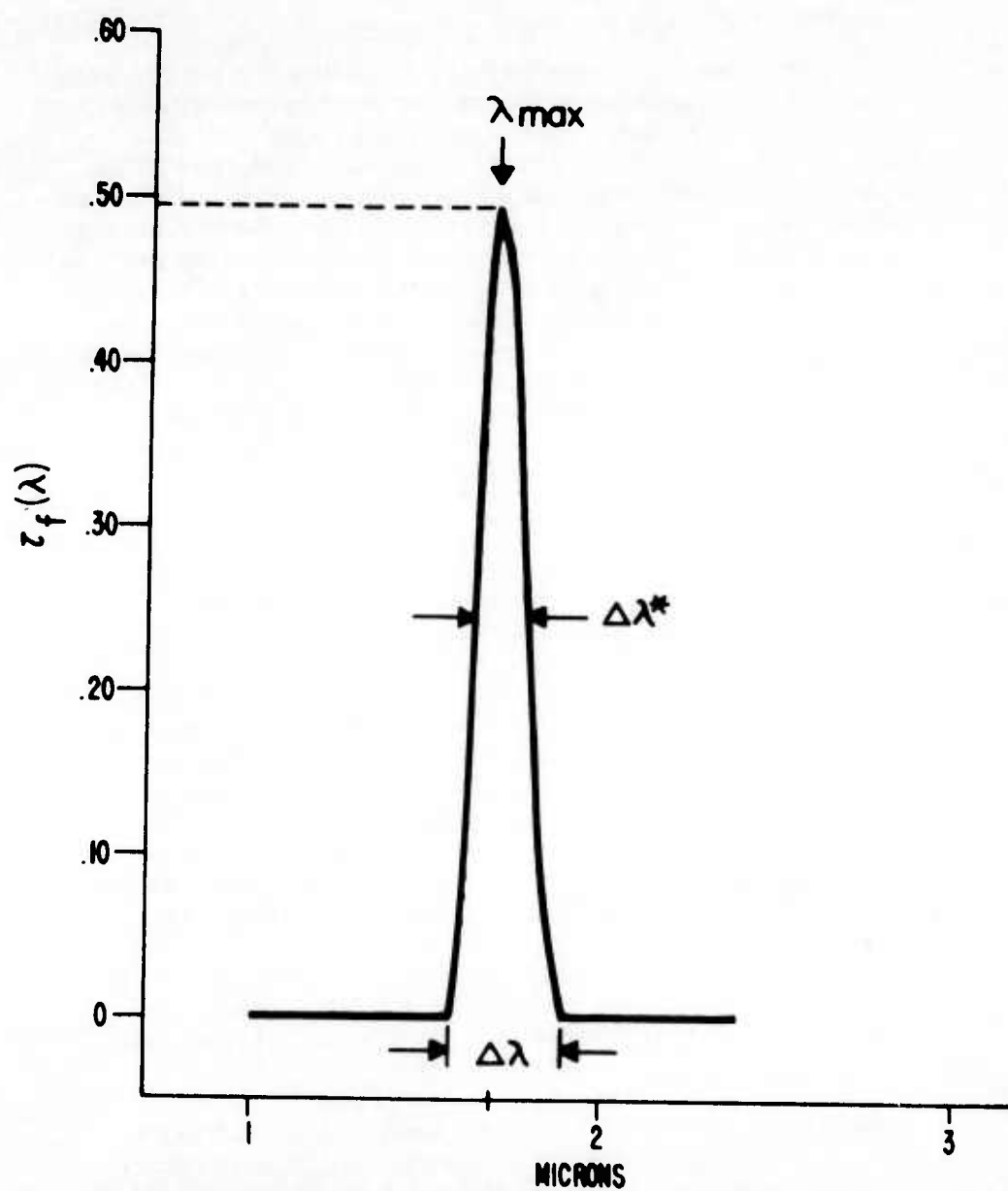


Figure 16. Spectral Transmission Curve for the First ($n = 1$) Band-Pass Filter.

TABLE 4
INTERFERENCE FILTER DATA

Filter Number	Bandwidth $\Delta \lambda^*$ (microns)	Total Width $\Delta \lambda$ (microns)
1	.13	.31
2	.07	.15
3	.07	.23
4	.09	.21
5	.09	.15
6	.08	.17
7	.10	.26
8	.10	.21
9	.09	.26
10	.10	.28
11	.12	.31
12	.13	.28
13	.12	.28
14	.12	.30
15	.13	.28
16	.10	.25
17	.13	.29
18	.12	.34

filter factors were approximated by Simpson's rule. Table 6 presents the filter factors f_j and the peak wavelength λ_m for each filter.

The IBM 1620 was programed to compute the spectral radiant intensity from the abbreviated equation

$$J_T(\lambda_m) = (V_T/V_B) \cdot f_j \cdot F. \quad (22)$$

The experimentally determined voltage ratio V_T/V_B for each filter, angle, and shield configuration, the f_j factor for each filter, and the factor F for each angle and shield aperture were the required inputs. Unsmoothed plots of Eq. (22) for two different shield conditions are shown in Figure 17. It should be noted that the points in the neighborhood of 4.3 microns and 2.7 microns are probably too low, because CO_2 absorption is unaccounted for in these plots.

As indicated by the plots, the points are not spaced at uniform intervals along the wavelength scale. Accordingly, the area under the $J_T(\lambda)$ curve was integrated by the trapezoidal rule for the total radiant intensity in the wavelength interval from 1.68 microns to 5.16 microns.

PRESENTATION OF RESULTS

The reduced data from the experimental program are presented in Table 5. This tabulation correlates the total radiant intensity in the region of interest and the angle of aspect for each model configuration studied. It will be noted that most of the radiant intensities appearing in the form printed by the computer have eight digits followed by the letter "E" and a negative number. The "E" stands for base - 10 exponent. A number in this notation such as .42779843E-2 means $.42779843 \times 10^{-2}$. Of the eight digits, only about four are significant figures; consequently, where revisions were made after computer reduction, the calculations are shown to four figures only.

The data are also shown in graphical form in Figures 19 through 39. The graphs were plotted on logarithmic polar paper because of the wide ranges of radiant intensity encountered. The cylindrical geometry of the models eliminated the necessity of measurements

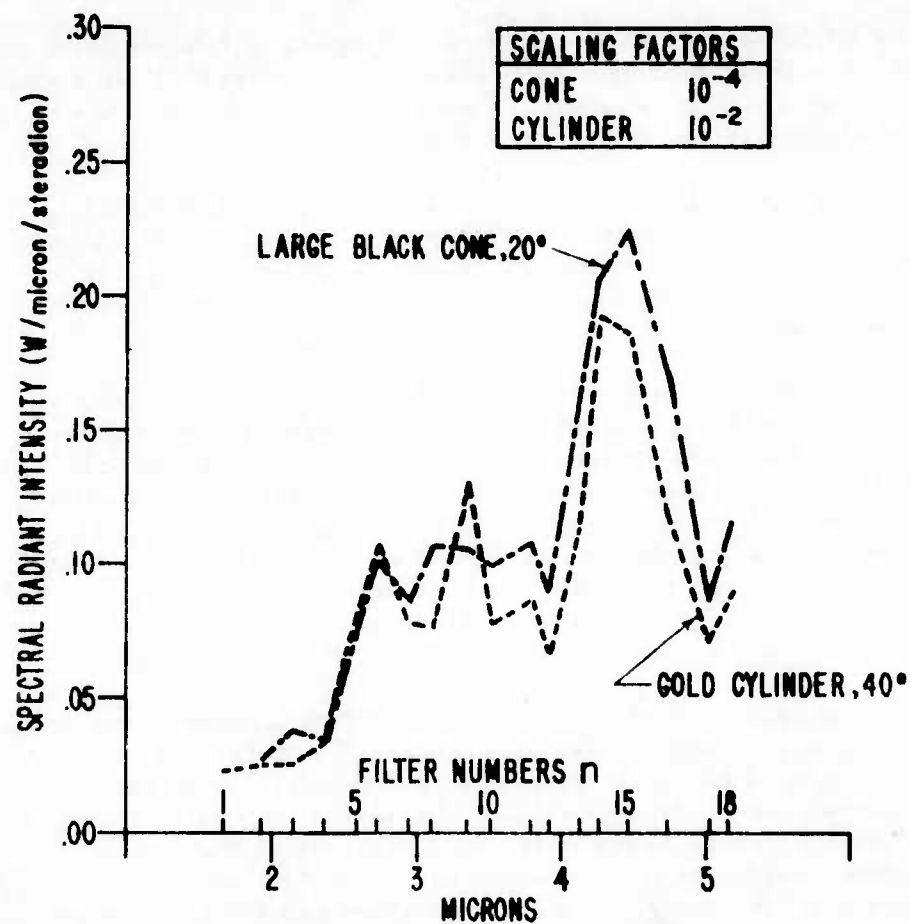


Figure 17. Unsmoothed Spectral Radiant Intensity for Two Shield Configurations.

in two quadrants.

Figure 19 shows the close agreement between the laboratory measurements and the computer predictions for the gold cylinder and the remarkable approximation of both to the cosine curve of a Lambert radiator. Comparison of this figure with Figure 11 indicates that the gold cylinder closely approximated a perfect reflector.

Figure 20 demonstrates the pronounced effect of coating the reflector with a low reflectivity material. The restricted angular spread indicates that essentially only that radiation which was not reflected contributed to the total radiative output.

Figures 21 and 22 indicate that the addition of a high reflectivity spherical innerbody does not greatly alter the radiative pattern of the basic cylinder, except for a somewhat enhanced rate of attenuation. The position of the innerbody along the axis is apparently not critical.

Figures 26 and 27 show both the total radiant intensity over the whole region of interest and the radiant intensity within the very narrow band pass of a single filter. It is interesting to note that the difference between the logarithms of the radiant intensities (or the linear difference when plotted on logarithmic paper) is constant. This enables one to infer the total intensity at levels too low for measurement if one can measure any subregion within the total region. This characteristic was used several times to indicate the shape of a curve at low intensities.

An interesting observation was made in connection with the large and small gold cones, shown in Figures 27 and 31. Despite the large amount of radiation gathered by the small cone, the normal intensity was only about one-third the normal intensity from the large cone which gathered only about three-tenths as much radiation from the plate. (See Figure 18.) The small arrows represent some arbitrary unit of radiation gathered by the cone. The apparent paradox was resolved by observing that the radiation pattern of the small cone was spread out over the entire quadrant, whereas the pattern of the large cone was concentrated in only one-half the quadrant. The small cone was observable around to

88° with measurable signals to 80°, while the large cone was observable to only 43° with readable signals to 40°.

The effect of blackening the large cone is shown in Figure 30. The angular spread has been reduced from that of the corresponding gold model, and the axial intensity has been reduced by a factor of about 2.5.

It is felt that the irregularities exhibited in Figure 32 reflect the experimental error. A tolerance of 10% would permit the drawing of a smooth curve similar to that of Figure 31 except for an over-all attenuation.

As might be expected, the radiative pattern of the small black cone (Figure 34) is very similar to that of the large black cone (Figure 30). In both cases the reflected radiation is almost negligible and the limiting aperture is the small end of the reversible cone.

Figure 35 is interesting for the lobe occurring at 50°. An attempt to account for this observation was made by plotting the sum of the patterns for the large and small gold cones, since the geometry of the double cone could be qualitatively reproduced by joining the front half of the small cone to the rear half of the large cone. The resulting pattern, shown in Figure 36, does indeed exhibit the same characteristic shape.

Figure 39 shows the pronounced effect of the black innerbody in the double cone when viewed along the axis. This double cone configuration is unique in that the innerbody intercepts all radiation from the source plate which is not reflected by the model itself.

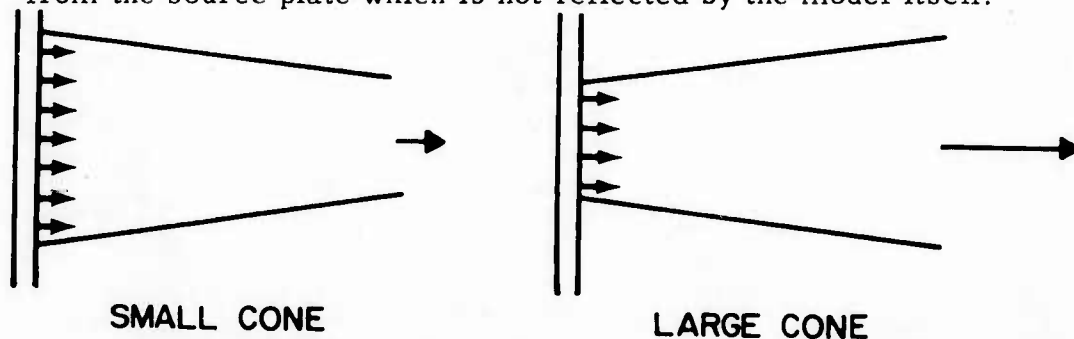


Figure 18. Normal Radiation from Gold Cones.

TABLE 5
EXPERIMENTAL MEASUREMENTS OF RADIANT INTENSITIES

Configuration	Radiant Intensity (watts/ster.)	Angle
Gold Cylinder	.4277E-2	0°
	.4012E-2	10°
	.4102E-2	20°
	.3454E-2	30°
	.3093E-2	40°
	.2540E-2	50°
	.1728E-2	60°
	.9664E-3	70°
Black Cylinder	.3112E-2	0°
	.1836E-2	10°
	.4397E-3	20°
Gold Cylinder and Gold Innerbody, Front Position	.2210E-2	0°
	.2201E-2	10°
	.1905E-2	20°
	.1659E-2	30°
	.1178E-2	40°
	.7518E-3	50°
	.3438E-3	60°
	.7898E-4	70°
Gold Cylinder and Gold Innerbody, Back Position	.1942E-2	0°
	.1912E-2	10°
	.1973E-2	20°
	.1687E-2	30°
	.1240E-2	40°
	.6149E-3	50°
	.3143E-3	60°
	.9587E-4	70°

TABLE 5 (CONT'D)
EXPERIMENTAL MEASUREMENTS OF RADIANT INTENSITIES

Configuration	Radiant Intensity (watts/ster.)	Angle
Gold Cylinder and Black Innerbody, Front Position	.1186E-2	0°
	.1155E-2	10°
	.1161E-2	20°
	.8861E-3	30°
	.5418E-3	40°
	.3150E-3	50°
	.1787E-3	60°
Gold Cylinder and Black Innerbody, Back Position	.1330E-2	0°
	.1126E-2	10°
	.1082E-2	20°
	.8960E-3	30°
	.4313E-3	40°
	.2639E-3	50°
	.1059E-3	60°
Black Cylinder and Gold Innerbody, Front Position	.1091E-2	0°
	.2954E-3	10°
Black Cylinder and Black Innerbody, Front Position	.1164E-2	0°
	.2190E-3	10°
Large Gold Cone	.4979E-2	0°
	.5297E-2	10°
	.4795E-2	20°
	.3356E-2	30°
	.1681E-3	40°

TABLE 5 (CONT'D)
EXPERIMENTAL MEASUREMENTS OF RADIANT INTENSITIES

Configuration	Radiant Intensity (watts/ster.)	Angle
Large Gold Cone and Gold Innerbody	.2645E-2	0°
	.2618E-2	10°
	.2055E-2	20°
	.1156E-2	30°
	.2373E-3	40°
Large Gold Cone and Black Innerbody	.1668E-2	0°
	.1485E-2	10°
	.1139E-2	20°
	.4905E-3	30°
Large Black Cone	.2008E-2	0°
	.1637E-2	10°
	.3602E-3	20°
Small Gold Cone	.1541E-2	0°
	.1499E-2	10°
	.1324E-2	20°
	.1232E-2	30°
	.1050E-2	40°
	.8332E-3	50°
	.6973E-3	60°
	.4220E-3	70°
Small Gold Cone and Gold Innerbody	.1722E-3	80°
	.1194E-2	0°
	.1218E-2	10°
	.1013E-2	20°
	.9409E-3	30°
	.6923E-3	40°
	.7080E-3	50°
	.5039E-3	60°
	.2493E-3	70°

TABLE 5 (CONT'D)
EXPERIMENTAL MEASUREMENTS OF RADIANT INTENSITIES

Configuration	Radiant Intensity (watts/ster.)	Angle
Small Gold Cone and Black Innerbody	.6625E-3	0°
	.5548E-3	10°
	.5197E-3	20°
	.6005E-3	30°
	.5102E-3	40°
	.3608E-3	50°
	.2371E-3	60°
	.1103E-3	70°
Small Black Cone	.1410E-2	0°
	.1409E-2	10°
	.4892E-3	20°
Gold Double Cone	.3048E-2	0°
	.3074E-2	10°
	.2802E-2	20°
	.2078E-2	30°
	.1315E-2	40°
	.1420E-2	50°
	.1087E-2	60°
	.1864E-3	70°
Gold Double Cone and Gold Innerbody	.1048E-2	0°
	.9314E-3	10°
	.1003E-2	20°
	.1163E-2	30°
	.1116E-2	40°
	.7260E-3	50°
	.2247E-3	60°

TABLE 5 (CONT'D)
EXPERIMENTAL MEASUREMENTS OF RADIANT INTENSITIES

Configuration	Radiant Intensity (watts/ster.)	Angle
Gold Double Cone and Black Innerbody	.1995E-3	0°
	.4669E-3	10°
	.5465E-3	20°
	.5502E-3	30°
	.4544E-3	40°
	.1973E-3	50°
Black Double Cone	.2247E-2	0°
	.1397E-2	10°
	.6576E-3	20°
	.8148E-4	30°

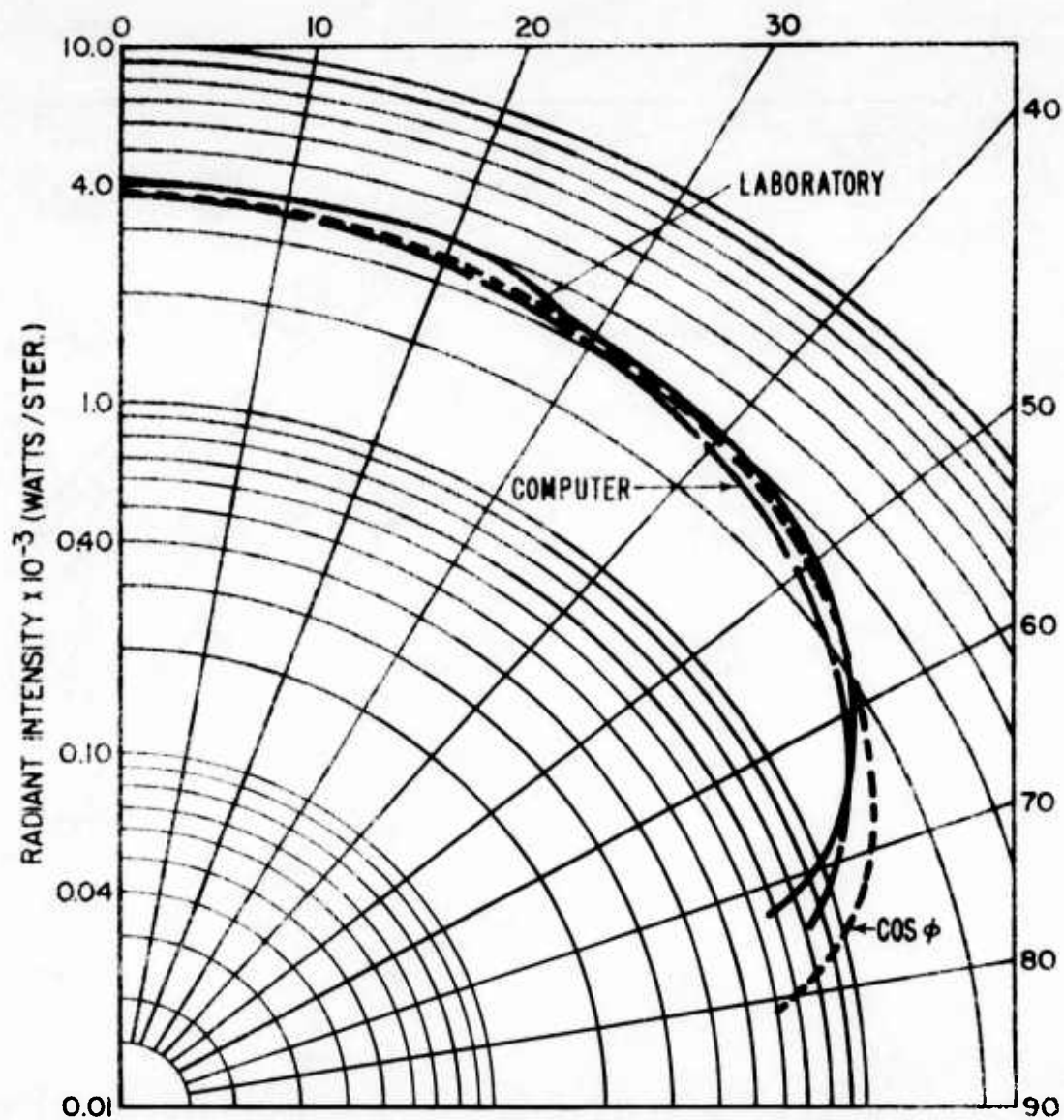


Figure 19. Gold Cylinder, No Innerbody.

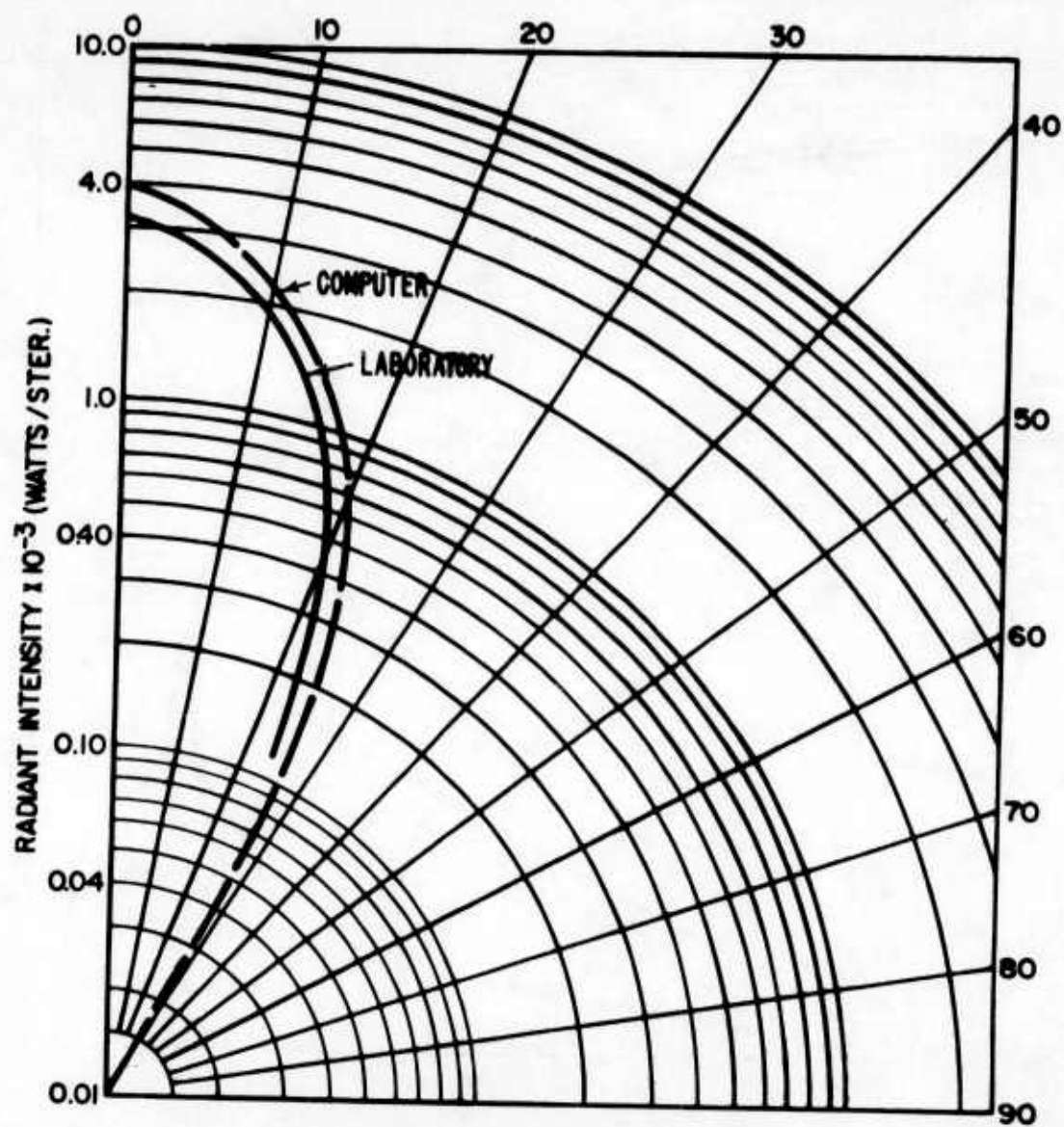


Figure 20. Black Cylinder, No Innerbody.

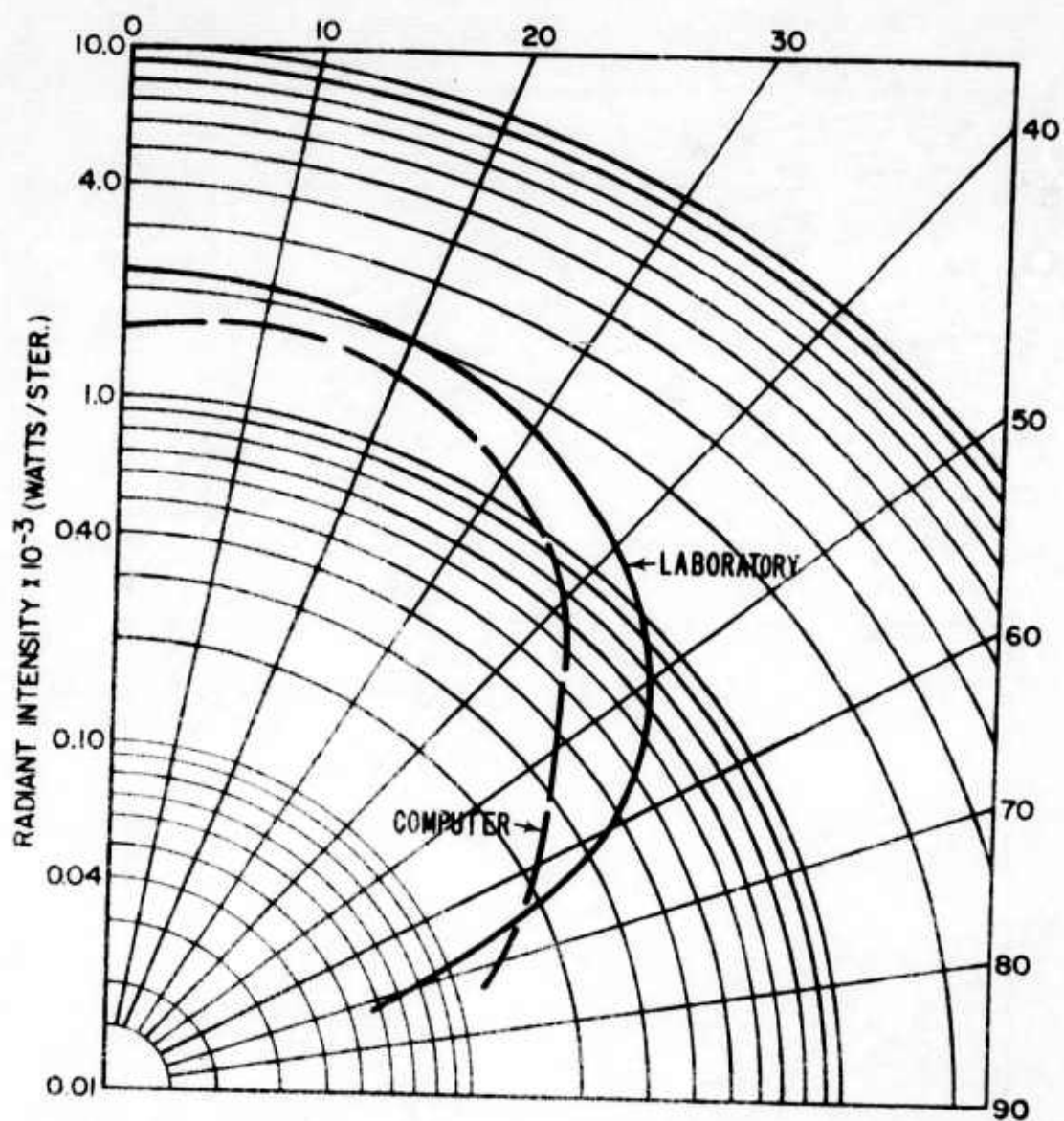


Figure 21. Gold Cylinder and Gold Innerbody, Front Position.

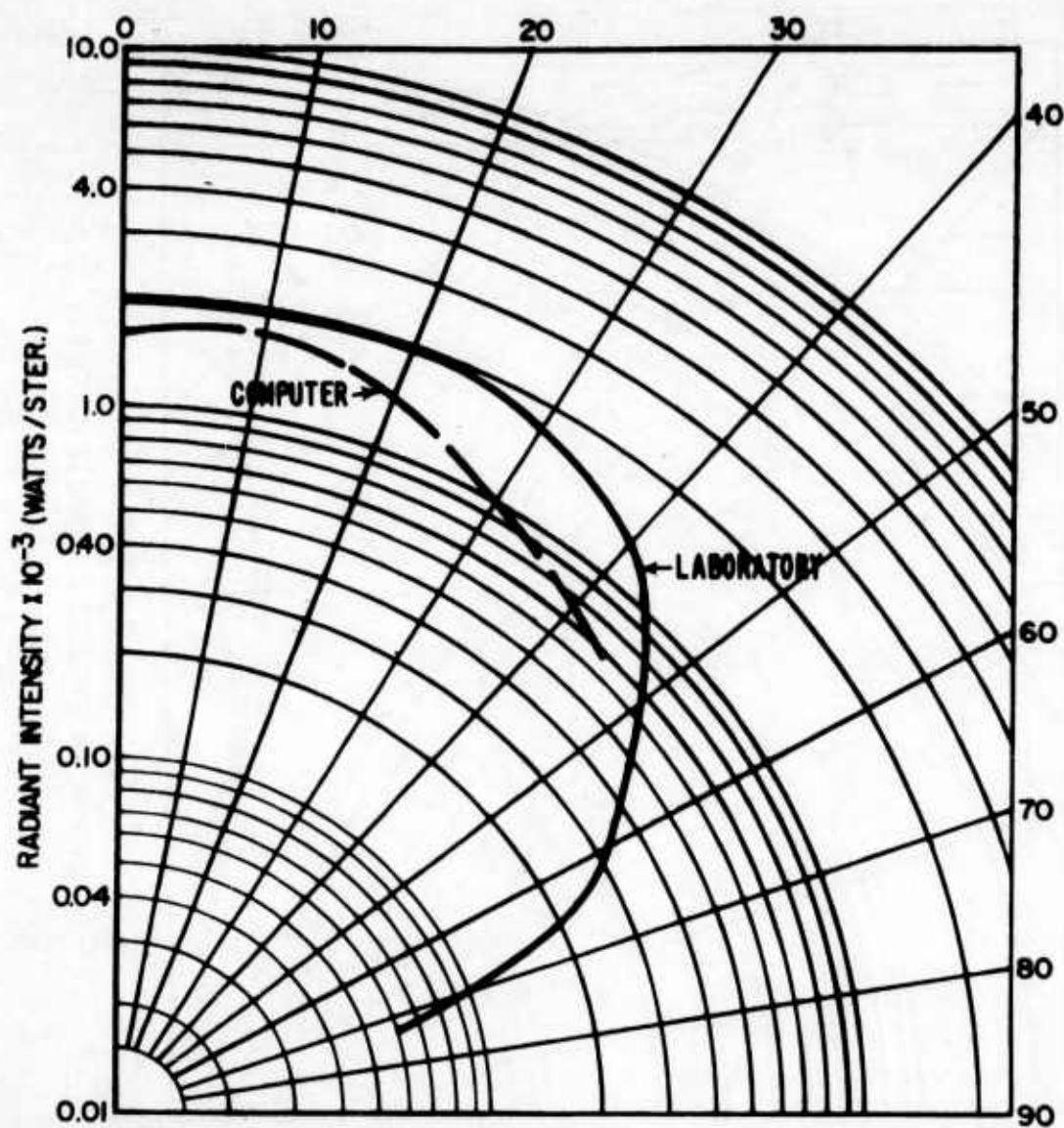


Figure 22. Gold Cylinder and Gold Innerbody,
Back Position.

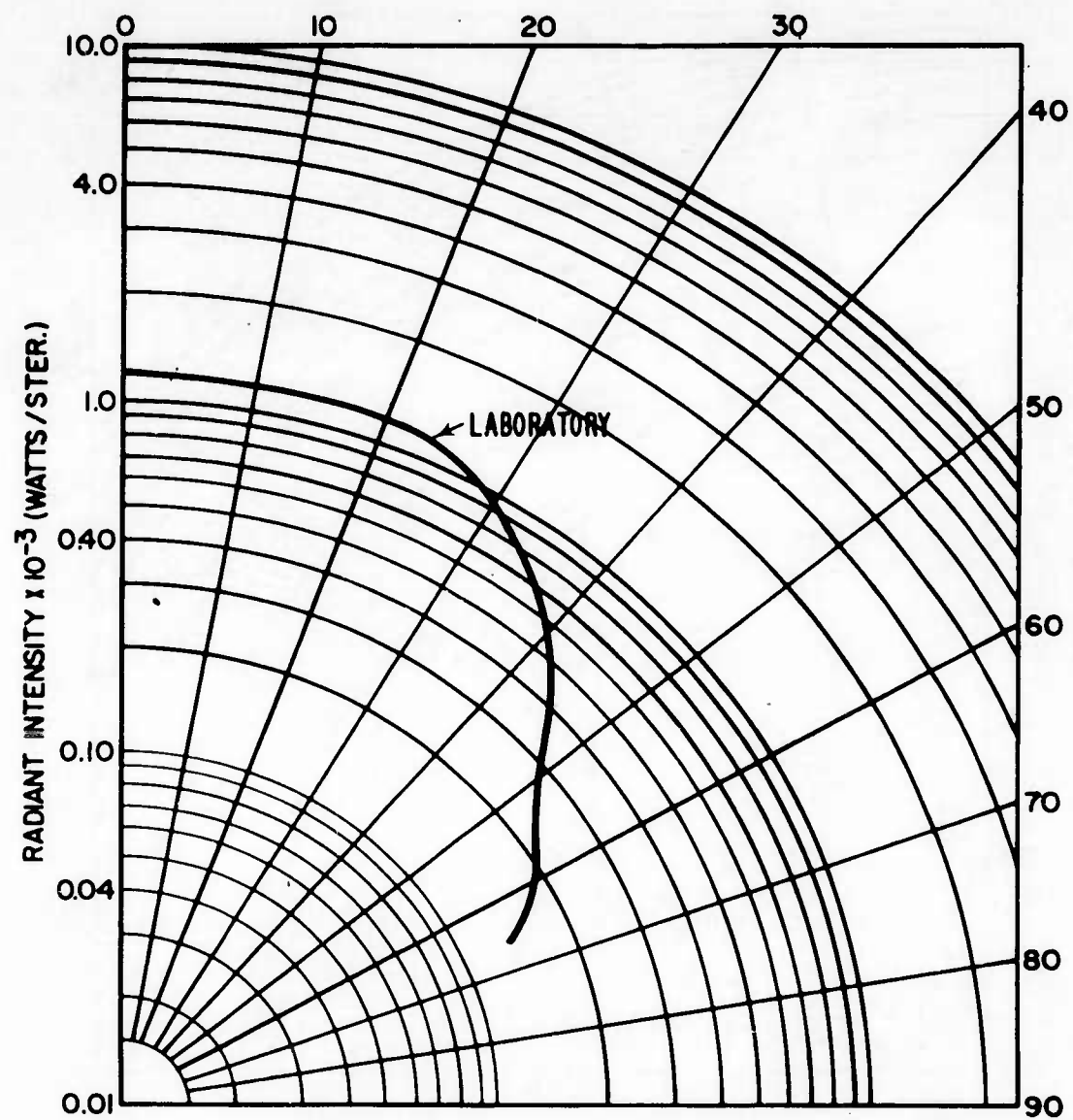


Figure 23. Gold Cylinder and Black Innerbody,
Front Position.

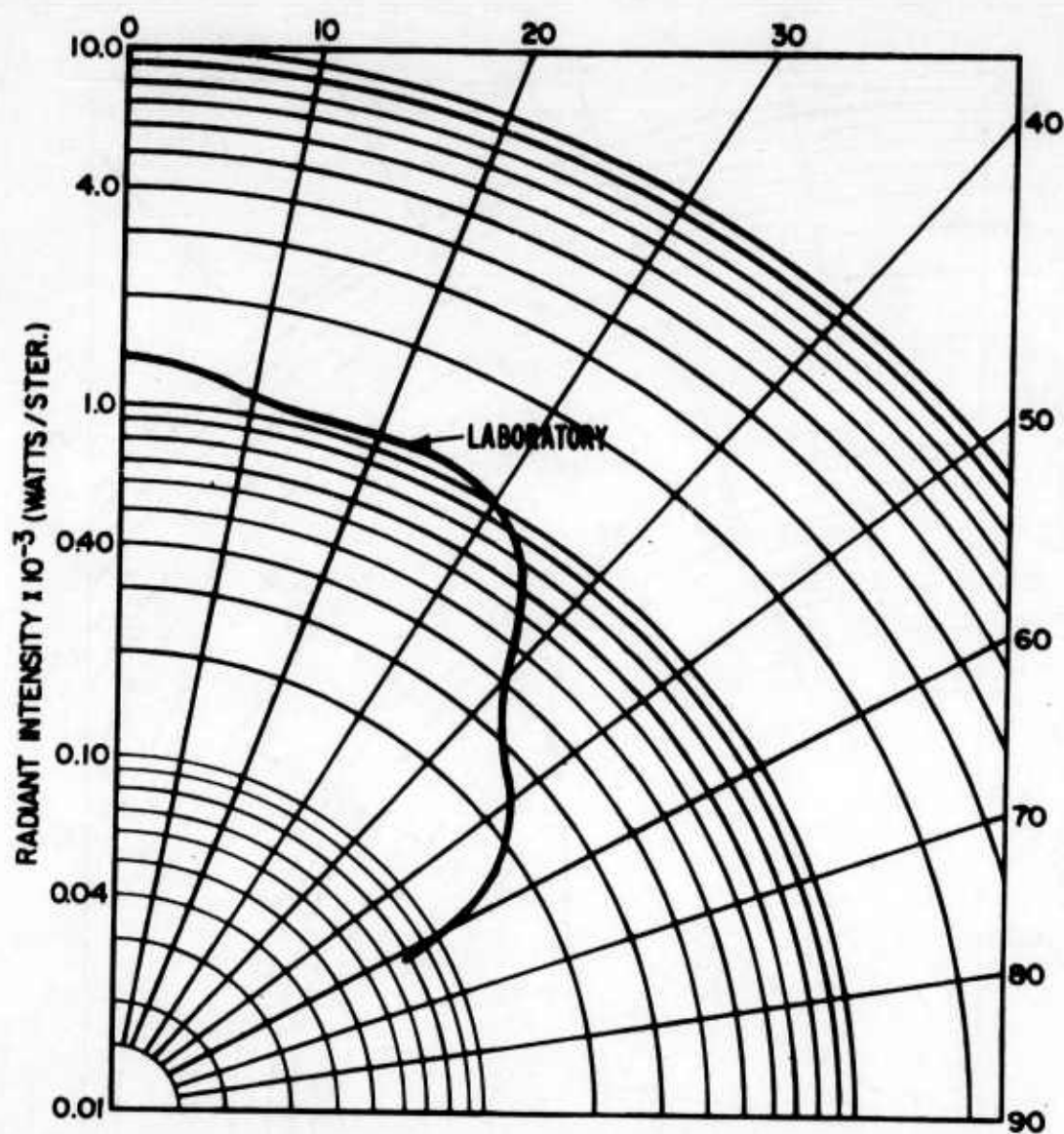


Figure 24. Gold Cylinder and Black Innerbody,
Back Position.

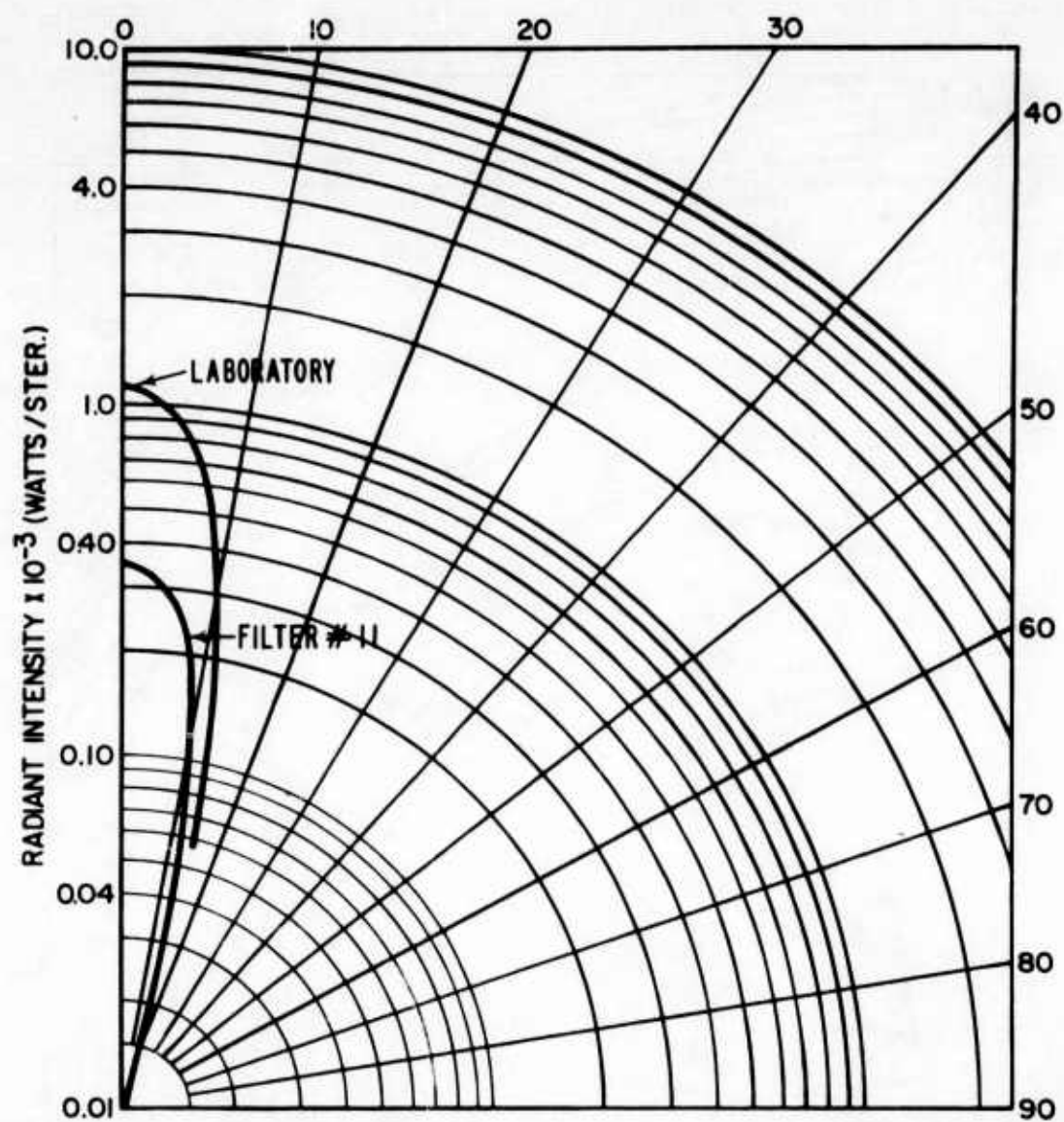


Figure 25. Black Cylinder and Gold Innerbody, Front Position.

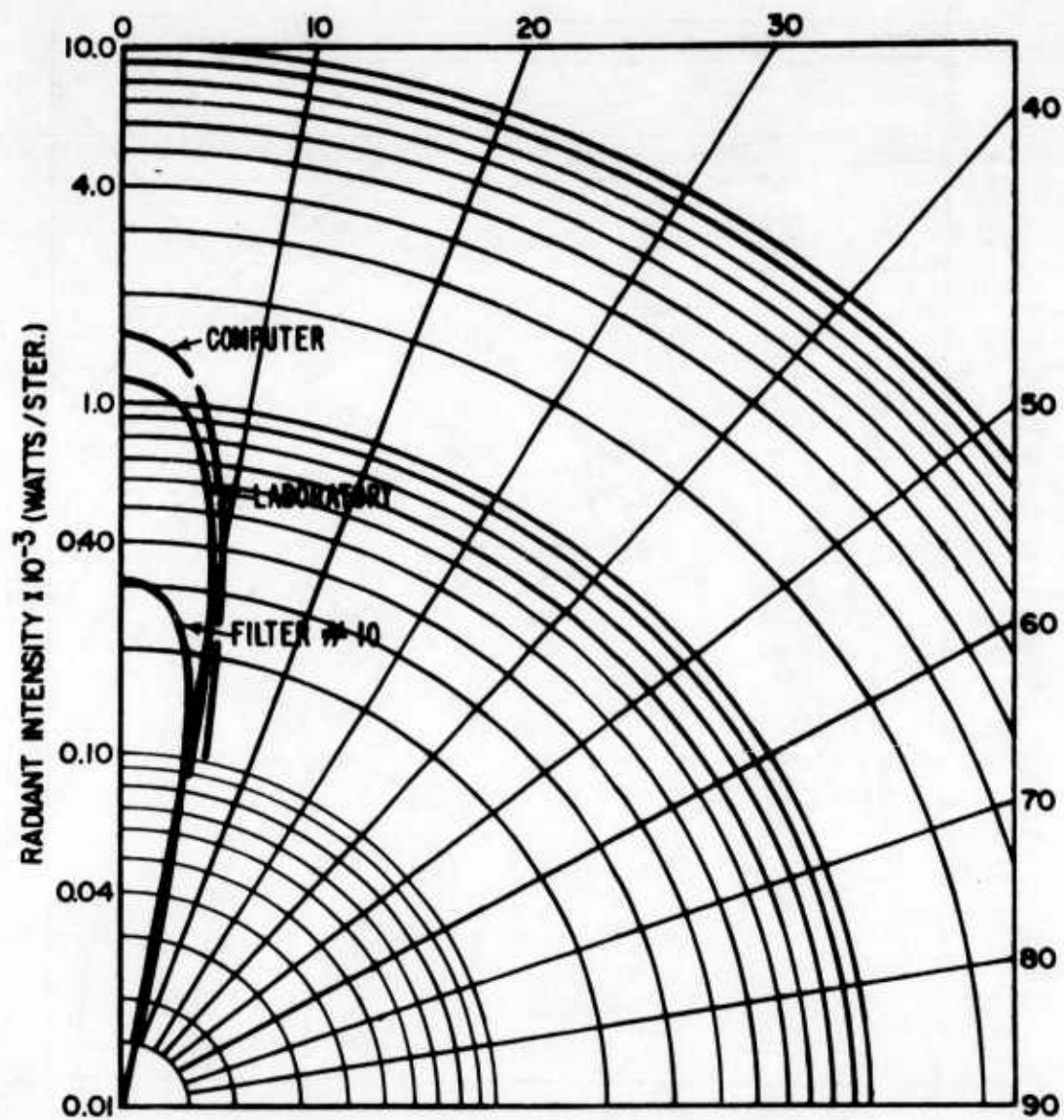


Figure 26. Black Cylinder and Black Innerbody, Front Position.

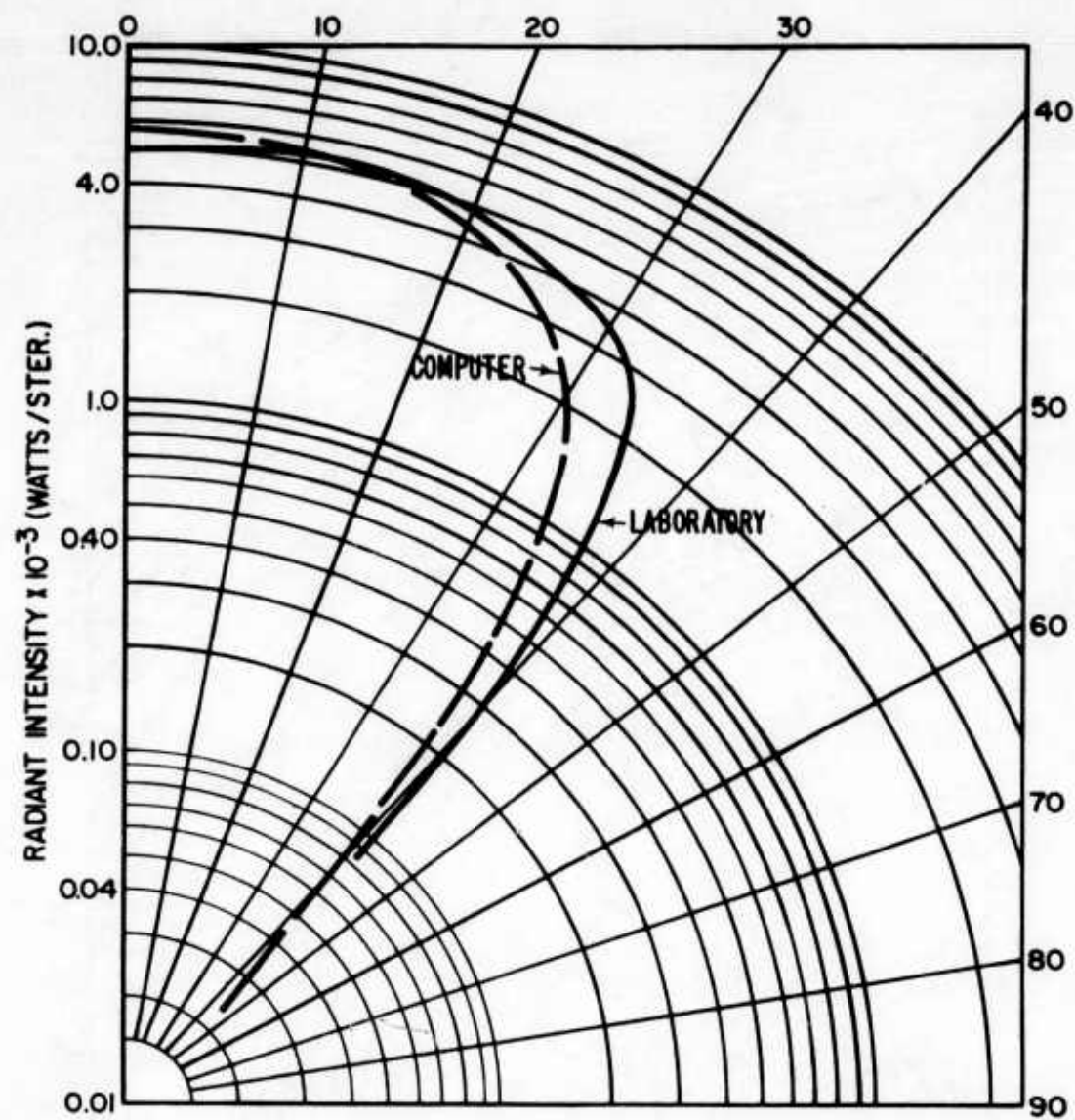


Figure 27. Gold Large Cone, No Innerbody.

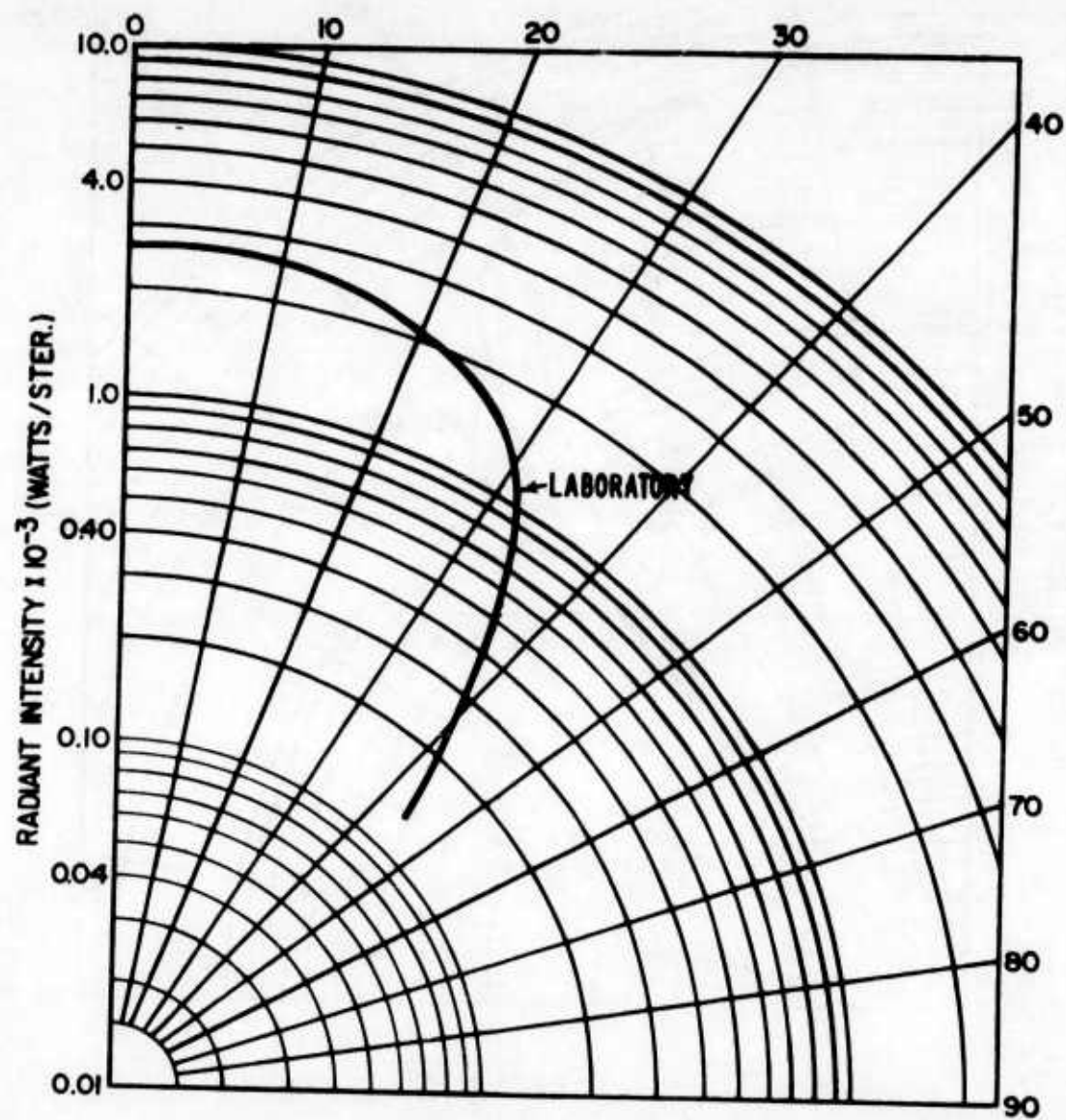


Figure 28. Gold Large Cone, Gold Innerbody.

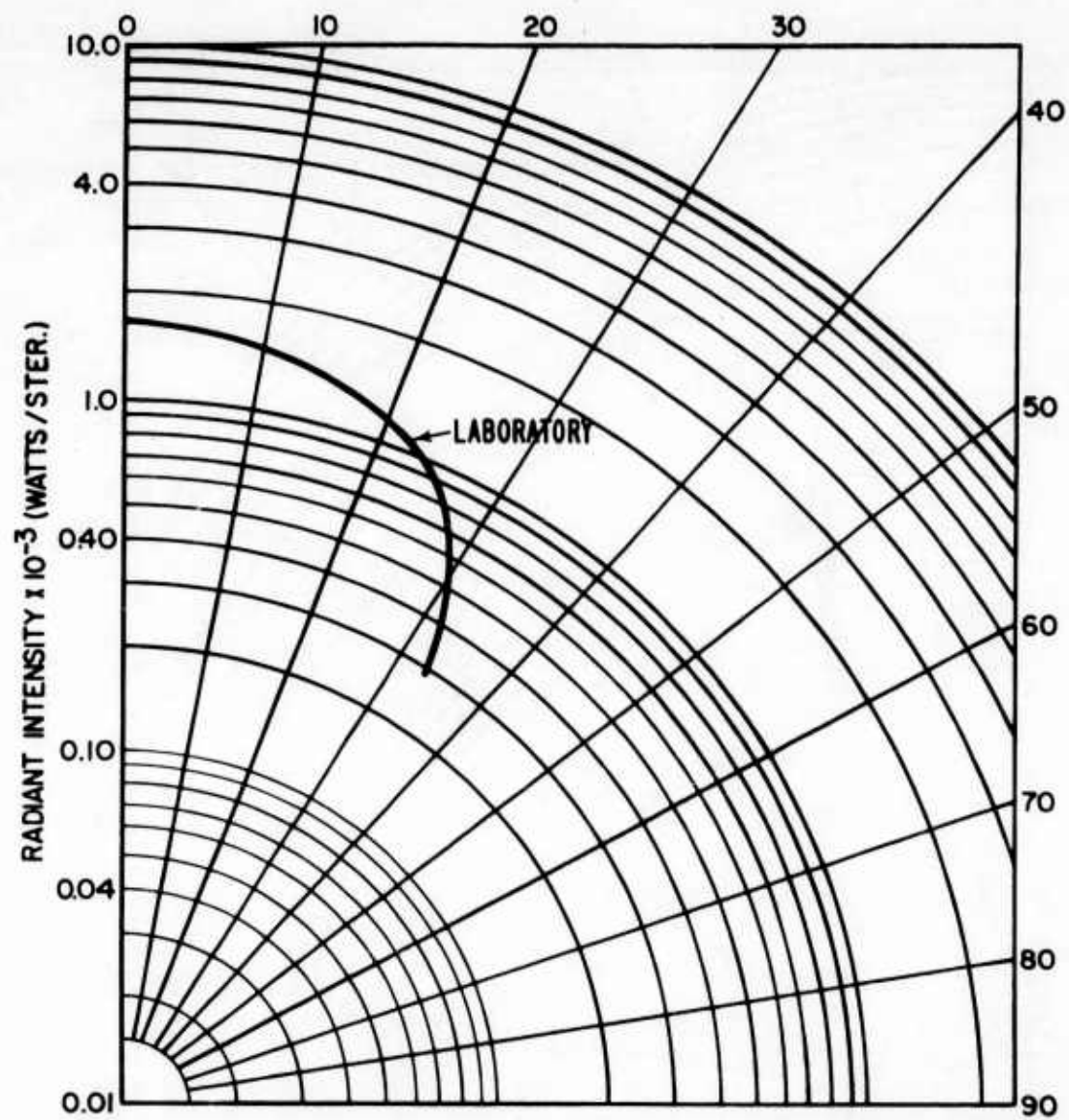


Figure 29. Gold Large Cone, Black Innerbody.

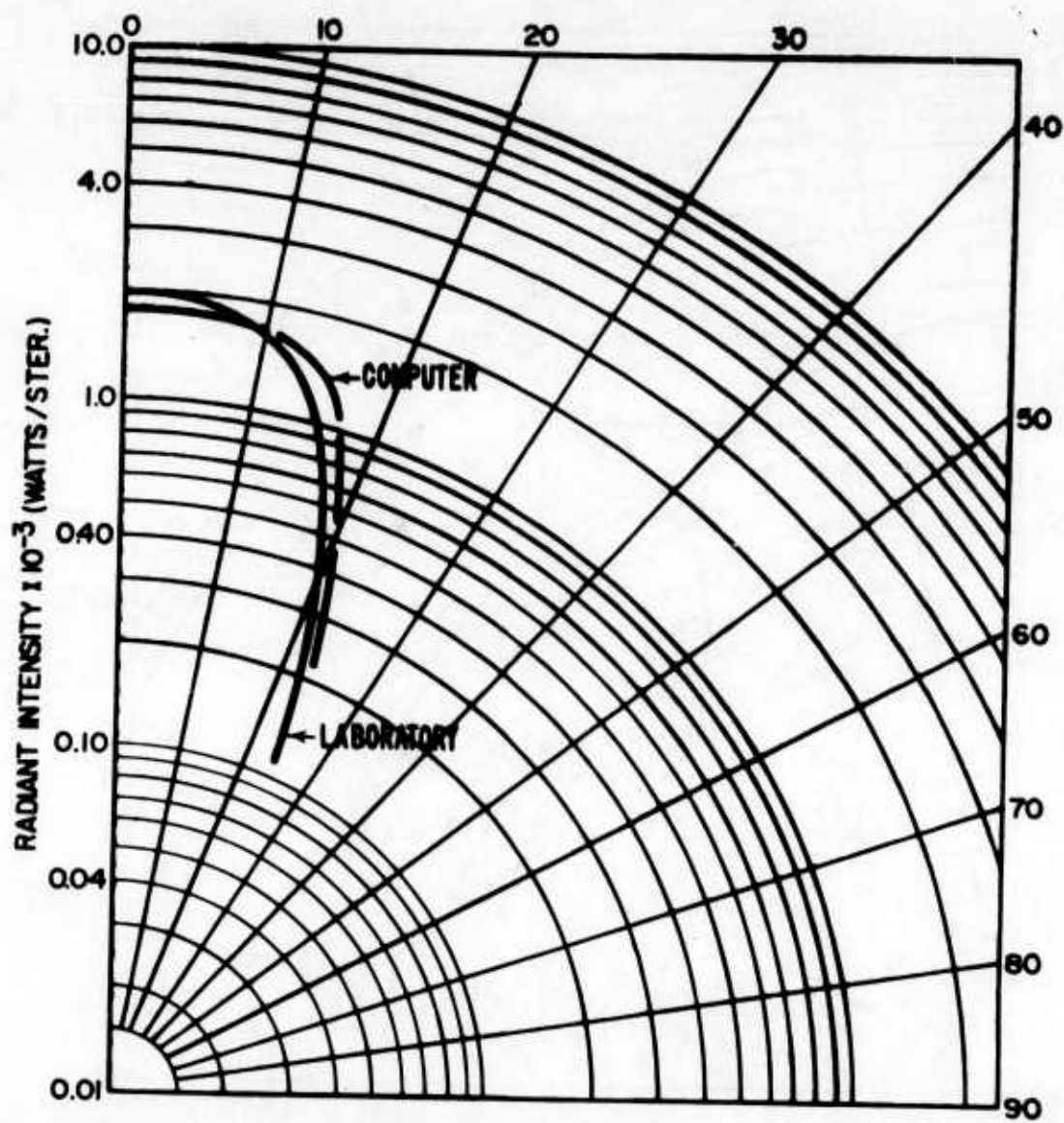


Figure 30. Black Large Cone, No Innerbody.

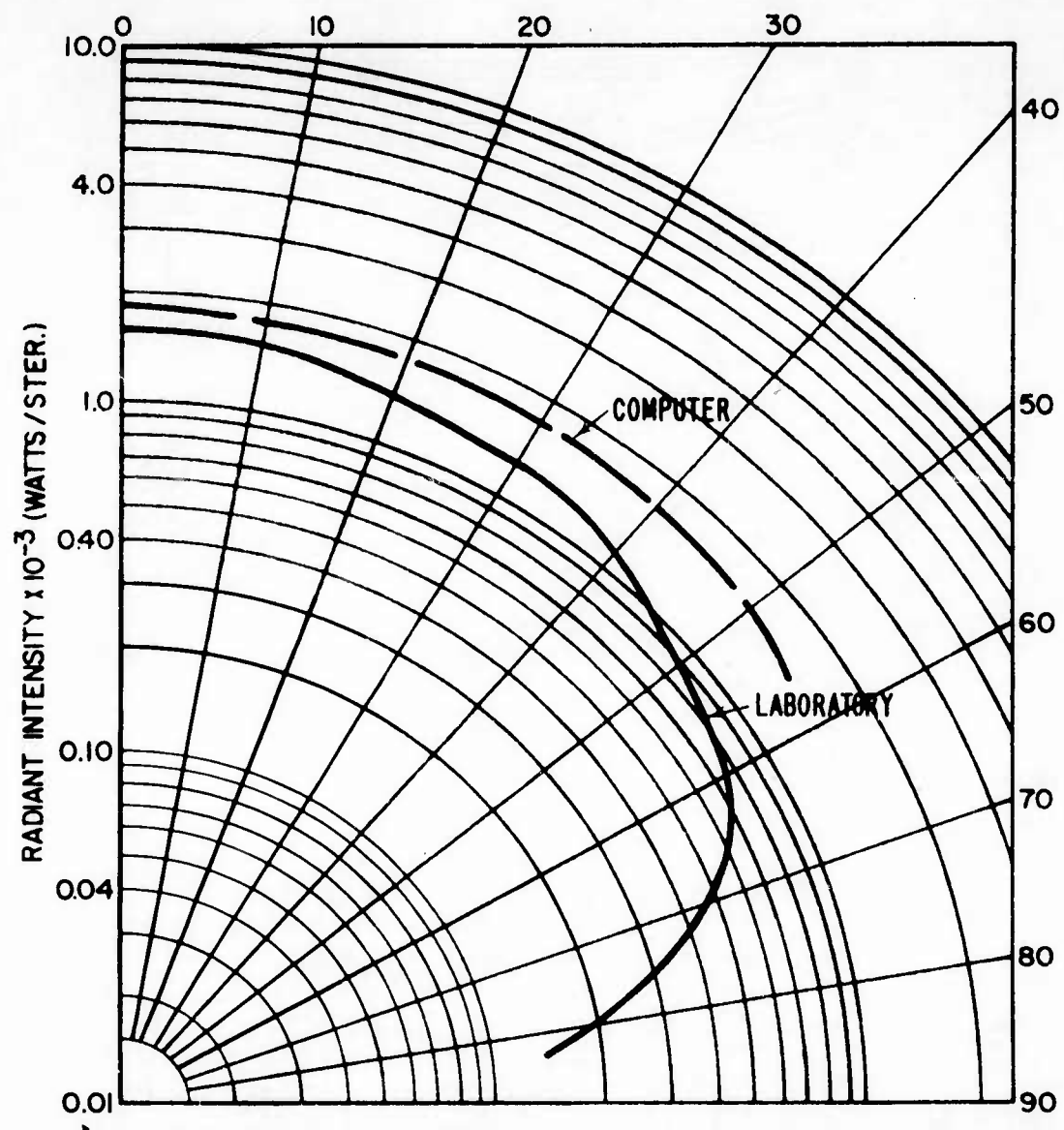


Figure 31. Gold Small Cone, No Innerbody.

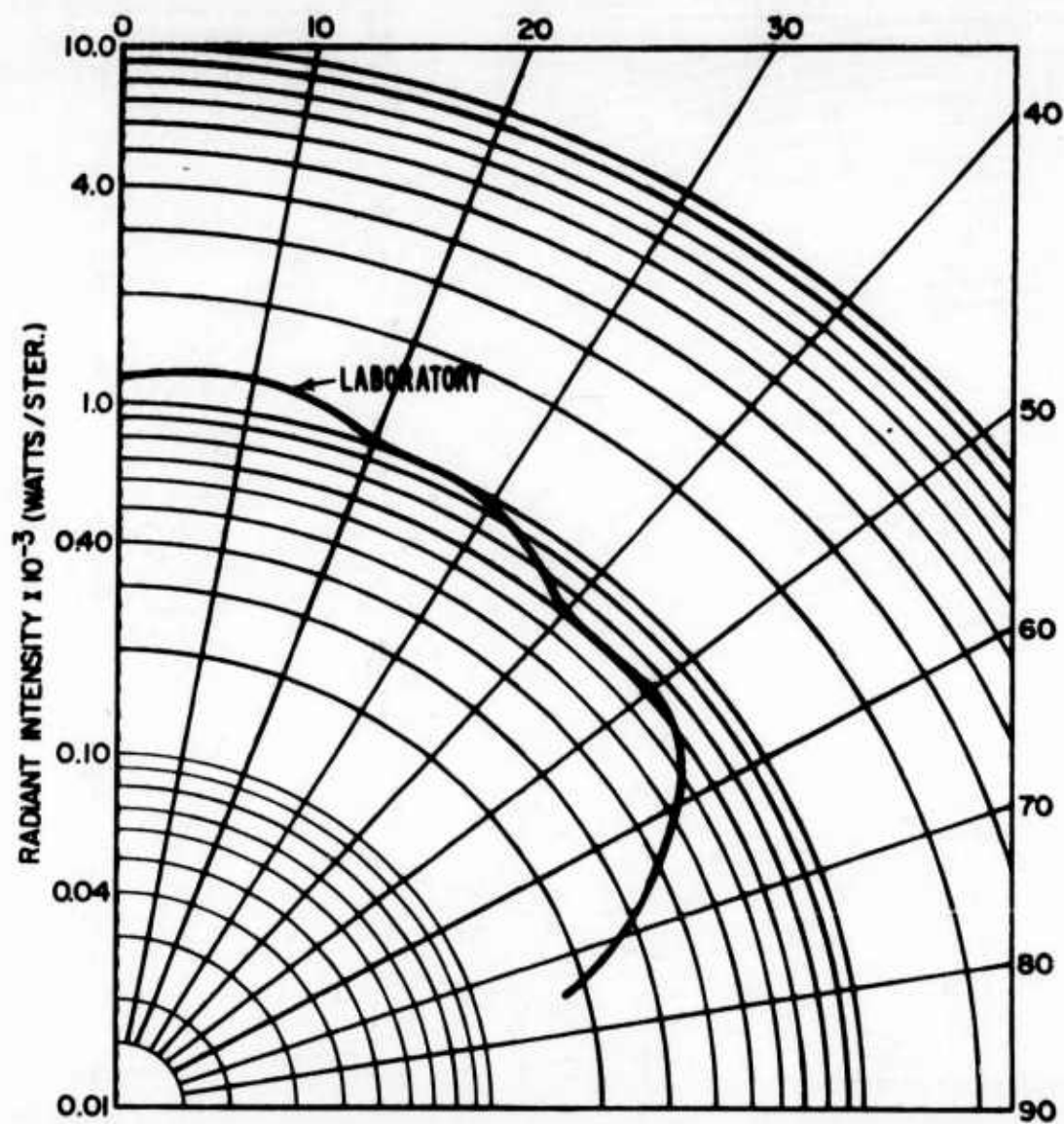


Figure 32. Gold Small Cone, Gold Innerbody.

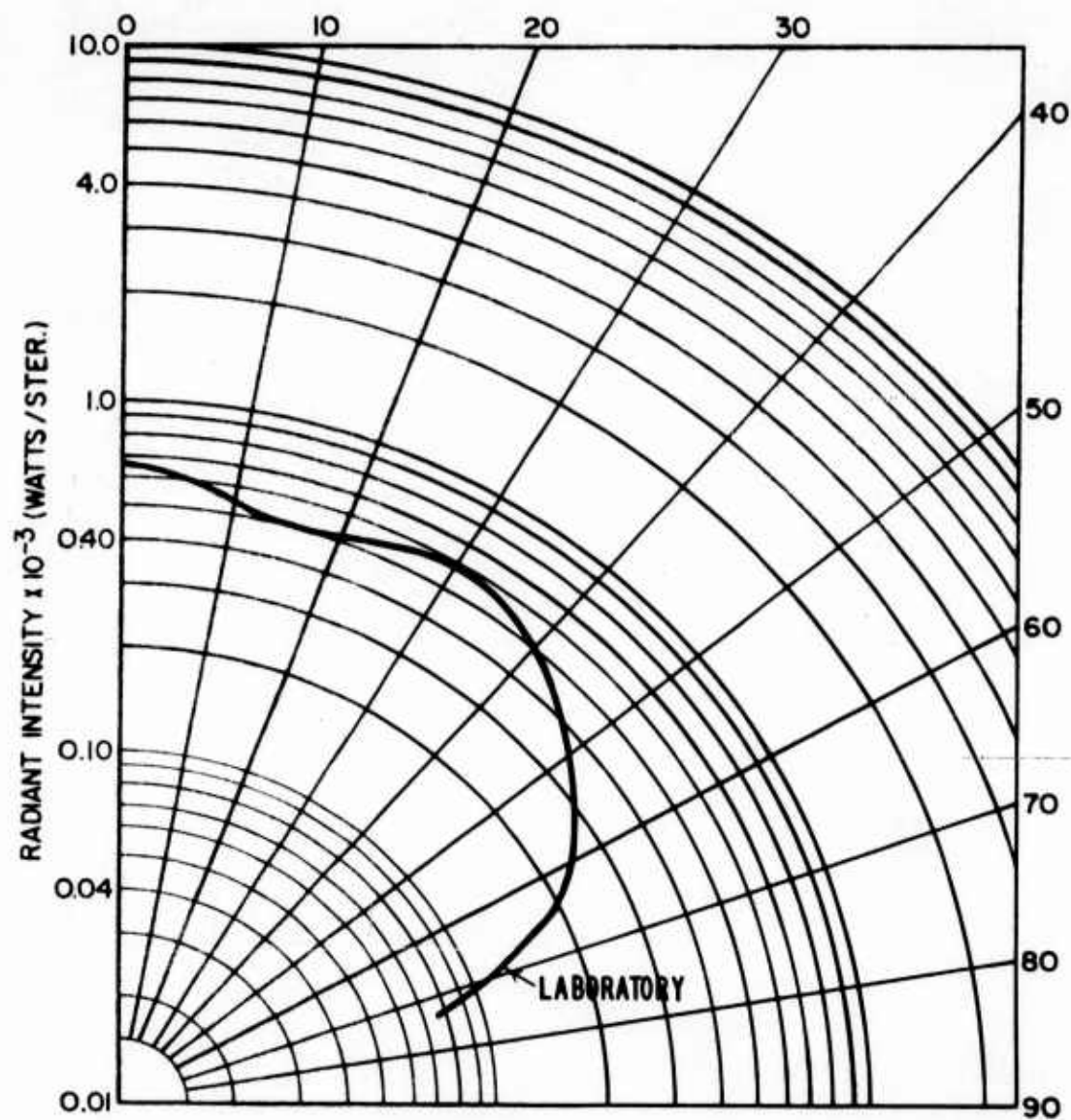


Figure 33. Gold Small Cone, Black Innerbody.

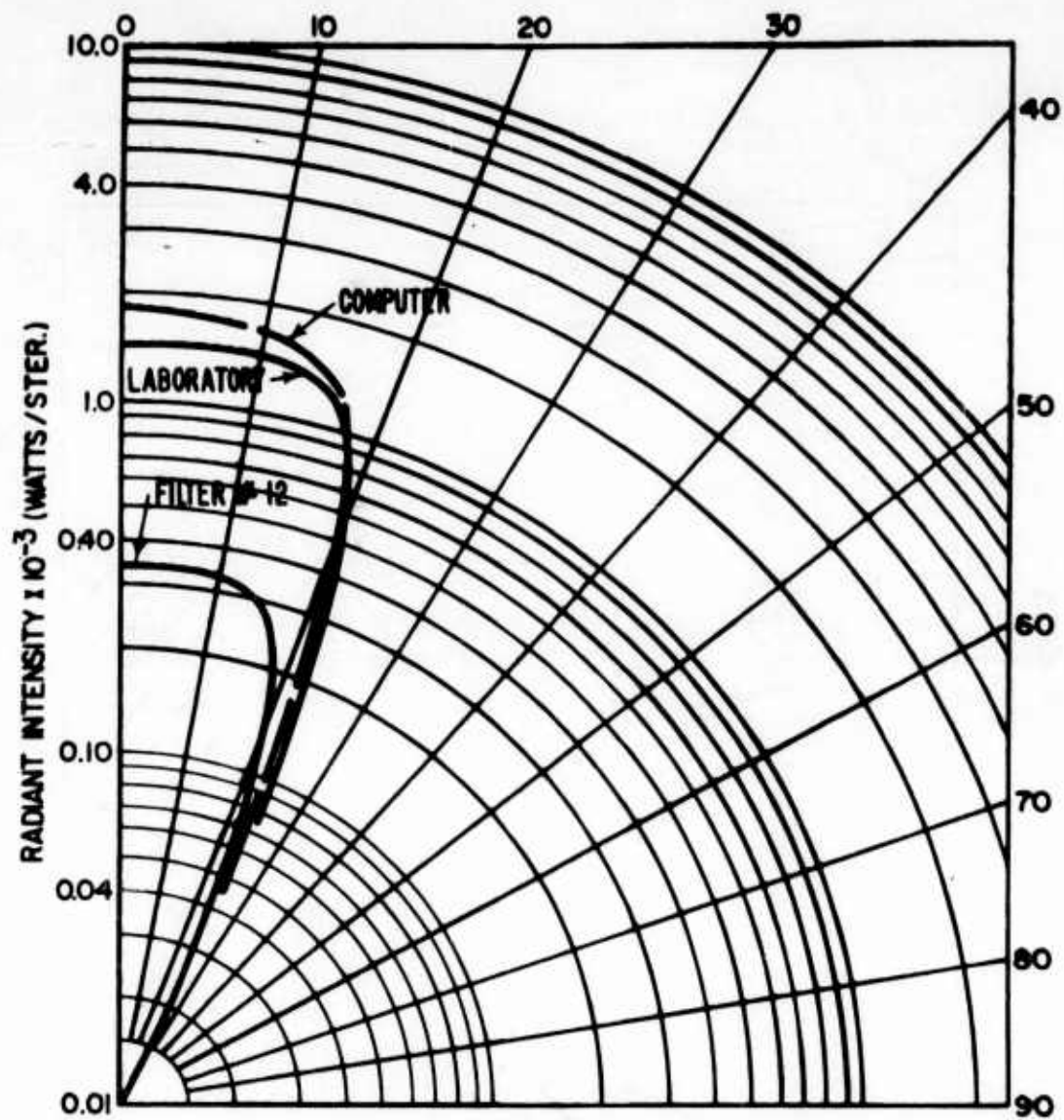


Figure 34. Black Small Cone, No Innerbody.

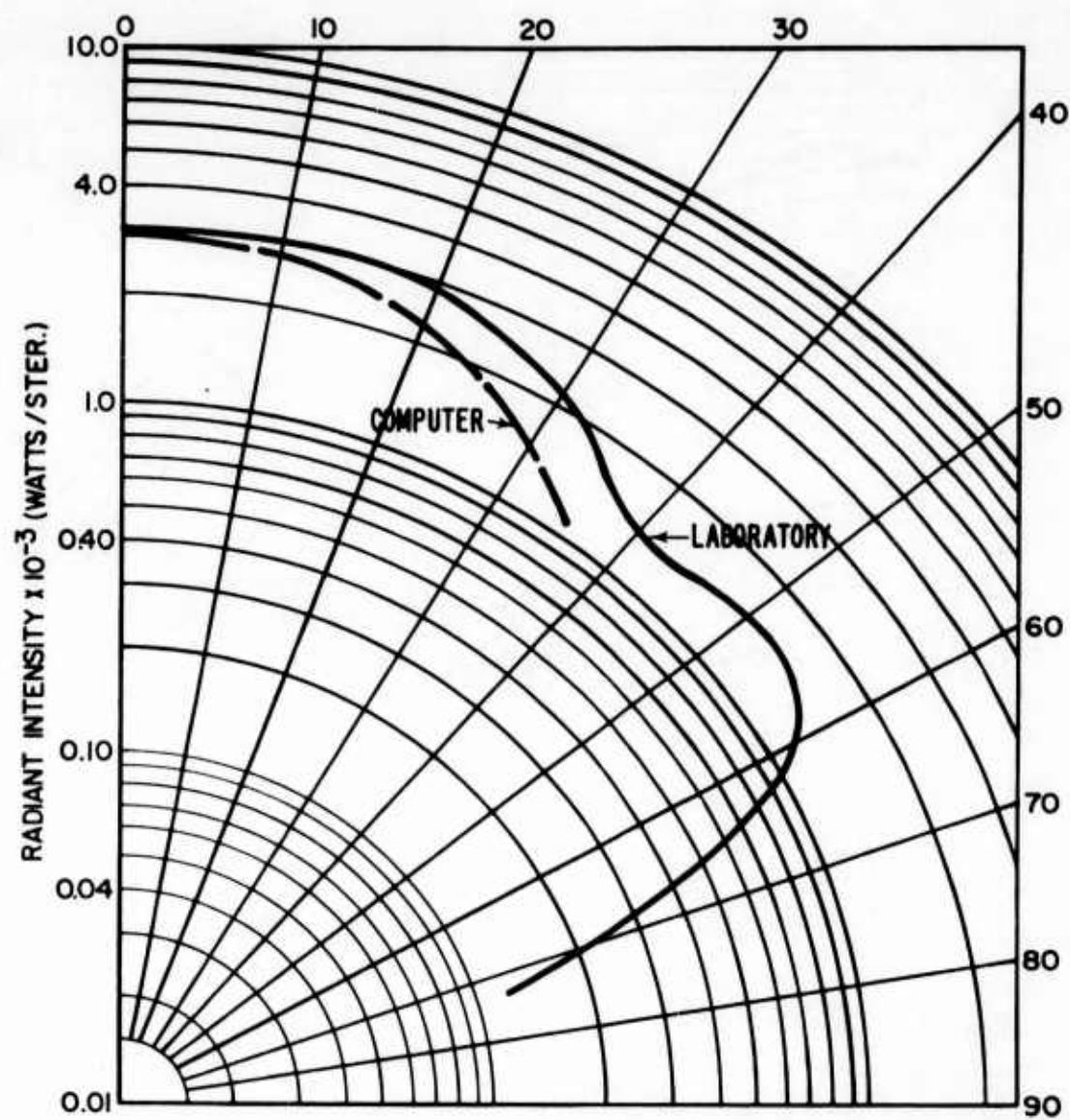


Figure 35. Gold Double Cone, No Innerbody.

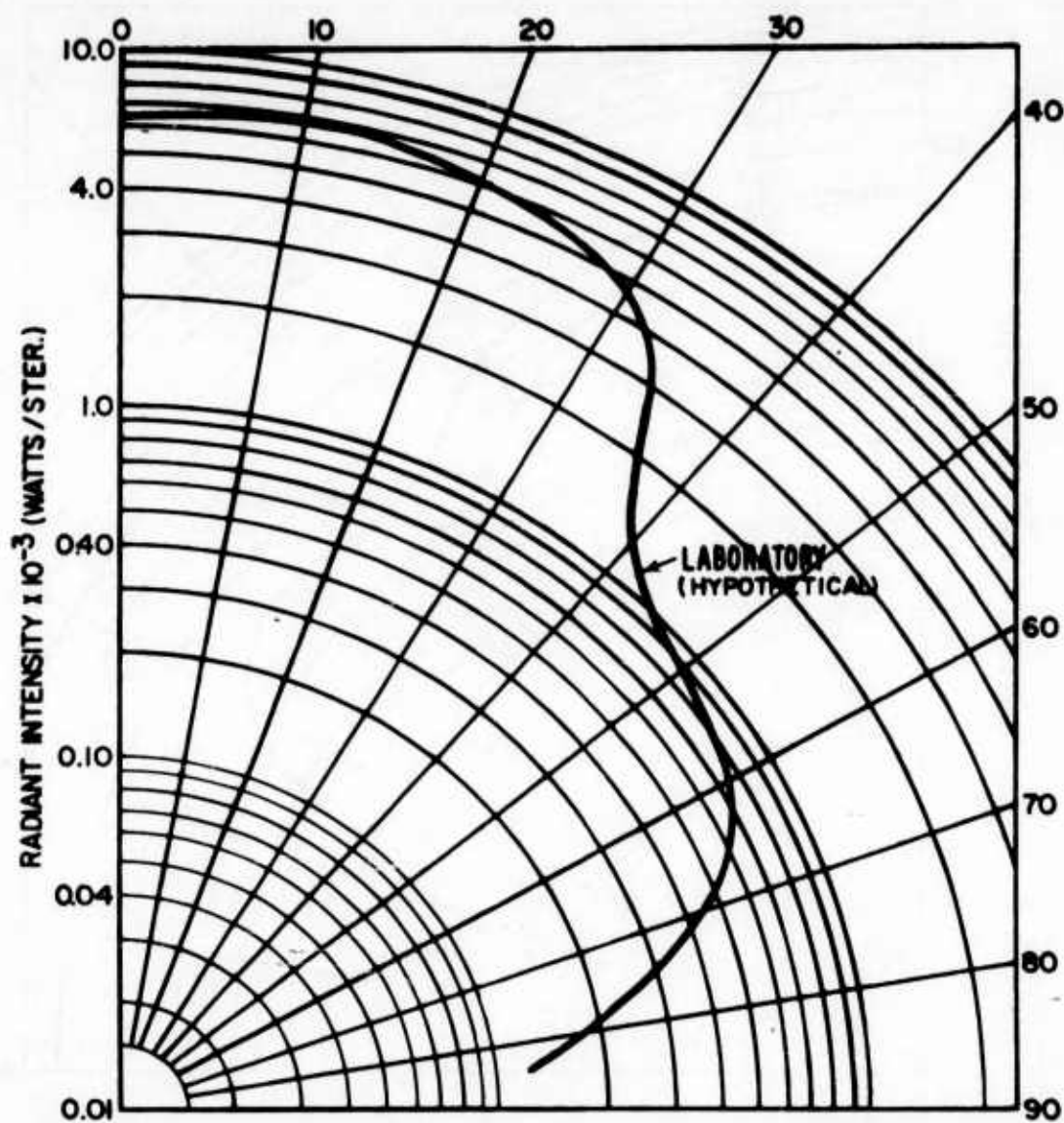


Figure 36. Sum of Large Plus Small Gold Cones.

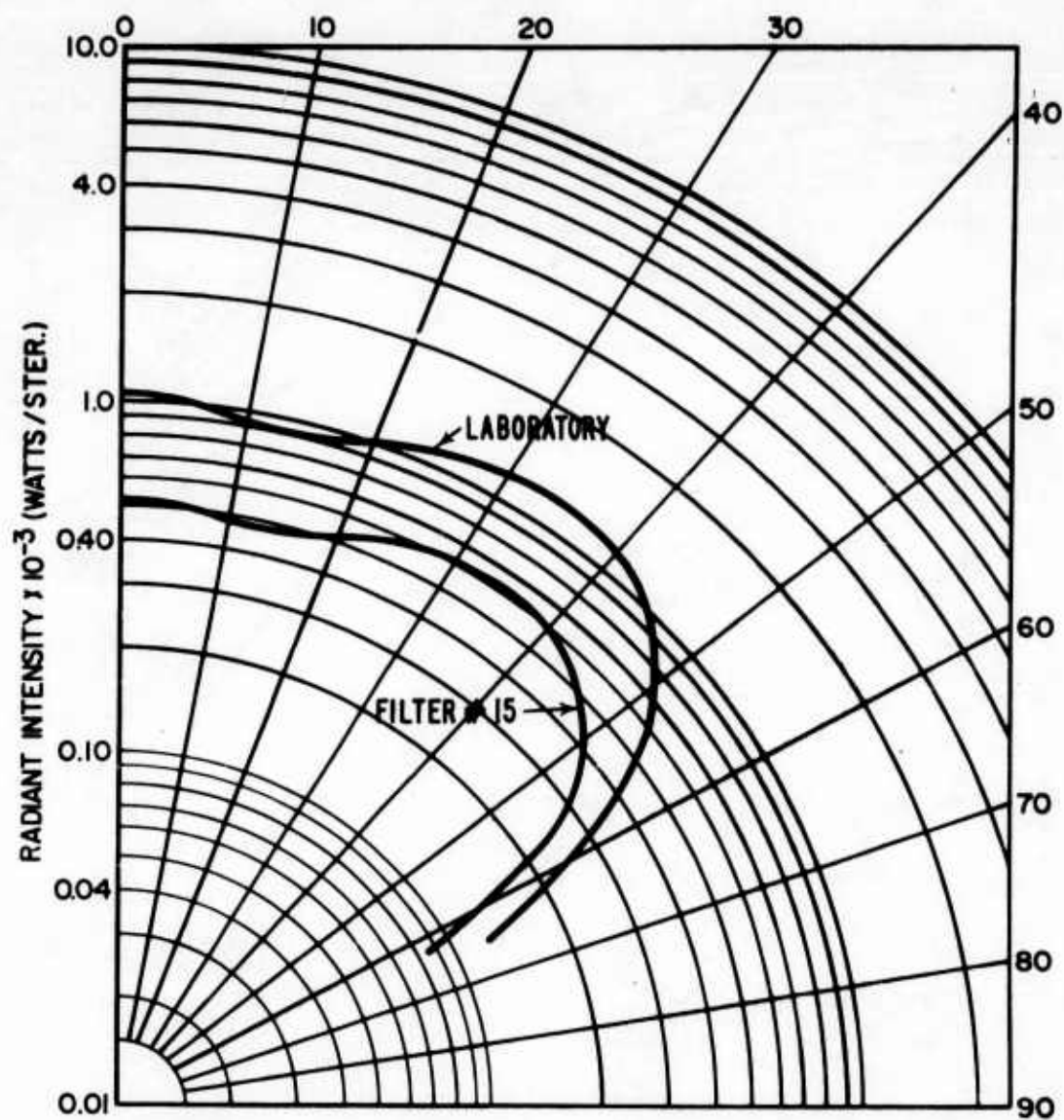


Figure 37. Gold Double Cone, Gold Innerbody.

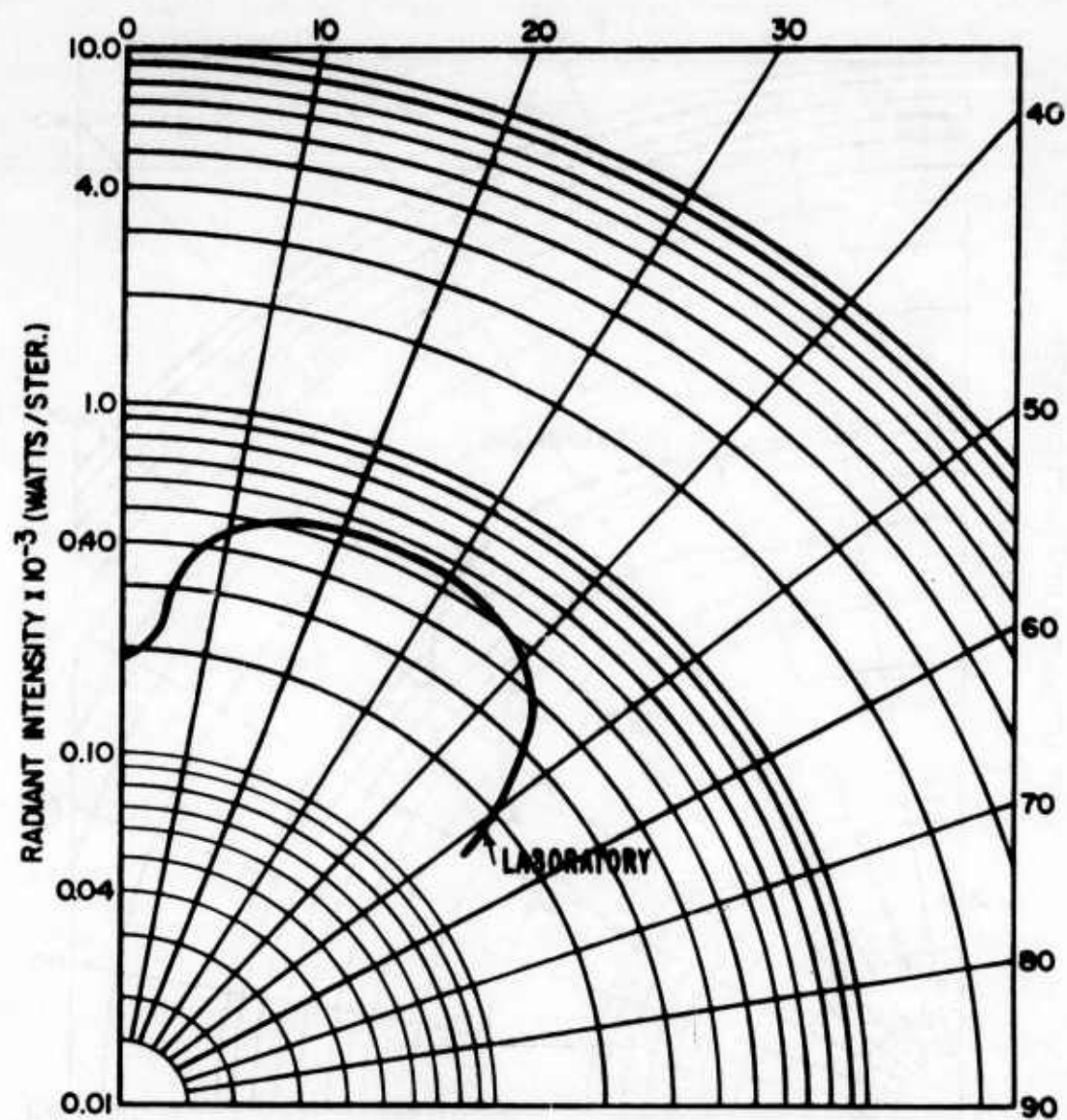


Figure 38. Gold Double Cone, Black Innerbody.

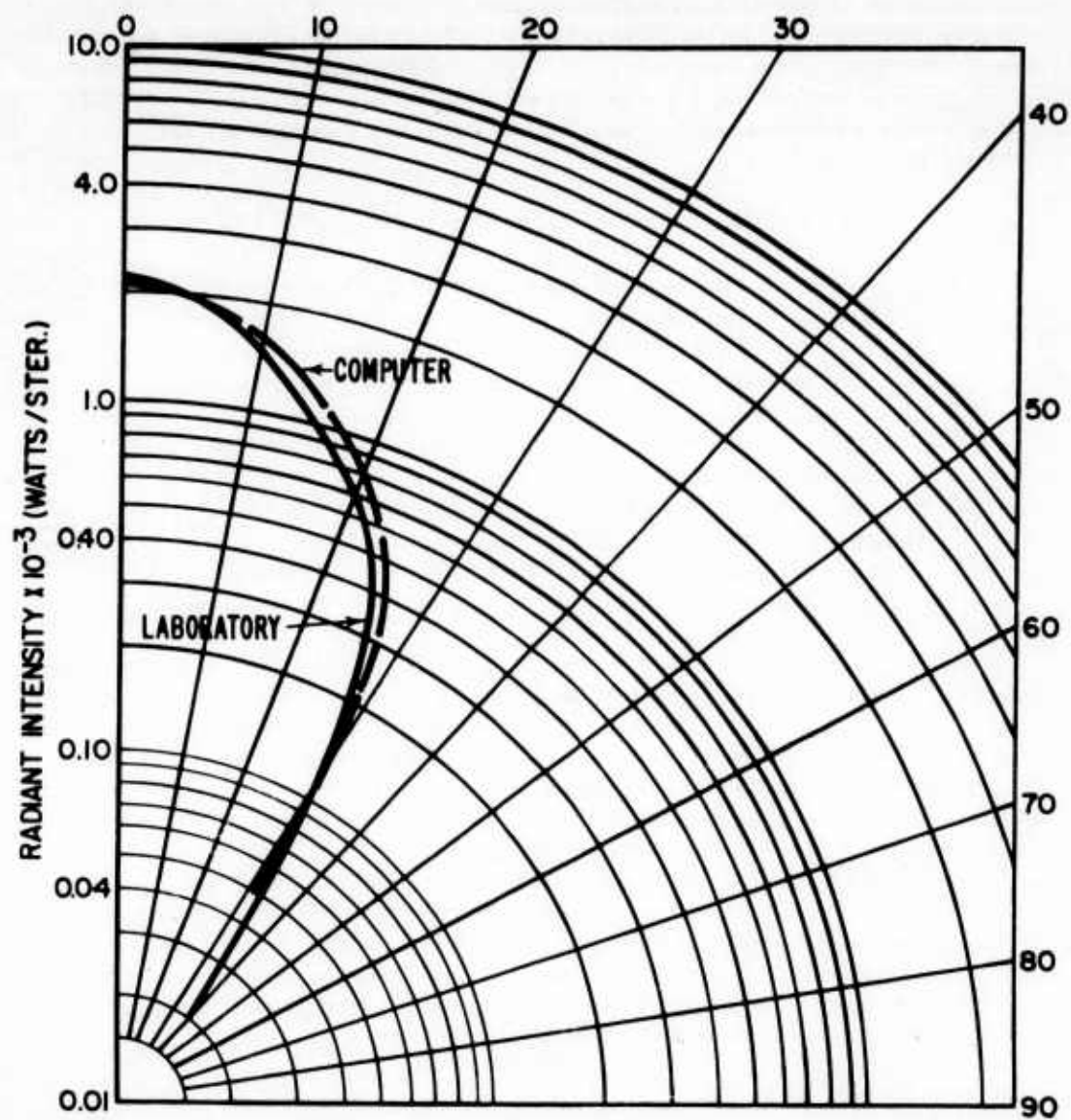


Figure 39. Black Double Cone, No Innerbody.

ANALYSIS OF EXPERIMENTAL ERROR

The experimental error contained in the radiant intensity measurements may be divided generally into two types: random error and determinate error. Qualitatively, random errors are those which vary randomly in sign and magnitude, whereas determinate errors are those which are consistent in sign and more or less consistent in magnitude. The possible sources of error are grouped according to these two classifications below, and the probable error arising from each is estimated.

Random errors are attributable to the following sources:

- (1) Alignment of the radiometer on the black body source and on the target source.
- (2) Changes in radiant intensity of black body or target source because of random temperature variations.
- (3) Electrical noise in the radiometer voltage output.
- (4) Fluctuations in the gain and/or drift of radiometer amplifier and recorder.
- (5) Reading of strip chart records of the radiometer voltage output.
- (6) Reading of filter spectral transmission curves and of curves pertaining to spectral atmospheric transmission.

The probable error due to random sources in a given measured quantity is precisely evaluated from a large number of measurements on that quantity. However, several radiant intensity measurements for each model configuration at each angle were impractical. In order to obtain an estimate of the random error arising from the sources listed above, a statistical analysis was made on a set of 23 radiometer voltage measurements, the voltages being induced by the black body source. The results of the analysis are shown in Table 6. The average voltage V_B for each filter is the result of measurements extending over a six weeks' interval, and, as such, contains an average effect of humidity variations over that time. The probable error P_y represents the combined random error in V_B due to first five sources described above.

It is recognized that the radiative characteristics of a shielded source are probably different from those of the black body source,

TABLE 6
RESULTS OF STATISTICAL ANALYSIS ON RADIOMETER
VOLTAGE CAUSED BY BLACK BODY SOURCE

Filter Number	λ_m (microns)	Mean Deflection V_B	Standard Deviation σ	Probable Error *		Probable Error of Means **	
n				r	%	P_Y	%
1	1.68	2.1	.810	.56	33.0	.12	7.1
2	1.93	9.1	1.057	.73	8.4	.15	1.7
3	2.13	14.7	1.818	1.75	8.9	.26	1.8
4	2.35	18.3	1.378	.95	5.5	.20	1.2
5	2.59	8.5	1.296	.89	11.7	.20	2.6
6	2.72	2.2	.769	.53	24.0	.11	5.0
7	2.94	25.5	2.052	1.42	5.7	.30	1.2
8	3.10	18.8	1.412	.97	5.1	.20	1.1
9	3.36	18.6	2.280	1.57	7.6	.33	1.6
10	3.51	20.2	2.054	1.42	6.6	.30	1.4
11	3.79	19.7	1.564	1.08	5.6	.22	1.1
12	3.92	20.5	1.637	1.13	5.9	.24	1.3
13	4.13	10.0	1.171	.81	8.4	.17	1.8
14	4.26	1.7	.160	.41	22.8	.06	3.3
15	4.47	10.9	1.082	.75	6.9	.16	1.5
16	4.74	6.2	1.021	.70	11.3	.15	2.4
17	5.01	10.1	1.304	.88	8.7	.18	1.8
18	5.16	6.2	.645	.65	9.2	.13	1.8

$$* r = \pm .6745 \sigma$$

$$** P_Y = \pm r / \sqrt{23}$$

but the measurement procedure is the same in either case. To this extent, the assumption is justified that the percentage random error in the target-induced voltage V_T is equal to the percentage random error in the black body-induced voltage V_B . This assumption is made for the purpose of establishing a realistic estimate of the probable random error in the measured spectral radiant intensities. As a specific case, Table 7 presents the estimated probable error in V_T for the gold cylinder model configuration viewed at normal incidence.

A preliminary analysis showed that item (6) above introduced about 5% uncertainty in the filter factors f_J , defined by Eq. (17). Table 7 also shows the associated error in each of the filter factors.

The probable error in a function Z defined by

$$Z = f(X, Y, \dots)$$

is given by the equation

$$P = \pm \left[(P_X \frac{\partial Z}{\partial X})^2 + (P_Y \frac{\partial Z}{\partial Y})^2 + \dots \right]^{\frac{1}{2}} ; \quad (23)$$

therefore, the probable error in the spectral radiant intensity $J(\lambda_m)$, as defined by Eq. (22) is given by

$$P_n = \frac{1}{V_B} \left[(P_X f_J F)^2 + (P_W V_T F)^2 + (P_T V_T f_J)^2 + \left(\frac{R_Y V_T f_J F}{V_B} \right)^2 \right]^{\frac{1}{2}} \quad (24)$$

where V_B , P_Y , V_T , P_X ; and f_J , P_W for the gold cylinder are presented in Tables 6 and 7. The probable error P_T in the field-of-view correction factor ($F = 1.11$) was estimated to be $\pm .01$. For the inputs thus given, the probable error estimated from Eq. (24) is shown for each filter in Table 7.

The probable error in each value of $J(\lambda_m)$ must be propagated through the numerical integration procedure in order to establish the probable error in the total radiant intensity J , which applies to the wavelength interval from λ_{m1} (filter 1) to λ_{m18} (filter 18). J was evaluated by the trapezoidal rule, which has the form

$$J = \frac{1}{2} [J(\lambda_{m1}) + J(\lambda_{m2})] (\lambda_{m2} - \lambda_{m1}) + \dots + \frac{1}{2} [J(\lambda_{m17}) + J(\lambda_{m18})] (\lambda_{m18} - \lambda_{m17}) . \quad (25)$$

TABLE 7
ESTIMATED PROBABLE ERROR IN TARGET
VOLTAGE V_T AND FILTER FACTORS f_J

Filter Number	V_T	Estimated Probable Error	P_x	f_J - factor (watts/ster. -micron)	P_w (watts/ster. -micron)
n		%			
1	2.2	7.1	.2	12.8×10^{-5}	$.6 \times 10^{-5}$
2	14.1	1.7	.2	20.7×10^{-5}	1.0×10^{-5}
3	32.8	1.8	.6	15.3×10^{-5}	$.8 \times 10^{-5}$
4	54.4	1.2	.7	13.8×10^{-5}	$.7 \times 10^{-5}$
5	29.8	2.6	.8	31.6×10^{-5}	1.6×10^{-5}
6	19.7	5.0	1.0	16.2×10^{-5}	$.8 \times 10^{-5}$
7	147.5	1.2	1.8	17.1×10^{-5}	$.9 \times 10^{-5}$
8	124.5	1.1	1.4	14.2×10^{-5}	$.7 \times 10^{-5}$
9	143.2	1.6	2.3	14.0×10^{-5}	$.7 \times 10^{-5}$
10	171.5	1.4	2.4	11.3×10^{-5}	$.6 \times 10^{-5}$
11	186.0	1.1	2.0	10.8×10^{-5}	$.5 \times 10^{-5}$
12	210.5	1.3	2.7	7.9×10^{-5}	$.4 \times 10^{-5}$
13	110.0	1.8	2.0	13.4×10^{-5}	$.7 \times 10^{-5}$
14	16.5	3.3	.5	16.3×10^{-5}	$.8 \times 10^{-5}$
15	139.7	1.5	2.1	16.2×10^{-5}	$.8 \times 10^{-5}$
16	88.0	2.4	2.1	9.7×10^{-5}	$.5 \times 10^{-5}$
17	142.7	1.8	2.6	5.7×10^{-5}	$.3 \times 10^{-5}$
18	92.7	1.8	1.7	6.9×10^{-5}	$.3 \times 10^{-5}$

The probable error in J is given by

$$P_t = \pm \left[a^2 (P_1^2 + P_2^2) + \dots + b^2 (P_{17}^2 + P_{18}^2) \right]^{\frac{1}{2}}, \quad (26)$$

where $a \equiv \frac{1}{2} (\lambda_{m2} - \lambda_{m1}), \dots, b \equiv \frac{1}{2} (\lambda_{m18} - \lambda_{m17})$. For the gold cylinder configuration, P_t has the value $.045 \times 10^{-3}$ watts/ster., which is 1.2 per cent of J:

The following items were taken to be sources of determinate error:

- (1) Numerical approximation of the integrals involved in the f_J factors.
- (2) Numerical approximation of total intensity integral.
- (3) Omission of CO_2 absorption effects in the f_J .
- (4) Approximate nature of the Elsasser model for H_2O absorption bands.
- (5) Background and stray radiation.
- (6) Drag in recorder pen drive.

The magnitude of the error caused by the numerical integrations involved in the f_J factors was minimized by choosing the smallest practical spectral increments; this error was considered negligible. Likewise, the error introduced in the total radiant intensity by numerically integrating over the spectral region 1.68 microns to 5.16 microns was negligible. The principal CO_2 absorption bands within the above spectral region are centered at 2.7 microns and 4.3 microns, corresponding to filters 6 and 14, respectively. The omission of CO_2 absorption contributes to the large percentage error in the spectral radiant intensity at these two filters. However, the integration process so smooths the spectral variations that the resulting error in the total radiant intensity J is relatively small. Hence, the omission of CO_2 absorption over the short path length involved introduces only a slight error in J. The Elsasser model for H_2O absorption is an approximation which is widely used. The error introduced by its use was minimized by the short path length involved in the experiment. Background and stray radiation effects were practically eliminated by the experimental procedure.

The effects of the recorder pen drag were not negligible. It was noted during the experiment that the pen deflection was uncertain to a percentage roughly proportioned to the amount of deflection. This effect was observed for both directions of pen deflection, the

total error being about 4%. Consequently, the voltages V_T and V_B are uncertain to this extent. These uncertainties in V_T and V_B introduce an additional 5.6% error in the spectral radiant intensities.

By combining the percentage random error P_n , presented in Table 8, with the estimated 5.6% determinate error, it is possible to arrive at a realistic estimate of the total error P_t in each of the spectral radiant intensity measurements. Table 8 also presents the estimated total error for the gold cylinder configuration viewed at normal incidence. When the data for P_t in Table 8 are applied in Eq. (26), it is found that the probable error in the total radiant intensity in the wavelength interval 1.68 microns to 5.16 microns is approximately 2.2%. Although these results apply explicitly to the gold cylinder, they serve as estimates of the probable error for the other model configurations.

TABLE 8
ESTIMATED PROBABLE ERROR
IN SPECTRAL RADIANT INTENSITY

Filter Number	m (microns)	$J(\lambda_m)$ (watts/ster.- micron)	Probable Random Error, P_n (watts/ster.- micron)	Total Est. Error, P_t (watts/ster.- micron)	%
n					
1	1.68	2.42×10^{-4}	$.22 \times 10^{-4}$	9.0	$.35 \times 10^{-4}$ 14.6
2	1.93	3.91×10^{-4}	$.21 \times 10^{-4}$	5.3	$.43 \times 10^{-4}$ 10.9
3	2.13	4.24×10^{-4}	$.24 \times 10^{-4}$	5.6	$.47 \times 10^{-4}$ 11.2
4	2.35	5.05×10^{-4}	$.26 \times 10^{-4}$	5.2	$.55 \times 10^{-4}$ 10.8
5	2.59	13.70×10^{-4}	$.88 \times 10^{-4}$	6.4	1.64×10^{-4} 12.0
6	2.72	10.78×10^{-4}	1.36×10^{-4}	12.6	1.97×10^{-4} 18.2
7	2.94	12.35×10^{-4}	$.63 \times 10^{-4}$	5.1	1.33×10^{-4} 10.7
8	3.10	11.18×10^{-4}	$.54 \times 10^{-4}$	4.8	1.15×10^{-4} 10.3
9	3.36	13.33×10^{-4}	$.60 \times 10^{-4}$	4.5	1.34×10^{-4} 10.1
10	3.51	12.23×10^{-4}	$.57 \times 10^{-4}$	4.7	1.29×10^{-4} 10.6
11	3.79	13.03×10^{-4}	$.57 \times 10^{-4}$	4.4	1.30×10^{-4} 10.0
12	3.92	10.25×10^{-4}	$.52 \times 10^{-4}$	4.7	1.05×10^{-4} 10.3
13	4.13	20.07×10^{-4}	1.01×10^{-4}	5.1	2.15×10^{-4} 10.7
14	4.26	16.50×10^{-4}	$.56 \times 10^{-4}$	3.5	1.65×10^{-4} 10.0
15	4.47	26.64×10^{-4}	1.29×10^{-4}	4.8	2.77×10^{-4} 10.4
16	4.74	17.49×10^{-4}	1.01×10^{-4}	14.7	1.20×10^{-4} 11.4
17	5.01	11.03×10^{-4}	$.54 \times 10^{-4}$	4.7	1.16×10^{-4} 10.5
18	5.16	13.07×10^{-4}	$.50 \times 10^{-4}$	3.8	1.23×10^{-4} 9.5

ANALYSIS OF COMPUTER PROGRAMS

INTRODUCTION

This project has been conceived as having a dual purpose: (1) the laboratory measurement of certain model configurations having simple, carefully maintained boundary conditions, with the aim of determining the radiant intensity distribution as a function of the azimuthal angle and expressing the radiant intensity in a suitable system of units, as opposed to normalized curves; and (2) the derivation of a theoretical or empirical formulation for the prediction of the radiant intensity as a function of the azimuthal angle for complex, shielded, radiating sources. The first part of this dual purpose has been described in detail in the preceding sections of this report. A similar description of the second part will now be given.

During the course of this project, this formulation has generally been referred to as the theoretical analysis, in contrast with the experimental program. Properly, it should be called the empirical formulation, since no attempt is made to base the technique on the theory of infrared radiation and reflection. This yet remains to be done. The attempt here has been to establish an empirical technique for predicting radiative characteristics of shielded infrared sources without having to resort to actual fabrication and laboratory measurement. The approach followed in the formulation of this technique was to select randomly a ray and to trace it through the configuration geometrically. This approach could be followed in either of two directions; i. e., the random choice of a ray could be either in the source plate with the tracing outwardly directed or in the aperture of the configuration with the tracing inwardly directed. The latter choice was elected because it was felt that it would yield the desired results with a minimum of computations. Since the laboratory measurements, which were to serve as a check on the empirical formulation, were made in the horizontal diametral plane of the models, only those rays radiating into this plane, or planes parallel to it, were of interest. However, a ray chosen at the source plate might radiate into any plane and at any angle with respect to the axis of symmetry (also the optical axis of the radiometer). To obtain a sufficient number

of rays having a given angular orientation and lying in horizontal planes, it might be necessary to trace many times as many rays. If a ray were chosen in the aperture with the desired angular orientation and lying in a horizontal plane, it could be traced without fear of unnecessary computations. The process could be repeated until the necessary number of rays had been traced. The description of this process can be conveniently divided into two topics: (1) the random selection of a ray and (2) the geometrical tracing of the ray.

MONTE CARLO TECHNIQUES

The random selection of a point in the aperture through which a ray might pass and the integration over the contributions of all such rays involve certain statistical methods known as Monte Carlo techniques. The following discussion will show how these techniques are employed and what approximations must be made.

In order to determine the radiant intensity J at some particular angle ϕ relative to the axis of symmetry, one must solve the equation

$$J = 2 \int_0^R \int_0^\pi N r \, dr \, d\theta, \quad (27)$$

where R is the radius of the aperture and N is the radiance of a pencil of rays emerging from an element of area $r \, dr \, d\theta$ in the aperture determined by randomly selecting values of r and θ . The factor 2 occurs because the limits of integration over $d\theta$ are taken from 0 to π rather than from 0 to 2π . This procedure effectively doubles the number of rays considered. In order to select the random values of r and θ , a distribution function must be established which meets certain boundary conditions. We take the distribution function to be $f(r, \theta) = k r$ where k is a yet undetermined constant. Then

$$\int_0^R \int_0^\pi k r \, dr \, d\theta = 1.$$

On integrating,

$$\frac{k R^2}{2} \pi = 1 \text{ or } k = \frac{2}{\pi R^2}.$$

Now,

$$f(r, \theta) = \frac{2r}{\pi R^2} = f_1(r) f_2(\theta),$$

where

$$f_1(r) = \frac{2r}{R^2} \quad \text{and} \quad f_2(\theta) = \frac{1}{\pi}.$$

The random values of r and θ can be chosen from lists of uniformly random numbers by integrating over $f_1(r)$ and $f_2(\theta)$. If U and V are the lists of random numbers,

$$U = \int_0^r \frac{2r}{R^2} dr = \frac{r^2}{R^2}, \quad V = \int_0^\theta \frac{1}{\pi} d\theta = \frac{\theta}{\pi},$$

and

$$r = R \sqrt{U}, \quad \theta = \pi V.$$

The expected value of N is by definition

$$\begin{aligned} E(N) &= \int_0^R \int_0^\pi N \frac{2}{\pi R^2} r dr d\theta \\ &= \frac{2}{\pi R^2} \int_0^R \int_0^\pi N r dr d\theta. \end{aligned}$$

Substituting from Eq. (27) yields

$$E(N) = \frac{1}{\pi R^2} J,$$

or

$$J = \pi R^2 E(N). \quad (28)$$

Now, the expected value of N can be approximated by an averaging process, so that

$$E(N) = \frac{1}{n} \sum_{i=1}^n N_i.$$

Substituting the summation for $E(N)$ in Eq. (28) yields for the radiant intensity J this expression:

$$J = \frac{\pi R^2}{n} \sum_{i=1}^n N_i. \quad (29)$$

RAY-TRACING TECHNIQUES

Once a ray has been chosen randomly, N can be determined by tracing it analytically through the configuration to the source plate. The following discussion outlines this process for the simple case of the water-cooled cylinder without any innerbody.

Consider a cylinder of radius r and length z_0 . A ray L_1 emerges from a random position (x_0, y_0, z_0) at any specified angle ϕ . (See Figure 40.) The random position is specified by an angle θ and a radius R_0 . The angle θ is one of 200 angles obtained by multiplying 2π by 200 random numbers between zero and one. R_0 is one of 200 radii obtained by multiplying r by another set of 200 random numbers between zero and one. The coordinates of point (x_0, y_0, z_0) are given by

$$x_0 = R_0 \sin \theta$$

$$y_0 = R_0 \cos \theta$$

$$z_0 = z_0.$$

Since L_1 lies in a plane parallel to the yz plane, its direction cosines are 0, $\cos(90 - \phi)$, and $\cos \phi$. Therefore, a set of parametric equations for L_1 is given by

$$x = x_0$$

$$y = y_0 + t \cos(90 - \phi) \quad (30)$$

$$z = z_0 + t \cos \phi.$$

To determine whether L_1 is reflected by the cavity shield or is a direct ray from the base, a test is performed to indicate whether L_1 intersects the xy plane inside or outside the cylinder.

Let the point of intersection of L_1 in the xy plane be designated by $(x^{b1}, y^{b1}, 0)$. From Eq. (30),

$$z_0 + t \cos \phi = 0$$

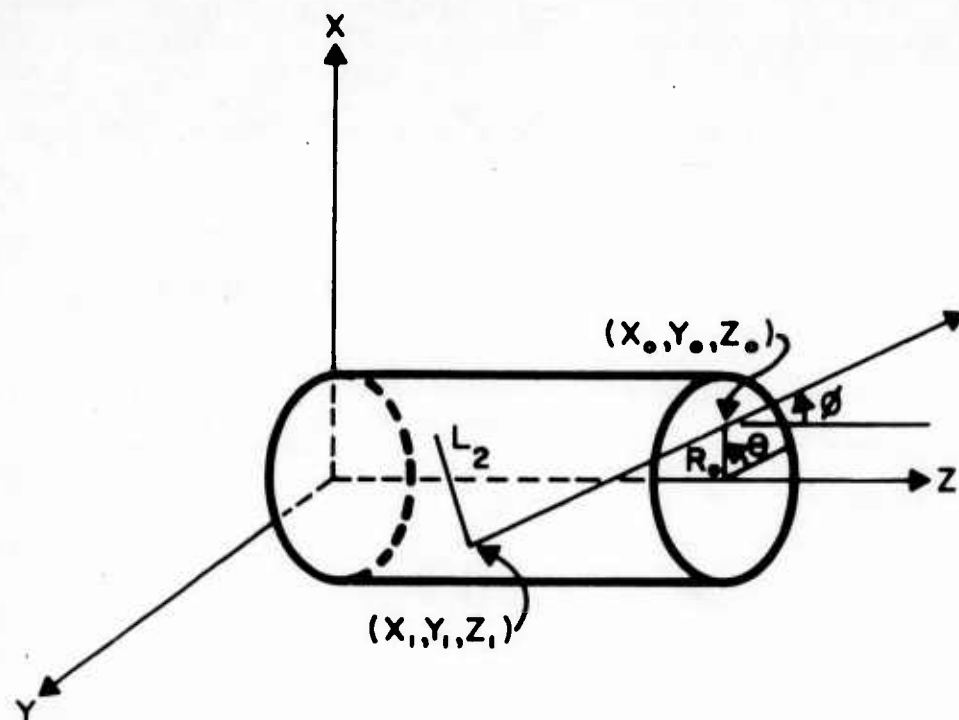


Figure 40. Cylinder with Emergent Ray L_1 and Reflected Ray L_2 .

so that

$$t = - \frac{z_0}{\cos \phi}$$

and

$$y^{b_1} = y_0 - \frac{z_0}{\cos \phi} \cos (90 - \phi)$$

$$x^{b_1} = x_0 .$$

Let r^{b_1} be the distance from $(x^{b_1}, y^{b_1}, 0)$ to the origin. Then

$$r^{b_1} = \sqrt{x^{b_1^2} + y^{b_1^2}} .$$

If $r^{b_1} \leq r$, the ray is a direct ray and the radiance N is given by

$$N = N_0 \cos \phi$$

where N_0 is the radiance normal to the base. If $r^{b_1} > r$, the ray is reflected from the cylinder at some point (x_1, y_1, z_1) , where, from Eq. (30),

$$x_1 = x_0$$

$$y_1 = y_0 + t \cos (90 - \phi)$$

$$z_1 = z_0 + t \cos \phi .$$

In order to determine the direction of the reflected ray L_2 , a normal n to the surface at the intersection of L_1 and the cylinder must be erected, as well as a line p perpendicular to L_1 and n . (See Figure 41.) The reflected ray L_2 must lie in the plane of L_1 and n , and angle A_2 must equal angle A_1 . Direction cosines of L_1 are 0, $\cos (90 - \phi)$, $\cos \phi$. Direction cosines of n are x_1/r , y_1/r , 0. Direction numbers of p are 1, a_1 , b_1 . L_2 has direction cosines k_1 , l_1 , m_1 . Consequently,

$$\cos A_1 = \frac{y_1}{r} \cos (90 - \phi) \text{ and}$$

$$\cos A_2 = |\cos A_1| .$$

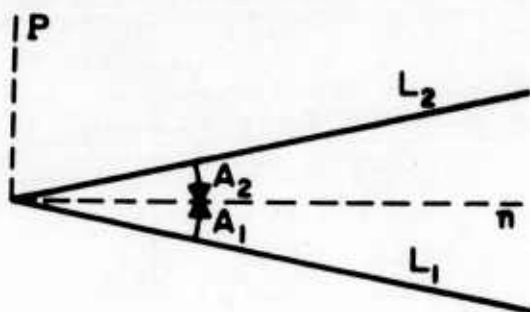


Figure 41. Geometry for Determining Reflected Ray

The last equation may be rewritten as

$$k_1 \frac{x_1}{r} + l_1 \frac{y_1}{r} = \frac{|y_1|}{r} \cos(90 - \phi), \text{ or}$$

$$k_1 + l_1 \frac{y_1}{x_1} - \frac{y_1}{x_1} \cos(90 - \phi) = 0. \quad (31)$$

Equation (31) and four other relations lead to solutions for the direction cosines of L_2 . These five equations are

$$k_1 + l_1 \frac{y_1}{x_1} - \frac{y_1}{x_1} \cos(90 - \phi) = 0 \quad (\angle A_2 = \angle A_1) \quad (32a)$$

$$k_1 l + l_1 a_1 + m_1 b_1 = 0 \quad (L_2 \perp p) \quad (32b)$$

$$l \frac{x_1}{r} + a_1 \frac{y_1}{r} = 0 \quad (p \perp n) \quad (32c)$$

$$l(0) + a_1 \cos(90 - \phi) + b_1 \cos \phi = 0 \quad (p \perp L_1) \quad (32d)$$

$$k_1^2 + l_1^2 + m_1^2 = 1. \quad (32e)$$

Rearranging (32c) gives

$$a_1 = -\frac{x_1}{y_1},$$

and solving (32d) for b_1 gives

$$b_1 = \frac{x_1 \cos(90 - \phi)}{y_1 \cos \phi}.$$

Equations (32a), (32b), and (32c) can be solved simultaneously for k_1 , l_1 , and m_1 in terms of a_1 and b_1 , yielding

$$k_1 = \frac{a_1^2 |y_1| \cos(90 - \phi)}{x_1 (1 + a_1^2)} - \frac{b_1}{1 + a_1^2} \sqrt{\frac{1 + a_1^2 - a_1^2 \left(\frac{|y_1|}{x_1}\right)^2 \cos^2(90 - \phi)}{1 + a_1^2 + b_1^2}}$$

$$l_1 = -\frac{a_1 b_1}{1 + a_1^2} \sqrt{\frac{1 + a_1^2 - a_1^2 \left(\frac{|y_1|}{x_1}\right)^2 \cos^2(90 - \phi)}{1 + a_1^2 + b_1^2}} - \frac{a_1 |y_1| \cos(90 - \phi)}{x_1 (1 + a_1^2)}$$

$$m_1 = \pm \sqrt{\frac{1 + a_1^2 - a_1^2 \left(\frac{|y_1|}{x_1}\right)^2 \cos^2(90 - \phi)}{1 + a_1^2 + b_1^2}}.$$

The signs are chosen so that the reflected ray lies within the cylinder. The parametric equations of the reflected ray are

$$x = x_1 + k_1 t$$

$$y = y_1 + l_1 t$$

$$z = z_1 + m_1 t.$$

The radiance N of the reflected ray is given by

$$N = N_0 R^n |\cos \phi|, \quad (33)$$

where N_0 is the radiance normal to the plate, R is the surface reflectivity of the cylindrical shield, and n is the number of reflections experienced by the ray. Equation (33) for the i -th ray is substituted in Eq. (29) to compute the radiant intensity.

In the case of a configuration having an innerbody, provisions must be made for reflection at the surface of the innerbody. As a simple example, consider the case of the cylinder with a spherical, water-cooled innerbody. As before, L_1 is a randomly positioned ray

emerging from the model at some particular angle ϕ relative to the axis of the model. Let the point from which the ray emerges be (x_0, y_0, z_0) and let the radii of the cylinder and inner sphere be r_1 and r_3 , respectively. When traced back into the cavity, L_1 may initially intersect the sphere, the cylinder, or the source plate.

If L_1 intersects the source plate, the radiance may be calculated immediately. If L_1 intersects the cylinder and does not thereafter intersect the sphere, the treatment is the same as that given in the discussion above. Three cases remain: (1) L_1 may intersect the sphere and be reflected back out; (2) L_1 may intersect the sphere and be reflected into the cavity, striking either the cylinder or the source plate; (3) L_1 may intersect the cylinder and be reflected onto the sphere.

In case (1), the ray is discarded. For case (2), the parametric equations of L_1 are

$$\left. \begin{aligned} x &= x_0 + k_1 t_1 \\ y &= y_0 + l_1 t_1 \\ z &= z_0 + m_1 t_1 \end{aligned} \right\} ,$$

in which

$$k_1 = 0$$

$$l_1 = \cos(90 - \phi)$$

$$m_1 = \cos \phi ,$$

and the equation of the sphere is

$$x^2 + y^2 + (z-K)^2 = r_3^2 , \quad (35)$$

where K is the distance from the center of the sphere to the origin. Solving Eqs. (34) and (35) for t_1 yields

$$t_1 = \frac{-B + \sqrt{B^2 - 4AC}}{2A} ,$$

where

$$A = k_1^2 + l_1^2 + m_1^2$$

$$B = 2[x_0 k_1 + y_0 l_1 + (z_0 - K) m_1]$$

$$C = x_0^2 + y_0^2 + (z_0 - K)^2 - r_3^2$$

If $B^2 - 4AC$ is negative, L_1 does not intersect the sphere. If $B^2 - 4AC$ is positive, solve for the t which makes $m_1 t$ negative. The point of intersection (x_1, y_1, z_1) can now be determined.

To determine the equations of the reflected ray L_2 , it is necessary to erect a normal n to the surface of the sphere at (x_1, y_1, z_1) and a line P perpendicular to L_1 and n . Direction numbers of the normal are

$$\frac{\partial f}{\partial x} = 2x$$

$$\frac{\partial f}{\partial y} = 2y$$

$$\frac{\partial f}{\partial z} = 2(z - K)$$

or, just as well,

$$\frac{x_1}{r_3}, \frac{y_1}{r_3}, \frac{z_1 - K}{r_3}$$

Direction numbers of P are $(1, a_1, b_1)$, and direction cosines of L_2 are (k_2, l_2, m_2) . As in the discussion of the cylinder, five simultaneous equations can be set up to determine the equations of L_2 . These equations are

$$x_1 + a_1 y_1 + b_1 (z_1 - K) = 0 \quad (P \perp n) \quad (36a)$$

$$k_1 + a_1 (l_1) + b_1 m_1 = 0 \quad (P \perp L_1) \quad (36b)$$

$$k_2 + l_2 a_1 + m_2 b_1 = 0 \quad (P \perp L_2) \quad (36c)$$

$$\cos(N, L_2) = |\cos(N, L_1)| \quad (\angle(N, L_2) = \angle(N, L_1)) \quad (36d)$$

$$k_2^2 + l_2^2 + m_2^2 = 1. \quad (36e)$$

Equations (36a) and (36b) can be solved for a_1 and b_1 , and Eqs. (36c), (36d), and (36e) can be solved for k_2 , l_2 , and m_2 . The equations of L_2 are then

$$x = x_1 + k_2 t_2$$

$$y = y_1 + l_2 t_2$$

$$z = z_1 + m_2 t_2 .$$

This reflected ray is tested for intersection with the cylinder and the source plate. If no intersection occurs, the ray has been reflected outside and the case degenerates to case (1). If an intersection occurs, the analysis is repeated until the ray intersects the source plate.

The analysis for case (3) is the same as that for case (2), except the emergent ray L_1 strikes the cylinder first. The radiance of those rays which eventually intersect the source plate is given by

$$N = N_0 R_1^{n_1} R_2^{n_2} |\cos \psi| , \quad (37)$$

where N_0 is the radiance normal to the source plate, R_1 and R_2 are the reflectivities of the cylinder and sphere, n_1 and n_2 are the number of times the respective surfaces reflect the ray, and ψ is the angle at which the ray intersects the source plate.

Obviously, the large number of computations involved demands the use of a high-speed, electronic computer. The discussions here were the basis of programs written initially for a Royal-McBee RPC 4000 computer. Similar programs were written for all the other configurations studied. Largely because of the limited memory, its attendant limitations on lengthy programs, and lack of rapid input-output, the RPC 4000 was exchanged about midway through the project for an IBM 1620.

RESULTS

These computer programs were actually run for eleven of the twenty configurations studied. The results have been tabulated in Table 9, where the letter E followed by a negative number refers

TABLE 9
RESULTS OF EMPIRICAL COMPUTER PROGRAMS

Configuration	Radiant Intensity (watts/ster.)	Angle in Degrees
Gold Cylinder	.3818E-2	0
	.3707E-2	10
	.3489E-2	20
	.3159E-2	30
	.2742E-2	40
	.2239E-2	50
	.1671E-2	60
	.1058E-2	70
Gold Cylinder With Gold Innerbody, Front Position	.1546E-2	0
	.1695E-2	10
	.1523E-2	20
	.1149E-2	30
	.7358E-2	40
	.3496E-2	50
	.2132E-3	60
	.1333E-3	70
Gold Cylinder With Gold Innerbody, Center Position	.1546E-2	0
	.1684E-2	10
	.1347E-2	20
	.9405E-3	30
	.7385E-3	40
Black Cylinder	.3818E-2	0
	.2132E-2	10
	.6955E-3	20
	.1036E-4	30
	.2903E-5	40

TABLE 9 (CONT'D)
RESULTS OF EMPIRICAL COMPUTER PROGRAMS

Configuration	Radiant Intensity (watts/ster.)	Angle in Degrees
Black Cylinder	.1546E-2	0
With	.3638E-3	10
Black Innerbody, Front Position	.6281E-5	20
Large Gold Cone	.5675E-2	0
	.5454E-2	10
	.4305E-2	20
	.1948E-2	30
	.5573E-4	40
	.0000E-9	50
Large Black Cone	.1750E-2	0
	.1692E-2	10
	.4301E-3	20
Small Gold Cone	.1804E-2	0
	.1773E-2	10
	.1718E-2	20
	.1675E-2	30
	.1588E-2	40
	.1459E-2	50
Small Black Cone	.1804E-2	0
	.1635E-2	10
	.4474E-3	20
	.8022E-5	30
Gold Double Cone	.2965E-2	0
	.2737E-2	10
	.2201E-2	20
	.1399E-2	30

TABLE 9 (CONT'D)
RESULTS OF EMPIRICAL COMPUTER PROGRAMS

Configuration	Radiant Intensity (watts/ster.)	Angle in Degrees
Black Double Cone	.2102E-2	0
	.1563E-2	10
	.7717E-3	20
	.7198E-4	30

to the base -10 exponent. The results have also been plotted in graphical form in Figures 19 through 39 along with the measured radiant intensities. The normal radiance of the source plate, i. e., the quantity N_0 in Eqs. (33) and (37), was calculated to be 0.4709 watts/m² - steradian.

COMPARISON OF EXPERIMENTAL MEASUREMENTS AND EMPIRICAL PREDICTIONS

The degree of success achieved in establishing an empirical formulation to predict laboratory measurements has been encouraging. An examination of Figures 19 through 39 will give an idea of the measure of achievement.

Figure 19 presents perhaps the best agreement obtained. The small differences are easily within the realm of experimental error. Figure 20 exhibits primarily a difference in intensity rather than shape. The fact that an averaged radiance for the unshielded source plate (an experimentally measured quantity) was used for the normal radiance in the computer program may account for small deviations in the radiant intensities of the measured and the predicted curves. Figures 21 and 22 exhibit a somewhat more serious problem, in that there is a noticeable difference in the shapes of the predicted curves compared with the measured curves. An examination of this problem suggested the need for a supplementary computer program which will be discussed presently. Figure 27 shows good agreement except for the magnitudes of the intensity at 30° and 40° . Figure 31 played a prominent part in the formulation of the supplementary program, without which the nearly constant intensity seemed untenable. Finally, Figure 39 exhibits remarkable agreement.

An examination of Figure 31 from the viewpoint of the present computer program revealed that any ray passing through the aperture would strike the source plate with only a few reflections, at the most. The present Monte Carlo techniques required about two hundred rays per angle for a reliable statistical treatment. This means that the intensity predicted by the present program would indeed remain nearly constant, independent of angle, for models having reflectivities near unity. However, physically, a ray at a large angle sees a much smaller effective aperture area, with a correspondingly smaller probability of intersecting the aperture. Furthermore, examination of Eq. (29) (page 78) shows no explicit angular dependence in calculating a quantity expected to vary with angle. Even the area of the aperture, entering through the Monte Carlo distribution function, is constant. The projected area of a plane circle decreases as the cosine of the angle of projection. If

a factor of $\cos \phi$ be inserted in Eq. (29), the resulting curve gives excellent agreement with the measured curve. But, the same factor in the program for the cylinder destroys agreement. The factor needed, apparently, must be dictated by the geometry of the model configuration. The most feasible solution seemed to lie in the writing of a computer program which reversed the philosophy of the present programs. Namely, rays given random directions at the source plate should be traced outwardly, with allowances for their radiating into three dimensions. By circularly projecting the rays onto the horizontal diametral plane, the natural distribution with respect to the axis, as determined by the geometry of the model, could be observed. This distribution, in turn, would dictate the angularly dependent factors to be used in Eq. (29). Unfortunately, this apparent deficiency in the empirical formulation was not discovered until a few weeks before the termination of the project. An attempt was made to write such a program for the cylinder, but insufficient time did not permit its utilization. However, the agreement obtained by the present programs has clearly established the feasibility of such an empirical approach to the problem of predicting the radiative characteristics of shielded sources.

DISTRIBUTION

U. S. Army Test and Evaluation Command	3
U. S. Army Command and General Staff College	1
Army War College	1
U. S. Army Armor Board	1
U. S. Army Aviation Test Board	1
Aviation Test Office, Edwards AFB	1
The Research Analysis Corporation	1
Army Research Office, Durham	2
Office of Chief of R&D, D/A	1
U. S. Army Liaison Officer, Naval Air Test Center	1
Army Research Office, D/A	1
U. S. Army Aviation School	1
Deputy Chief of Staff for Military Operations, D/A	1
U. S. Army Engineer Research and Development Laboratories	1
U. S. Army Combat Developments Command	
Transportation Agency	1
U. S. Army Aviation and Surface Materiel Command	1
U. S. Army Transportation Research Command	21
U. S. Army Tri-Service Project Officer (MCLATS)	1
U. S. Army Transportation School	3
U. S. Army Airborne, Electronics and Special Warfare Board	1
U. S. Army Research and Development Group (Europe)	1
U. S. Army Aviation School	1
Air University Library, Maxwell AFB	1
Air Force Systems Command, Wright-Patterson AFB	2
Bureau of Naval Weapons	1
NASA-LRC, Langley Station	2
George C. Marshall Space Flight Center, NASA	1
Ames Research Center, NASA	1
Lewis Research Center, NASA	1
NASA Representative, Scientific and Technical Information Facility	1
Defense Documentation Center	10
U. S. Patent Office	1
U. S. Army Mobility Command	2
U. S. Army Materiel Command	2
U. S. Army Limited War Laboratory	1

Hayes International Corp., Birmingham, Ala., A STUDY OF THE RADIATIVE CHARACTERISTICS OF SHIELDED INFRARED SOURCES - C. M. Askey, N. D. Gilliam, J. L. Reid, W. S. Harbin, Engineering Report No. 649, October 1963, (Contract DA 44-177-TC-805), USATRECOM Task ID121401A14802 (Formerly Task 9R38-01-022-02), TRECOM Technical Report 63-45, 100 pp.

Unclassified Report
(over)

1. Infrared Physics
2. Contract DA 44-177-TC-805

Hayes International Corp., Birmingham, Ala., A STUDY OF THE RADIATIVE CHARACTERISTICS OF SHIELDED INFRARED SOURCES - C. M. Askey, N. D. Gilliam, J. L. Reid, W. S. Harbin, Engineering Report No. 649, October 1963, (Contract DA 44-177-TC-805), USATRECOM Task ID121401A14802 (Formerly Task 9R38-01-022-02), TRECOM Technical Report 63-45, 100 pp.

Unclassified Report
(over)

Hayes International Corp., Birmingham, Ala., A STUDY OF THE RADIATIVE CHARACTERISTICS OF SHIELDED INFRARED SOURCES - C. M. Askey, N. D. Gilliam, J. L. Reid, W. S. Harbin, Engineering Report No. 649, October 1963, (Contract DA 44-177-TC-805), USATRECOM Task ID121401A14802 (Formerly Task 9R38-01-022-02), TRECOM Technical Report 63-45, 100 pp.

Unclassified Report
(over)

1. Infrared Physics
2. Contract DA 44-177-TC-805

Hayes International Corp., Birmingham, Ala., A STUDY OF THE RADIATIVE CHARACTERISTICS OF SHIELDED INFRARED SOURCES - C. M. Askey, N. D. Gilliam, J. L. Reid, W. S. Harbin, Engineering Report No. 649, October 1963, (Contract DA 44-177-TC-805), USATRECOM Task ID121401A14802 (Formerly Task 9R38-01-022-02), TRECOM Technical Report 63-45, 100 pp.

Unclassified Report
(over)

1. Infrared Physics
2. Contract DA 44-177-TC-805

This interim report gives an account of an experimental measurements program and an empirical formulation for determining the radiative characteristics of shielded infrared sources. Included is a detailed description of the apparatus and instrumentation used in the experimental program and the computer programs for predicting radiant intensity as a function of aspect angle.

The results of the empirical formulation when compared with the experimental measurements clearly indicate the feasibility of this method.

This interim report gives an account of an experimental measurements program and an empirical formulation for determining the radiative characteristics of shielded infrared sources. Included is a detailed description of the apparatus and instrumentation used in the experimental program and the computer programs for predicting radiant intensity as a function of aspect angle.

The results of the empirical formulation when compared with the experimental measurements clearly indicate the feasibility of this method.

This interim report gives an account of an experimental measurements program and an empirical formulation for determining the radiative characteristics of shielded infrared sources. Included is a detailed description of the apparatus and instrumentation used in the experimental program and the computer programs for predicting radiant intensity as a function of aspect angle.

The results of the empirical formulation when compared with the experimental measurements clearly indicate the feasibility of this method.

This interim report gives an account of an experimental measurements program and an empirical formulation for determining the radiative characteristics of shielded infrared sources. Included is a detailed description of the apparatus and instrumentation used in the experimental program and the computer programs for predicting radiant intensity as a function of aspect angle.

The results of the empirical formulation when compared with the experimental measurements clearly indicate the feasibility of this method.

Hayes International Corp., Birmingham, Ala., A STUDY OF THE RADIATIVE CHARACTERISTICS OF SHIELDED INFRARED SOURCES - C. M. Askey, N. D. Gilliam, J. L. Reid, W. S. Harbin, Engineering Report No. 649, October 1963, (Contract DA 44-177-TC-805), USATRECOM Task ID121401A14802 (Formerly Task 9R38-01-022-02), TRECOM Technical Report 63-45, 100 pp.

Unclassified Report
(over)

1. Infrared Physics
2. Contract DA 44-177-TC-805

Hayes International Corp., Birmingham, Ala., A STUDY OF THE RADIATIVE CHARACTERISTICS OF SHIELDED INFRARED SOURCES - C. M. Askey, N. D. Gilliam, J. L. Reid, W. S. Harbin, Engineering Report No. 649, October 1963, (Contract DA 44-177-TC-805), USATRECOM Task ID121401A14802 (Formerly Task 9R38-01-022-02), TRECOM Technical Report 63-45, 100 pp.

Unclassified Report
(over)

1. Infrared Physics
2. Contract DA 44-177-TC-805

Hayes International Corp., Birmingham, Ala., A STUDY OF THE RADIATIVE CHARACTERISTICS OF SHIELDED INFRARED SOURCES - C. M. Askey, N. D. Gilliam, J. L. Reid, W. S. Harbin, Engineering Report No. 649, October 1963, (Contract DA 44-177-TC-805), USATRECOM Task ID121401A14802 (Formerly Task 9R38-01-022-02), TRECOM Technical Report 63-45, 100 pp.

Unclassified Report
(over)

Hayes International Corp., Birmingham, Ala., A STUDY OF THE RADIATIVE CHARACTERISTICS OF SHIELDED INFRARED SOURCES - C. M. Askey, N. D. Gilliam, J. L. Reid, W. S. Harbin, Engineering Report No. 649, October 1963, (Contract DA 44-177-TC-805), USATRECOM Task ID121401A14802 (Formerly Task 9R38-01-022-02), TRECOM Technical Report 63-45, 100 pp.

Unclassified Report
(over)

1. Infrared Physics
2. Contract DA 44-177-TC-805

This interim report gives an account of an experimental measurements program and an empirical formulation for determining the radiative characteristics of shielded infrared sources. Included is a detailed description of the apparatus and instrumentation used in the experimental program and the computer programs for predicting radiant intensity as a function of aspect angle.

The results of the empirical formulation when compared with the experimental measurements clearly indicate the feasibility of this method.

This interim report gives an account of an experimental measurements program and an empirical formulation for determining the radiative characteristics of shielded infrared sources. Included is a detailed description of the apparatus and instrumentation used in the experimental program and the computer programs for predicting radiant intensity as a function of aspect angle.

The results of the empirical formulation when compared with the experimental measurements clearly indicate the feasibility of this method.

This interim report gives an account of an experimental measurements program and an empirical formulation for determining the radiative characteristics of shielded infrared sources. Included is a detailed description of the apparatus and instrumentation used in the experimental program and the computer programs for predicting radiant intensity as a function of aspect angle.

The results of the empirical formulation when compared with the experimental measurements clearly indicate the feasibility of this method.

This interim report gives an account of an experimental measurements program and an empirical formulation for determining the radiative characteristics of shielded infrared sources. Included is a detailed description of the apparatus and instrumentation used in the experimental program and the computer programs for predicting radiant intensity as a function of aspect angle.

The results of the empirical formulation when compared with the experimental measurements clearly indicate the feasibility of this method.

UNCLASSIFIED

UNCLASSIFIED